VARIATIONAL STUDIES OF EXOTIC BOSE LIQUID, SPIN LIQUID, AND MAGNETIC PHASES

Thesis by

Tiamhock Tay

In Partial Fulfillment of the Requirements
for the Degree of
Doctor of Philosophy

California Institute of Technology
Pasadena, California

2011
(Defended 27 May 2011)

To Bubble and Buttercup

Acknowledgements

This dissertation would not be possible without the guidance of my thesis advisor, Lesik Motrunich, who has been very encouraging, patient, always willing to teach, and always finds time to discuss any issue I have whenever I knock on his office door. Despite being instrumental in directing much of the progress in our work, Lesik has always refused to take the credit and would always encourage me by highlighting my contributions. I also would like to thank Gil Refael for sharing his insights and views, which have helped to shape some of my perspective of physics. To my Caltech friends – Heywood Tam, Hsin-hua Lai, Wei Liang, Jing liu, Liyan, Zhaorui, Xiaowei, and many others whom I had the privilege to interact with – I wish to thank them for having enriched my experience here.

I am blessed to have the companionship of my wife, Kweelee, who has given me her unfailing love and encouragement throughout these years, and has always accepted me with all my strengths and weaknesses. Without her, this thesis would not have been completed.

Abstract

The strong interest in strongly correlated systems in condensed matter physics has continued unabated for the past few decades. In recent years, the number of novel, exotic quantum phases found in theoretical studies has seen a phenomenal rise. Among those interesting quantum states are bose liquids and spin liquids, where strong quantum fluctuations have prevented the systems from developing a long range order. Our work in this thesis seeks to further the understanding of frustrated systems. In the study of a hard-core boson model with ring-only exchange interactions on a square lattice, we obtain concrete numerical realization of the unconventional Exciton Bose Liquid (EBL) phase, which possesses interesting properties such as a "Bose surface" which resembles the Fermi surface in a metal, as well as unusual thermodynamic properties such as a $T \log T$ dependence for specific heat. An equally important result from this work is the demonstration that the widely used Gutzwiller projection on slave-particle wave functions may generally fail to capture the correct long wavelength physics in the respective systems. For the Heisenberg antiferromagnet on the kagome lattice, which is a promising candidate for realizing a spin-disordered ground state, our variational study shows that the projected Schwinger boson wave function is energetically better than the Dirac spin liquid wave function when a small antiferromagnetic second-neighbor spin coupling is added to the nearest-neighbor model. We also study the anisotropic triangular Heisenberg antiferromagnetic in magnetic field, and find simple, yet accurate wave functions for various regions of the surprisingly rich phase diagram, thus providing insights into the energetics of the competing phases in this interesting model. Finally, our work also highlights permanent-type wave functions as potentially useful constructions in variational studies of systems with short-ranged correlations, e.g., a Mott insulator and a gapped spin liquid.

Contents

Chapter 1

Introduction

1.1 Overview of thesis

In this thesis, we study a pure ring-exchange model on the square lattice with the objective of realizing the exciton Bose liquid (EBL) phase first proposed by Paramekanti, Balents and Fisher. The EBL is an unconventional quantum phase in which bosons do not condense and are not localized by interactions. With an unusual "Bose surface" in the energy spectrum analogous to the Fermi surface in a metal, the lines of gapless excitations in the Brillouin zone result in low temperature properties different from conventional bosonic phases. In earlier numerical studies, single-boson hopping was found to result in an instability to superfluid order, and pure ring exchanges on 1×1 plaquettes instead realize a (π, π) charge density wave (CDW). To suppress the superfluid and the CDW orders, we exclude single-boson hopping and introduce competing ring terms on 1×2 and 2×1 plaquettes. Our main interest here is whether this unconventional phase can be realized in a concrete Hamiltonian. We set up a Green's Function Monte Carlo simulation which allows us to obtain a numerically exact phase diagram. We obtain a strong evidence that the EBL is realized for boson density less than 1/2. We find that the system is unstable to phase separation at low densities. This is not surprising since the bosons can gain energy from the ring exchanges only when they are sufficiently close to one another. At half-filling, we obtain the $\pi \times \pi$ CDW order in the parameter regime close to the original 1×1 ring model, and the EBL phase when the 1×2 and 2×1 ring exchanges dominate. In the intermediate regime for the parameter, we obtain a Valence Bond Solid (VBS).

A spin off from our attempt to find a concrete model for realizing the EBL phase is our observation that the EBL phase is a fractionalized phase in which each boson can be viewed as a composite of two partons, such that one species move horizontally only while the other move vertically. By coupling the partons to the gauge field with opposite gauge charges, we show that the low energy effective theory of the parton-gauge system realizes the EBL theory. In this picture, the ring interaction between two bosons can be interpreted as an exchange of partons. The critical question that we attempt to address here is whether the widely used Gutzwiller projection for obtaining a variational wave function from slave particle wave functions is able to capture the spatial gauge fluctuations in a gauge theory. We compare an exact EBL wave function and a Gutzwiller wave function for hard-core bosons and find qualitative differences in the low energy properties such as the density structure factor and decay in the correlation at large distances, thus verifying our intuition that Gutzwiller wave functions might not accurately capture the true physics.

We also investigate magnetically ordered states and quantum liquids from a variational perspective. Due to the lack of unbiased numerically exact tools in the study of frustrated systems, the well known sign problem presents a difficulty for quantum Monte Carlo. For this reason, we use the variational Monte Carlo (VMC) to identify candidate ground states among competing trial states in spin-1/2 Heisenberg antiferromagnets on the triangular and kagome lattices, where a combination of geometrical frustration and small spin on the low-dimensional lattice leads to enhanced quantum fluctuations and interesting physics.

On the triangular lattice, the high coordination number (i.e., six) helps to stabilize various magnetic phases. We investigate the magnetic orderings on an anisotropic triangular antiferromagnet in magnetic field by first mapping to an equivalent hard-core boson model with nearest-neighbor repulsion. In the bosonic language, the competition between the bosons trying to gain energy via hopping and the need to minimize the repulsion energy gives rise to a number of interesting phases. By constructing physically motivated wave functions guided by some intuition acquired from the bosonic picture, we calculate variational energies for the isotropic 36-site cluster in magnetic field and find a good agreement with exact diagonalization (ED) results. We extend this study to the anisotropic regime and obtain a very rich phase diagram.

For the kagome antiferromagnet, the lower coordination number (i.e., four) of the lattice instead stabilizes a spin liquid phase. We study a specific spin liquid known as the Resonance Valence Bond (RVB) state, first proposed by P. W. Anderson in connection with the pseudogap regime of high temperature superconductivity. By using the Schwinger boson representation for the spin operators, we decouple the resulting quartic Hamiltonian and obtain a solvable mean-field Hamiltonian. On projecting the mean-field ground states onto the physical spin-1/2 sector, we obtain

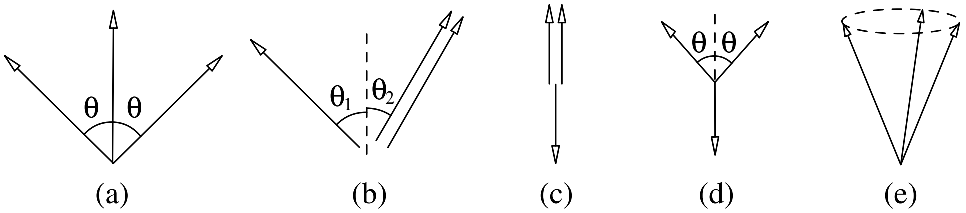

Figure 1.1: Spin orderings of the classical ground states, which we denote using (a) Ψ, (b) V, (c) *uud*, (d) Y, and (e) *spiral*. For each of these orderings, the three arrows represent the spin orientations on the three sublattices of the triangular lattice.

RVB states which consist of linear combinations of dimer covers. We find that the amplitude of the singlet bonds can be tuned from a quasi long-range decay to an exponential decay by varying the chemical potential in the mean-field Hamiltonian. The closing of the spinon energy gap at a critical value of the chemical potential results in condensation of spinons and consequently, producing a wave function with magnetic order. Thus, the range of the singlet bonds helps to provide an indication whether the variational ground state is spin-disordered or close to realizing a magnetic order. Using these RVB states constructed from the slave-particle approach, we compare the energies of the projected Schwinger boson wave functions against other competing variational states for the first- and second-nearest-neighbor J_1-J_2 Heisenberg model. We find that the projected Schwinger boson wave function is a viable candidate for $J_2 > 0.08J_1$.

The remainder of this chapter provides a more detailed introduction to each of the studies described above, while the following chapter contains simple theoretical treatments of the models which bridge the gap to the material in later chapters. Chapters 3 to 6 are a collection of published papers[1, 2, 3, 4, 5] co-authored with my thesis advisor, Olexei I. Motrunich. It is a pleasure to acknowledge his important, extensive contributions which have unveiled the interesting physics in the study of these strongly correlated systems.

1.2 Triangular antiferromagnet in magnetic field

The nearest-neighbor spin-1/2 Heisenberg antiferromagnet on the spatially anisotropic triangular lattice in magnetic field is a simple quantum model that surprisingly captures a rather rich physics. When analyzed classically, the spatially isotropic model contains degenerate ground states for all fields between zero and the saturation field. These states are magnetically ordered with a three-sublattice structure in their spin orientations as depicted in Fig. 1.1. The *spiral* and Y orderings have equal energies at low fields, while V, Ψ, and *spiral* have equal energies at high fields. At 1/3 of the saturation field, the Y and V orderings reduce to the *uud*, which also has the same energy as the *spiral* and Ψ orderings.

The degeneracies in the classical ground states are lifted by thermal fluctuations at finite temperatures. In a classical Monte Carlo study by Kawamura *et al.*[6], the coplanar Y and V orderings are found to be selected at low and high magnetic fields respectively, while the collinear *uud* ordering is increasingly stabilized with temperature at intermediate fields. For the isotropic quantum model at zero temperature, a semi-classical analysis by Chubukov *et al.* shows that quantum fluctuations also select the same coplanar and collinear orderings[7]. The *uud* has been predicted to give rise to a 1/3-magnetization plateau (see Fig. 3.5 on page 41) but was first observed much later in a high field magnetization study by Ono *et al.* on the nearly isotropic Cs_2CuBr_4[8]. A more recent experiment by Fortune *et al.* further reveals a cascade of quantum phase transitions in magnetocaloric and magnetic-torque measurements made on the same chemical compound[9].

A similar attempt to identify the newly discovered phases using the semi-classical analysis would immediately run into difficulty. In fact, an incommensurate generalization of the *spiral* phase becomes the unique classical ground state of the anisotropic model at all fields, hence spin-wave expansions about other classical orderings such as the *uud* are not allowed for finite anisotropy. This issue was overcome by Alicea *et al.*[10] by extending the large-S expansion to an interacting spin-wave theory controlled by large spin as well as small spatial anisotropy. Their theoretical results show that strong quantum fluctuations again select the *uud* state at intermediate fields as well as the coplanar orderings in its vicinity. The *uud* plateau extends considerably into the anisotropic region, and they also obtain incommensurate coplanar and distorted spiral phases for larger anisotropy.

The extension of the triangular Heisenberg antiferromagnet to the anisotropic regime also creates additional fronts for investigations. In addition to the regime near the plateau, the model has been analyzed from the high field limit and the weak inter-chain coupling limit. Using a mapping from spin-1/2 operators into hard-core boson operators, the high field regime is equivalent to a dilute gas of hard-core bosons hopping on the lattice with nearest-neighbor repulsions. An analysis of the isotropic model by Nikuni *et al.*[11] showed that the coplanar V and Ψ states have lower energies than the *spiral*, but their calculations were unable to resolve the energy difference between the two. Veillette *et al.* studied the dilute gas model for an anisotropy relevant to Cs_2CuCl_4 and found that the incommensurate *spiral* dominates near the saturation field, but undergoes phase transition at a slightly lower field to a commensurate non-coplanar ordering[12].

From the decoupled-chain limit, Starykh *et al.* argues that the interchain coupling is a relevant perturbation and can induce various boson CDW phases or a spiral phase[13]. The former happens for small and intermediate fields, while the latter is expected near the saturation field. In zero magnetic field, their study predicted a collinear antiferromagnetic order while variational studies suggest that the non-coplanar *spiral* phase is stable for small lattice anisotropy[14], and the intermediate anisotropic region may contain one or two spin liquid phases[15, 16]. This is supported by an ED/DMRG study which found signatures of spin liquid for $J'/J < 0.78$ from numerical measurements of spin structure factor, excitation energy gap, and spin correlation[17].

In Chapter 3, we investigate the anisotropic Heisenberg model in magnetic field by studying the equivalent hard-core boson model using the variational approach. Here, we provide a summary of our results in reference to a schematic phase diagram shown in Fig. 3.10 on page 55. Starting from the 1/3-magnetization for the isotropic regime, we construct an accurate Mott insulator wave function which features a short range correlation between every pair of sites. This wave function naturally generalizes to the nearby commensurate coplanar Y and V states which are realized as supersolid states in the hard-core boson picture. Interestingly, the Y wave function has a short range correlation when at least one site resides on the "down" sublattice (see Fig. 1.1d). This contrasts with the long range correlation when both sites belong to the remaining sublattices. For the V phase, we construct a supersolid wave function having long range correlations between all sites on the lattice. Our accurate wave functions allow us to obtain upper and lower critical fields of the plateau which agree quantitatively with other studies. For magnetic fields close to zero, we find that Huse and Elser's *spiral* wave function[14] performs better than the Y state.

Encouraged by the accuracy of our variational study for the isotropic regime, we generalize our commensurate wave functions to study the anisotropic lattice. We find that the *uud* plateau extends deep into the anisotropy regime. At high fields, we obtain an incommensurate coplanar ordering for low anisotropy and the incommensurate *spiral* for higher anisotropy, with the boundary between the two shifting in favor of the *spiral* as the field decreases away from saturation. In the highly anisotropic regime at low to intermediate fields, we find that our wave function constructed from a "2-parton" slave-particle approach gives very good energies but we interpret this as a consequence of finite-size effects, thus suggesting that other numerical techniques such as the Density Matrix Renormalization Group (DMRG) would be necessary for unveiling the physics in the quasi one-dimensional regime.

1.3 Exciton Bose Liquid

The search for exotic quantum phases has gained a very wide audience in recent years. A number of years ago, Paramekanti *et al.*[18] proposed an interesting critical bosonic phase which shares many characteristics normally associated with electrons in a metal. Starting with a bosonic ring exchange model on the square lattice, where two bosons hop simultaneously on opposite corners of an elementary square plaquette to the other two corners, they derived a low energy effective Lagrangian in terms of the boson phase variable and its dual vortex phase variable. The effective theory demonstrates a remarkable similarity to the bosonized action for a one-dimensional Luttinger liquid, and can be traced back to the "dimensional reduction" of the system which results from the conservation of boson numbers along each row and each column of the square lattice. The energy spectrum of the system features lines of gapless excitations (see Fig. 1.2) that are responsible for various properties of the system such as a power-law decay in the correlations and a specific heat varying as $T \log(1/T)$. A striking parallel to electrons in a metal is pointed out by Sachdev[19], where the Fermi surface separates occupied electron states from the vacant states. Here, the zero energy lines in Brillouin zone can be analogously termed the "Bose surface" since low energy excitations of the system occur near this surface, and Bose-condensation does not occur in the system.

Known as the exciton Bose Liquid (EBL), Paramekanti *et al.* suggested that this critical quantum state may be appropriate for describing the charge sector in the underdoped cuprates where ring exchange processes might be stronger. In Sec. 2.2, we show that the "dimensional reduction" of the problem can be understood via a slave-particle approach. Starting from a parton-gauge system on the square lattice, where one species of partons move horizontally only and couple to the gauge field with a positive gauge charge while the others move vertically and carry negative gauge charge, the fluctuations of the gauge fields bind together one parton of each species to give the original boson. The resulting low energy theory of the parton-gauge system reduces to the EBL action when the gauge fields are integrated out. This formulation provides an alternative perspective of the EBL as a fractionalized phase.

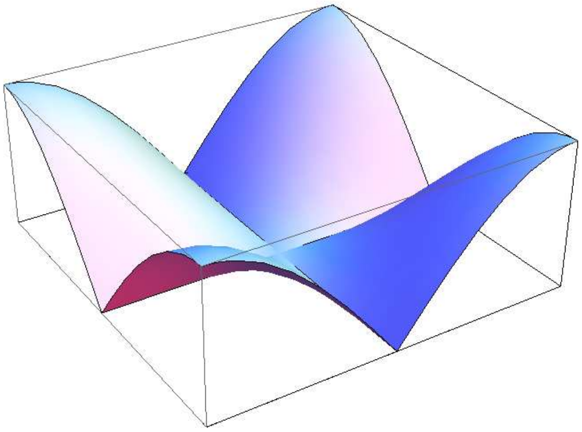

Figure 1.2: The EBL phase is characterized by a "Bose surface", that is, the lines of gapless excitations in the Brillouin zone (i.e., $k_x = 0$ or $k_y = 0$) which are responsible for the unusual low temperature properties.

The striking proposal of Paramekanti *et al.* stimulated a number of works which seek to establish the stability of the EBL phase in hard-core boson models with ring exchange interactions on the square lattice[20, 21, 22, 23]. However, these studies found that the EBL is not realized in these models. Instead, such ring interactions favor a (π, π) charge density wave (CDW) in the half-filled case, while away from half-filling they induce strong tendencies to phase separation. With a goal of realizing the novel EBL phase, we attempt to suppress the CDW order by adding competing ring exchanges to the system. We consider in Chapter 4 a specific hard-core boson model with competing ring-only exchanges on a square lattice, where a K_1 term acts on 1×1 plaquettes and a K_2 term acts on 1×2 and 2×1 plaquettes. We construct Jastrow-type variational wave functions for the EBL and study their formal properties using Variational Monte Carlo. The optimized trial wave functions are then used as starting points for a projective Quantum Monte Carlo study. Using Green's Function Monte Carlo, we obtain an unbiased phase diagram (cf. Fig. 4.14 on page 83) which at half-filling reveals CDW for small K_2, valence bond solid for intermediate K_2, and possibly for large K_2 the EBL phase. Away from half-filling, we argue that the EBL phase is present for intermediate K_2 and remains stable for a range of densities below 1/2 before phase separation occurs at lower densities.

In Chapter 5, we continue our study of the EBL phase in the parton-gauge picture but focusing on the question of whether the absence of dynamical gauge fluctuations may lead to a qualitatively different phase. In place of the dynamical gauge fluctuations, we consider a simplified procedure using Gutzwiller-projected trial states. We show that the Gutzwiller projection indeed leads to a state with subtle differences in the long-wavelength properties, thus suggesting that Gutzwiller wave functions may generally fail to capture long-wavelength physics.

1.4 Kagome antiferromagnet

In recent years, interest in the spin-1/2 Heisenberg antiferromagnetic model on the kagome lattice has been re-ignited by exact diagonalization (ED) and Density Matrix Renormalization Group (DMRG) studies which provide stronger evidence that the ground state of the system realizes a spin liquid[24, 25, 26]. At the classical level, geometrical frustration is known to result in a macroscopically large number of degenerate ground states. This is easily seen by noting that any classical spin configuration having its spins oriented at 120° apart on every elementary triangular plaquette is a ground state of the system. Thus, listing down these states amounts to assigning one out of three possible spin orientations (denoted A, B, and C) to every site such that no two nearest neighbors point in the same direction. As an illustration, Fig. 1.3 shows three out of 504 possibilities for a 36-site cluster with periodic boundary condition. In addition to this huge degeneracy among coplanar states, the plane formed by any closed loop containing only two spin directions (e.g., A–B–A–B–A–B–A around an hexagon) can be rotated about the third direction (i.e., C) without incurring an energy penalty. This huge number of continuously degenerate ground states therefore cast doubts on the validity of a spin-wave expansion of the quantum model about a specific classical ordering, and instead raises the prospect of the system realizing a spin-disordered ground state.

Numerical evidence from ED and DMRG studies indicates that the Heisenberg antiferromagnet on the kagome lattice does not have any magnetic or valence bond ordering[27, 28, 25, 29]. These studies found short ranged spin-spin correlations and a finite spin gap estimated at $J/20$, where J is the nearest-neighbor coupling constant[28, 25, 26]. Interestingly, a large number of singlet excitations are observed in the spin gap[25]. On the experimental side, the lack of a magnetic order persists down to 50 mK in the material Herbertsmithite which contains weakly coupled layers of spin-1/2 kagome antiferromagnets[30, 31, 32, 33]. Thus, there is a convergence of views over the years that the isotropic spin-1/2 Heisenberg antiferromagnet with only nearest-neighbor exchange indeed realizes a spin liquid.

Many other computational approaches have been used to study the kagome antiferromagnet. Among these include series expansions[34, 35, 36] which propose a valence

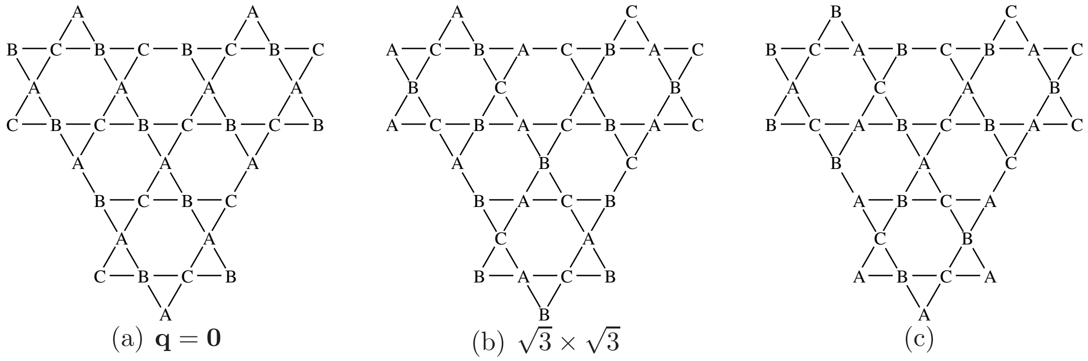
(a) $\mathbf{q} = \mathbf{0}$ (b) $\sqrt{3} \times \sqrt{3}$ (c)

Figure 1.3: Illustration of three possible spin orderings out of a total of 504 for a periodic 36-site cluster, where A, B and C denotes three coplanar vectors with 120° between them. These states have identical energy for the classical model, but the degeneracy may be lifted by thermal or quantum fluctuations.

bond crystal with a 36-site unit cell as the ground state, contractor renormalization (CORE)[37, 38], and multi-scale entanglement renormalization ansatz (MERA)[39].

Slave-particle approaches have also been used to explore the possible nature of the spin liquid ground state. An early study by Sachdev using Sp(N) Schwinger bosons in the large-N limit found the $\sqrt{3} \times \sqrt{3}$ magnetically ordered ground state[40] for spin $S > 0.26$, depicted in Fig. 1.3(b). Analysis of the gauge field fluctuations showed that the spinons remain deconfined for $S < 0.26$, while they condense for larger spin and result in the magnetic ordering. Attempts to extend the spin liquid regime to the physical spin $S = 1/2$ would fail to address the continuum of singlet excitations found in the spin gap by ED studies[25], since the Schwinger boson spinon spectrum is gapped. A different approach by Hastings uses slave fermions to construct a long range Resonating Valence Bond (RVB) state with a Dirac structure in the spinon spectrum[41]. Hastings' state, also known as the Dirac spin liquid, is appealing since it contains low energy gauge excitations. A subsequent Gutzwiller projection on the mean-field Dirac spin liquid wave function by Ran *et al.* obtained a variational energy which lies close to the ED ground state energy[42, 27].

Our work in this thesis is motivated by the question of whether Gutzwiller projection on the Schwinger boson spin liquid wave function may result in a more competitive variational energy. However, unlike the fermionic case which requires computation of determinants, the projection on a bosonic mean-field wave function in general leads to permanents whose computational cost scales poorly with the system size. To our knowledge, this has not been carried out in the boson number basis, although an alternative workaround using Monte Carlo sampling in the valence bond basis has been implemented for a projected Schwinger boson wave function on the triangular lattice[43]. The latter suffers from a less severe form of sign problem and such calculations are similarly restricted to small system sizes. For our study in Chapter 6, we extend the nearest-neighbor model to the J_1-J_2 Heisenberg model with antiferromagnetic J_2 coupling[44], and investigate the energetics of various wave functions. We find that Sachdev's $Q_1 = Q_2$ Schwinger boson ansatz is a viable candidate for $J_2 \gtrsim 0.08 J_1$ due to a stronger second-neighbor antiferromagnetic spin correlation compared to the Dirac spin liquid. For $J_2 \lesssim -0.04 J_1$, Sachdev's $Q_1 = -Q_2$ ansatz performs well due to its ferromagnetic second-neighbor correlations. Thus, our study shows that the Schwinger boson wave functions may still be relevant despite being eclipsed by the Dirac spin liquid wave function in recent years.

We mention here an extension of our work for future study. Each coplanar spin configuration among the numerous possibilities would lead to a corresponding Schwinger boson mean-field ansatz, which in turn allows us to obtain a projected wave function. One might envisage a multitude of resonances between these states gaining energy from the quantum tunneling, and thereby accounting for the continuum of low energy excitations found in the ED studies for $J_2 = 0$.

Chapter 2

Preliminaries

In this chapter, we discuss some of the models in this thesis using simpler or less accurate theoretical treatments for some special cases, with the purpose of bridging the transitional gap to the material presented in later chapters. In Sec. 2.1, we analyze the isotropic Heisenberg antiferromagnet in magnetic field using a spin-wave approach and discuss how this approach breaks down for the anisotropic lattice. Our variational Monte Carlo treatment in the next chapter allows us to compare competing phases identified by other theoretical approaches. This is achieved by constructing accurate wave functions which help to determine candidate quantum phases. In Sec. 2.2, we provide a parton-gauge perspective to the Exciton Bose Liquid phase whose interesting properties had motivated our search for a realizable concrete model in Chapter 4. In Sec. 2.3, we analyze the nearest-neighbor Heisenberg antiferromagnet on the kagome lattice using a mean-field Schwinger boson slave-particle treatment, while leaving the full analysis for the extension to the second-neighbor Heisenberg model to Chapter 6. Finally, in Sec. 2.4, we discuss the Monte Carlo implementations used in this thesis.

2.1 Spin-wave analysis of the triangular Heisenberg model

The nearest-neighbor antiferromagnetic Heisenberg spin model on an isotropic triangular lattice in magnetic field is given by the following Hamiltonian:

$$H = J \sum_{\langle i,j \rangle} \mathbf{S}_i \cdot \mathbf{S}_j - \vec{h} \cdot \sum_i \mathbf{S}_i, \tag{2.1}$$

where J is the coupling strength between spins on nearest-neighbor sites i and j of the triangular lattice. Due to geometrical frustration on the lattice, it is not possible to saturate the lower bound in the interaction energy for every pair of nearest-neighbors. This results in degenerate ground states in the corresponding classical model at all magnetic fields. To see this, we note that the classical Hamiltonian is minimized when the spin configuration has a three-sublattice structure

$$\begin{aligned} E_{\rm cl}/\text{site} &= JS^2\left(\hat{n}^z_A\cdot\hat{n}^z_B+\hat{n}^z_B\cdot\hat{n}^z_C+\hat{n}^z_C\cdot\hat{n}^z_A\right)-\frac{1}{3}\vec{h}\cdot S(\hat{n}^z_A+\hat{n}^z_B+\hat{n}^z_C), && (2.2)\\ &= \frac{3}{2}JS^2-\frac{1}{18}h^2/J+\frac{1}{2}JS^2\left(\hat{n}^z_A+\hat{n}^z_B+\hat{n}^z_C-\frac{\vec{h}}{3JS}\right)^2, && (2.3)\end{aligned}$$

where $\hat{n}^z_A$, $\hat{n}^z_B$ and $\hat{n}^z_C$ are unit vectors along the directions of the spin orderings on sublattices A, B and C. The ground state spin configurations satisfy

$$\vec{h}=3JS(\hat{n}^z_A+\hat{n}^z_B+\hat{n}^z_C), \tag{2.4}$$

and the only possible orderings are shown in Fig. 1.1, where we denote them by (a) Ψ, (b) V, (c) *uud*, (d) Y, and (e) *spiral*. The saturation field $h = 4.5J$ for the spin-1/2 classical model follows from Eq. (2.4), and this value also holds for the quantum model. For $h < 1.5J$, the *spiral* and Y states are degenerate ground states, while for $1.5 < h/J < 4.5$, the states V, Ψ, and *spiral* are degenerate. At $h = 1.5J$, all of the states shown in Fig. 1.1 have the same energy. In addition to these degeneracies, the energy is invariant under a rotation about the magnetic field.

In the presence of quantum fluctuations, some or all of the degeneracies existing in the classical model may be lifted. In the following, we apply the Holstein-Primakoff transformation:

$$\begin{aligned} S^+ &= \sqrt{2S-a^\dagger a}\;a \approx \sqrt{2S}a, && (2.5)\\ S^- &= a^\dagger\sqrt{2S-a^\dagger a} \approx \sqrt{2S}a^\dagger, && (2.6)\\ S^z &= S-a^\dagger a, && (2.7)\end{aligned}$$

where $a^\dagger$ is a bosonic creation operator, and obtain a spin-wave Hamiltonian

$$\begin{aligned}(H_{\rm SW}-E_{\rm cl})/JS &= \frac{1}{2}\sum_{\mathbf{k}}\nu_{\mathbf{k}}\left(\hat{e}_a\cdot\hat{e}_b\; a_{-\mathbf{k}}b_{\mathbf{k}}+\hat{e}_b\cdot\hat{e}_c\; b_{-\mathbf{k}}c_{\mathbf{k}}+\hat{e}_c\cdot\hat{e}_a\; c_{-\mathbf{k}}a_{\mathbf{k}}\right)\\ &+ \frac{1}{2}\sum_{\mathbf{k}}\nu_{\mathbf{k}}\left(\hat{e}^*_a\cdot\hat{e}_b\; a^\dagger_{\mathbf{k}}b_{\mathbf{k}}+\hat{e}^*_b\cdot\hat{e}_c\; b^\dagger_{\mathbf{k}}c_{\mathbf{k}}+\hat{e}^*_c\cdot\hat{e}_a\; c^\dagger_{\mathbf{k}}a_{\mathbf{k}}\right)\\ &+ \text{H.c.}+3\sum_{\mathbf{k}}(a^\dagger_{\mathbf{k}}a_{\mathbf{k}}+b^\dagger_{\mathbf{k}}b_{\mathbf{k}}+c^\dagger_{\mathbf{k}}c_{\mathbf{k}}), \qquad (2.8)\end{aligned}$$

where $\nu_{\mathbf{k}}=\sum_\mu e^{i\mathbf{k}\cdot\hat{\mu}}$ and $\hat{e}_\alpha=\hat{n}^x_\alpha-i\hat{n}^y_\alpha$. Here, a, b, and c are the annihilation operators on the respective sublattices, $\{\hat{\mu}\}$ are three unit vectors on the lattice which make an angle 120° with one another, and $\hat{n}^j_\alpha$ specifies the orientation of the local j-axis on sublattice α. For non-collinear spin orderings, Eq. (2.4) is used to eliminate terms that are linear in the bosonic operators.

The spin-wave Hamiltonian can be diagonalized using Bogoliubov's transformation. For a general Hamiltonian that is quadratic in the bosonic operators, we may express it as follows:

$$\begin{aligned}H &= \vec{\alpha}^\dagger D\vec{\alpha}, && (2.9)\\ \vec{\alpha} &= (\gamma_1,\cdots,\gamma_n,\gamma^\dagger_{n+1},\cdots,\gamma^\dagger_{2n})^T, && (2.10)\\ [\alpha_i,\alpha_j] &= \eta_{ij}\equiv\text{diag}(1,\cdots,1,-1,\cdots,-1), && (2.11)\end{aligned}$$

where $\{\gamma_i\}$ are $2n$ independent bosonic annihilation operators. If a canonical transformation $\vec{\alpha}=U\vec{\beta}$ results in a diagonal matrix $\Lambda=U^\dagger DU$, then U and Λ must satisfy

$$\begin{aligned}U^\dagger\eta U &= \eta, && (2.12)\\ (\eta D)U &= U(\eta\Lambda). && (2.13)\end{aligned}$$

Since D is positive definite, the eigenvalues of the system are simply given by the absolute values of the corresponding eigenvalues of ηD.

Figure 2.1 compares the energies for the five spin orderings obtained by considering an expansion about each classical ordering. With the classical ground state energy subtracted, the figure illustrates the energy gain from quantum fluctuations. The Y, V, and *uud* curves meet at $h=1.5J$ since the Y and V orderings both reduce to the *uud* ordering at that field. Similarly, the *spiral* meets Y at $h=0$, and meets the V and Ψ curves at saturation. For $h<1.39J$, the Y state has the lowest energy, while

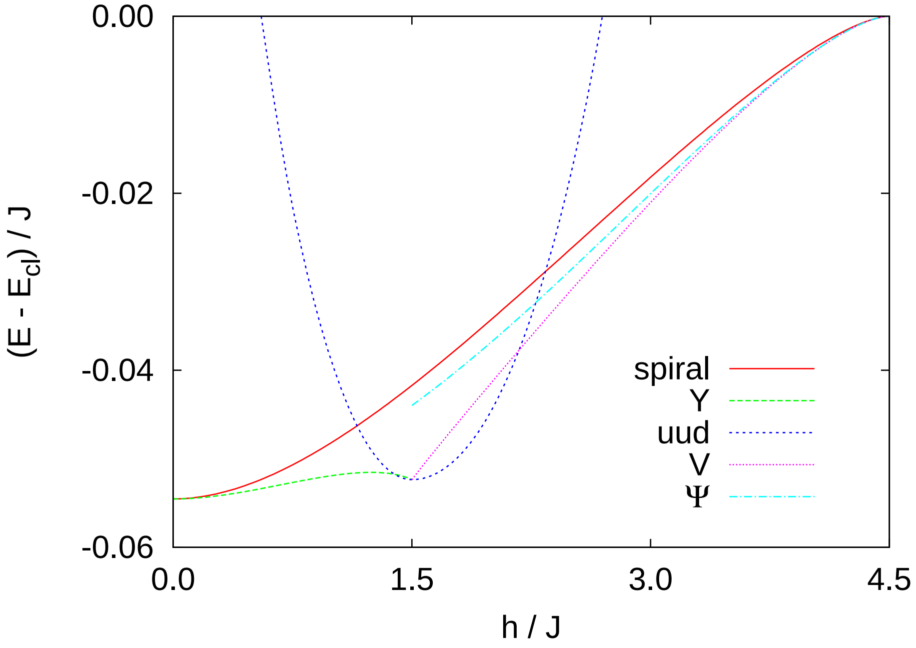

Figure 2.1: Comparison of the spin-wave energies (per bond) for each of the spin orderings listed in Fig. 1.1. The constant magnetization of the *uud* state leads to a 1/3-magnetization plateau for $1.4 < h/J < 2.17$ on an isotropic lattice (see Fig. 3.5).

the high field regime extending up to saturation is dominated by the V state. Interestingly, the *uud* state is stable over the range $1.39 < h/J < 2.17$ despite a smooth interpolation between the classical Y and V configurations through the *uud* ordering as h approaches $1.5J$. This results in a 1/3-magnetization plateau on the triangular lattice (see Fig. 3.5 on page 41) and was observed in $\mathrm{Cs_2CuBr_4}$[8]. In principle, renormalizations of the spin orientations may result from quantum fluctuations[7] and would lead to shifts in the upper and lower critical fields of the *uud* phase, but we have not taken this into consideration here. In contrast to the gapless spectra for the non-collinear spin orderings, we observe a finite gap in the *uud* spectrum which agrees with the absence of Goldstone modes since continuous symmetry has not been broken.

The Hamiltonian terms in Eq. (2.8) are leading order corrections to the classical energy in the Holstein-Primakoff large-S expansion of the quantum model. The truncation of the series at this order may not be accurate enough to resolve the quantum ground states near zero field as well as near saturation. In Chapter 3, we extend the study to the anisotropic lattice, with a coupling constant J for horizontal links on the lattice and J' for links directed along oblique directions. The same classical analysis repeated for the anisotropic lattice would show that the *spiral* is the unique classical ground state at all magnetic fields. The semi-classical spin-wave treatment therefore runs into a difficulty since $\mathrm{Cs_2CuBr_4}$ has been found to realize the 1/3-magnetization plateau despite having an anisotropy estimated to be $J'/J \sim 0.7$. Our approach to the problem is to study an equivalent hard-core boson model using variational Monte Carlo. In the bosonic picture, the spin orderings have interesting interpretations – namely, superfluid, supersolids and a Mott insulator. We study the model on the anisotropic lattice and obtain a very rich phase diagram (see Fig. 3.10). Possible implications to the triangular antiferromagnets $\mathrm{Cs_2CuBr_4}$ and $\mathrm{Cs_2CuCl_4}$ are discussed there.

2.2 Parton-gauge perspective on the Exciton Bose Liquid

In this section, we provide a parton-gauge perspective on the EBL phase. The EBL phase is defined by a fixed point Lagrangian[18]

$$\mathcal{L}_0 = \sum_{\mathbf{r}} \frac{i}{\pi} \partial_\tau \varphi(\mathbf{r}) \Delta_{xy} \vartheta(\mathbf{R}) + \int_{\mathbf{k}} \left[\frac{\mathcal{K}(\mathbf{k})}{2} |(\Delta_{xy}\varphi)_{\mathbf{k}}|^2 + \frac{\mathcal{U}(\mathbf{k})}{2\pi^2} |(\Delta_{xy}\vartheta)_{\mathbf{k}}|^2 \right], \tag{2.14}$$

where φ is the phase of a bosonic field and ϑ is related to the boson density through $n - \bar{n} = \frac{1}{\pi}\Delta_{xy}\vartheta$. The "EBL parameters" $\mathcal{K}(\mathbf{k})$ and $\mathcal{U}(\mathbf{k})$ are functions of $\mathbf{k}$ which respect the square lattice symmetries[18]. Long-wavelength properties such as various power-law exponents depend only on the function $\mathcal{K}(0, k_y)/\mathcal{U}(0, k_y)$. Notice the strong similarity between this Lagrangian and the bosonized action for Luttinger liquid. An effective "dimensional reduction" noted by some authors[18, 45, 46, 47, 48, 49] is suggestive of a decomposition of each boson into two partons with one-dimensional (1D) character, interacting strongly via a gauge field. Below, we show that the gauge fluctuation effects can be treated accurately and lead to the same EBL description. We will also see how the familiar 1D Bosonization techniques[50, 51] allow us to quickly obtain physical observables and important residual interactions in the EBL theory. We emphasize, however, that the EBL phase is qualitatively different from sliding or crossed-sliding Luttinger liquids[52, 53, 54, 55]—for example, it has specific heat $C \sim T \ln(1/T)$, cf. Ref. [18].

To show that one can arrive at the EBL theory by starting from a two-dimensional parton-gauge system, we consider the following Lagrangian:

$$\begin{aligned}\mathcal{L}[\varphi_1, \theta_1, \varphi_2, \theta_2, a_x, a_y] &= \sum_{\mathbf{r}} \frac{\kappa}{2}(\nabla_x a_y - \nabla_y a_x)^2 \\ &+ \sum_{\mathbf{r}} \Big[\frac{J}{2}(\nabla_x \varphi_1 - a_x)^2 + \frac{u}{2}\left(\frac{\nabla_x \theta_1}{\pi}\right)^2 + \frac{i}{\pi}\partial_\tau \varphi_1 \nabla_x \theta_1\Big] \\ &+ \sum_{\mathbf{r}} \Big[\frac{J}{2}(\nabla_y \varphi_2 + a_y)^2 + \frac{u}{2}\left(\frac{\nabla_y \theta_2}{\pi}\right)^2 + \frac{i}{\pi}\partial_\tau \varphi_2 \nabla_y \theta_2\Big].\end{aligned} \tag{2.15}$$

The phase and dual variables $\varphi_1(x, y)$ and $\theta_1(X, y)$ describe a harmonic fluid[50, 51] of partons moving on a horizontally oriented chain located at a vertical coordinate y, while variables $\varphi_2(x, y)$ and $\theta_2(x, Y)$ describe a harmonic fluid of partons moving on a vertically oriented chain at a horizontal coordinate x. Note that $\varphi_1(x, y)$ and $\varphi_2(x, y)$ reside on the sites of the original lattice, while $\theta_1(X, y)$ resides on the horizontal links and $\theta_2(x, Y)$ on the vertical links as illustrated in Fig. 2.2. The coupling parameters J and u represents parton hopping and on-site repulsion, respectively. Note that we assume a stable phase where (a_x, a_y) can be treated as a non-compact gauge field with a large "stiffness" parameter κ. The parton densities are given by

$$n_1(x, y) = \frac{1}{\pi}\nabla_x \theta_1, \tag{2.16}$$

$$n_2(x, y) = \frac{1}{\pi}\nabla_y \theta_2, \tag{2.17}$$

and we now introduce the following constraint to realize the microscopic boson in the EBL phase using a 2-parton composite:

$$\nabla_x \theta_1 = \nabla_y \theta_2 \ . \tag{2.18}$$

At this stage, we can integrate out the fields φ_1 and φ_2 and obtain the Lagrangian density

$$\begin{aligned}\mathfrak{l}[\theta_1, \theta_2, a_x, a_y] &= \frac{u}{2\pi^2}\left[(\nabla_x \theta_1)^2 + (\nabla_y \theta_2)^2\right] + \frac{1}{2\pi^2 J}\left[(\partial_\tau \theta_1)^2 + (\partial_\tau \theta_2)^2\right] \\ &+ \frac{i}{\pi}(a_x\, \partial_\tau \theta_1 - a_y\, \partial_\tau \theta_2) + \frac{\kappa}{2}(\nabla_x a_y - \nabla_y a_x)^2 \ .\end{aligned} \tag{2.19}$$

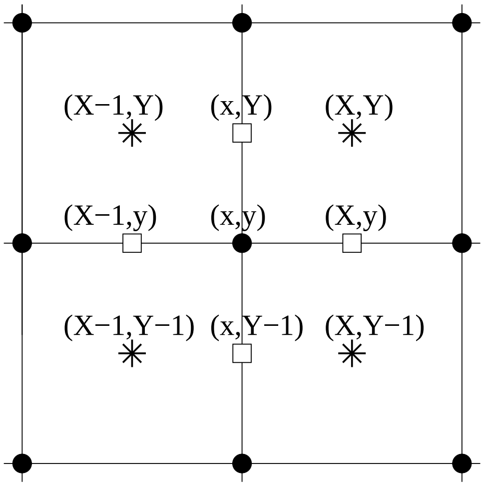

Figure 2.2: The parton phase fields $\varphi_1(x,y), \varphi_2(x,y)$ reside on the sites of the original square lattice (black circles); the 1D dual field $\theta_1(X,y)$ resides on the horizontal links and $\theta_2(x,Y)$ on the vertical links (white boxes). The dual EBL theory field $\vartheta(X,Y)$ resides on the plaquettes of the original lattice, or equivalently on the sites of the dual lattice (stars).

We then solve the constraint Eq. (2.18) via

$$\theta_1(X,y) = \nabla_y \vartheta \equiv \vartheta(X,Y) - \vartheta(X,Y-1) \ , \tag{2.20}$$

$$\theta_2(x,Y) = \nabla_x \vartheta \equiv \vartheta(X,Y) - \vartheta(X-1,Y) \ , \tag{2.21}$$

cf. Fig. 2.2. Integrating out the field $\boldsymbol{a}$, we finally obtain Lagrangian density

$$\mathfrak{l}[\vartheta] = \frac{u}{\pi^2}(\nabla_{xy}^2 \vartheta)^2 + \frac{1}{2\pi^2 J}(\partial_\tau \boldsymbol{\nabla} \vartheta)^2 + \frac{1}{2\pi^2 \kappa}(\partial_\tau \vartheta)^2. \tag{2.22}$$

This is essentially the EBL theory written in the dual variables ϑ [after integrating out the φ variables from Eq. (2.14)], with $\mathcal{U}(\mathbf{k}) = 2u$ and $1/\mathcal{K}(\mathbf{k}) = 4[\sin^2(k_x/2) + \sin^2(k_y/2)]/J + 1/\kappa$. Note that one may be tempted to drop the $(\partial_\tau \boldsymbol{\nabla} \vartheta)^2/J$ term as it contains more derivatives than the $(\partial_\tau \vartheta)^2/\kappa$ term. However, the long-distance EBL properties such as power-law exponents are determined by the full function $\mathcal{K}(0,k_y)$ which does depend on J if we want to be accurate in the simple model Eq. (2.15) that we took. If we include from the start general interactions among the partons and general Maxwell terms for the gauge field, we obtain the general Gaussian EBL theory with $\mathbf{k}$-dependent $\mathcal{K}(\mathbf{k})$ and $\mathcal{U}(\mathbf{k})$.

We can now establish connections between microscopic observables and the EBL theory in the ϑ variables. Thus, in the 1D Bosonization treatment, the particle density and bond energy are given by

$$\begin{aligned}\delta n_1(\mathbf{r}) &= \frac{\nabla_x \theta_1}{\pi} + A\cos\left[2\theta_1 + 2\pi\bar{n}(x-1/2)\right] \ , \qquad (2.23)\\ \delta\mathcal{B}_{\mathbf{r},\mathbf{r}+\hat{\mathbf{x}}} &= A'\cos\left[2\theta_1 + 2\pi\bar{n}x\right] \ . \qquad (2.24)\end{aligned}$$

Here θ_1 already means the long-wavelength component and the precise location where it is evaluated along the chain is unimportant. In terms of the original variables of the EBL theory [replacing θ_1 by Eq. (2.20)], we obtain

$$\begin{aligned}n(\mathbf{r}) &= \bar{n} + \delta n_0 + A\cos[2\nabla_y \vartheta + 2\pi\bar{n}(x-1/2)]\\ &+ A\cos[2\nabla_x \vartheta + 2\pi\bar{n}(y-1/2)] \ , \qquad (2.25)\\ \delta\mathcal{B}_{\mathbf{r},\mathbf{r}+\hat{\mathbf{x}}} &= A'\cos[2\nabla_y \vartheta + 2\pi\bar{n}x] \ . \qquad (2.26)\end{aligned}$$

We can also express inter-chain density-density interactions

$$\begin{aligned}V_j n_1(\mathbf{r}) n_1(\mathbf{r}+j\hat{\mathbf{y}}) &\sim V_j\cos\left[2\theta_1(\mathbf{r}) + 2\theta_1(\mathbf{r}+j\hat{\mathbf{y}}) + 4\pi\bar{n}x - 2\pi\bar{n}\right]\\ &+ V_j\cos\left[2\theta_1(\mathbf{r}) - 2\theta_1(\mathbf{r}+j\hat{\mathbf{y}})\right], \qquad (2.27)\end{aligned}$$

where we have only retained cosine terms. Written in terms of the ϑ fields, the first line is non-oscillatory only at half-filling and corresponds to the Umklapp interaction, while the second line is the non-Umklapp interaction.

Let us remark about the effects of compactness of the microscopic gauge field. As is known from the 1D folklore, allowing cosines of the dual fields in the action effectively allows vortices in the microscopic phase variables and provides a faithful treatment of the compactness of the phase variables. In this respect one may wonder about the status of our theory once we allow the described cosine terms in the θ_1 and θ_2 variables. It turns out that it is not complete yet, but becomes so after we allow terms like

$$\mathcal{L}_{\mathfrak{v}} = -\sum_{q=1}^{\infty} \mathfrak{v}_q \cos[q(2\vartheta + 2\pi\bar{n}XY)] \ , \qquad (2.28)$$

which in the parton-gauge setup correspond to allowing monopoles in the microscopic gauge field. Since the insertions Eq. (2.28) have ultra-short-range correlations at the EBL fixed point[18], the issue of monopoles can be safely ignored in the stable EBL theory (but of course they cannot be ignored if the EBL becomes unstable and the parton fields acquire gaps).

2.3 Schwinger boson Spin liquid

The Schwinger boson representation[56] of a spin $\mathbf{S}$ is given by

$$\mathbf{S} = \frac{1}{2}\sum_{\sigma,\sigma'} b^\dagger_\sigma \boldsymbol{\sigma}_{\sigma\sigma'} b_{\sigma'}, \tag{2.29}$$

where $\{b_\sigma,\ \sigma = \uparrow, \downarrow\}$ are bosonic operators and $\boldsymbol{\sigma}$ are the Pauli matrices. The physical Hilbert space lies in the sector with $\sum_\sigma n_\sigma = 2S$. A standard recipe for constructing a spin liquid often begins from a schematic Heisenberg Hamiltonian and follows by a mean-field decoupling which leads to a solvable model. In terms of Schwinger bosons, the spin coupling between sites i and j may be written as

$$\begin{aligned} \mathbf{S}_i \cdot \mathbf{S}_j &= \, : B^\dagger_{ij} B_{ij} : - \, A^\dagger_{ij} A_{ij}, && (2.30) \\ A_{ij} &= \frac{1}{2}\sum_{\sigma,\sigma'} \epsilon_{\sigma\sigma'} b_{i\sigma} b_{j\sigma'}, && (2.31) \\ B_{ij} &= \frac{1}{2}\sum_{\sigma} b^\dagger_{i\sigma} b_{j\sigma}, && (2.32) \end{aligned}$$

where : : denotes normal ordering. The decoupling leads to the mean-field Hamiltonian

$$\begin{aligned} H_{\text{m.f.}} &= \frac{1}{2}\sum_{i,j}\left(\bar{B}^*_{ij} B_{ij} + \bar{B}_{ij} B^\dagger_{ij} - |\bar{B}_{ij}\rangle|^2\right) && (2.33) \\ &- \frac{1}{2}\sum_{i,j}\left(\bar{A}^*_{ij} A_{ij} + \bar{A}_{ij} A^\dagger_{ij} - |\bar{A}_{ij}|^2\right) - \mu \sum_{i,\sigma} b^\dagger_{i\sigma} b_{i\sigma}, \end{aligned}$$

where the chemical potential μ is tuned to fulfill the condition $\sum_\sigma \langle n_{i\sigma}\rangle = 2S$ at each lattice site. The collection of parameters $\{\bar{A}_{ij}\}$ and $\{\bar{B}_{ij}\}$ is treated as an ansatz which determines the type of spin liquid realized by the ground state.

Using Wick's theorem and Eq. (2.29), the spin correlation between sites i and j

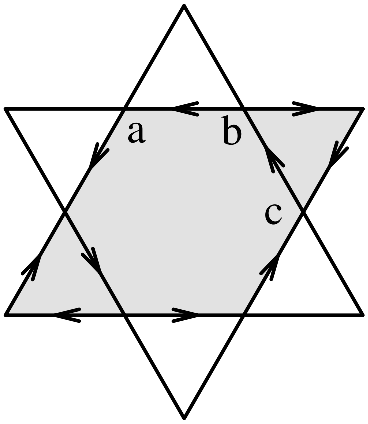

Figure 2.3: The Schwinger boson ansatze from Ref. [40], where $A_{ij} = 1$ if an arrow points from site i to a nearest-neighbor site j, -1 for the opposite direction, and zero for all further neighbors. The shaded region shows a unit cell of the ansatz, and a, b and c label the three bosonic operators in each unit cell.

can be evaluated as follows:

$$\begin{aligned}\langle \mathbf{S}_i \cdot \mathbf{S}_j \rangle &= \langle \mathbf{S}_i \rangle \cdot \langle \mathbf{S}_j \rangle + \frac{1}{2} \sum_{\alpha,\beta} \langle b^\dagger_{i\alpha} b_{j\alpha} \rangle \langle b_{i\beta} b^\dagger_{j\beta} \rangle \qquad (2.34)\\ &+ \frac{1}{4} \sum_{\alpha,\beta,\sigma} \langle b^\dagger_{i\alpha} b^\dagger_{j\beta} + \sigma b^\dagger_{i\beta} b^\dagger_{j\alpha} \rangle \langle b_{i\beta} b_{j\alpha} + \sigma b_{i\alpha} b_{j\beta} \rangle \\ &- \frac{1}{8} \sum_{\alpha,\beta,\sigma} \langle b^\dagger_{i\alpha} b^\dagger_{j\beta} + \sigma b^\dagger_{i\beta} b^\dagger_{j\alpha} \rangle \langle b_{i\alpha} b_{j\beta} + \sigma b_{i\beta} b_{j\alpha} \rangle \\ &- \frac{1}{8} \sum_{\sigma} \langle b^\dagger_{i\uparrow} b_{j\uparrow} + \sigma b^\dagger_{i\downarrow} b_{j\downarrow} \rangle \langle b_{i\uparrow} b^\dagger_{j\uparrow} + \sigma b_{i\downarrow} b^\dagger_{j\downarrow} \rangle \\ &= \frac{3}{2} \left(|\langle B_{ij} \rangle|^2 - |\langle A_{ij} \rangle|^2 \right). \qquad (2.35)\end{aligned}$$

Equation (2.35) suggests that an energy cost is incurred for ansatze with $\bar{B}_{ij} \neq 0$ when considering spin liquids on antiferromagnetic models. In Ref. [57], Wang *et al.* classified all possible Z_2 symmetric spin liquids with A-only ansatze on the kagome lattice allowed by the Projective Symmetry Group analysis and showed that there are only four distinct classes for nearest-neighbor A_{ij}. Below, we study one of the ansatze shown in Fig. 2.3 (first found by Sachdev[40]), which we denote by "$\mathbf{q} = \mathbf{0}$ ansatz."

On the kagome lattice, the mean-field Hamiltonian for the $\mathbf{q} = \mathbf{0}$ ansatz may be written in momentum space as follows:

$$
\begin{aligned}
H &= \sum_{\mathbf{k}} \left[\Psi^\dagger_{\mathbf{k}} \begin{pmatrix} -\mu & iD_{\mathbf{k}} \\ -iD_{\mathbf{k}} & -\mu \end{pmatrix} \Psi_{\mathbf{k}} + 3\mu \right] , \qquad (2.36) \\
D_{\mathbf{k}} &= \frac{i}{2} \begin{bmatrix} 0 & 1+e^{-i\mathbf{k}\cdot\hat{e}_1} & -e^{-i\mathbf{k}\cdot\hat{e}_1} - e^{i\mathbf{k}\cdot\hat{e}_3} \\ -1-e^{i\mathbf{k}\cdot\hat{e}_1} & 0 & 1+e^{i\mathbf{k}\cdot\hat{e}_3} \\ e^{i\mathbf{k}\cdot\hat{e}_1} + e^{-i\mathbf{k}\cdot\hat{e}_3} & -1-e^{-i\mathbf{k}\cdot\hat{e}_3} & 0 \end{bmatrix} , \qquad (2.37) \\
\hat{e}_1 &= \hat{x}, \quad \hat{e}_2 = (\hat{x} + \sqrt{3}\hat{y})/2, \quad \hat{e}_3 = (-\hat{x} + \sqrt{3}\hat{y})/2, \qquad (2.38) \\
\Psi^T_{\mathbf{k}} &= (a_{\mathbf{k}\uparrow},\ b_{\mathbf{k}\uparrow},\ c_{\mathbf{k}\uparrow},\ a^\dagger_{-\mathbf{k}\downarrow},\ b^\dagger_{-\mathbf{k}\downarrow},\ c^\dagger_{-\mathbf{k}\downarrow}), \qquad (2.39)
\end{aligned}
$$

where a, b and c are the three bosonic annihilation operators in each unit cell of the kagome lattice (see Fig. 2.3). The Hamiltonian can be simplified further by applying a 3×3 unitary transformation $M_{\mathbf{k}}$ on $D_{\mathbf{k}}$ which gives

$$
\begin{aligned}
H &= \sum_{\mathbf{k},\gamma=a,b,c} \left[\begin{pmatrix} \tilde{\gamma}_{\mathbf{k}\uparrow} \\ \tilde{\gamma}^\dagger_{-\mathbf{k}\downarrow} \end{pmatrix}^\dagger \begin{pmatrix} -\mu & i\lambda_{\mathbf{k}\tilde{\gamma}} \\ -i\lambda_{\mathbf{k}\tilde{\gamma}} & -\mu \end{pmatrix} \begin{pmatrix} \tilde{\gamma}_{\mathbf{k}\uparrow} \\ \tilde{\gamma}^\dagger_{-\mathbf{k}\downarrow} \end{pmatrix} + \mu \right] , \qquad (2.40) \\
\tilde{\gamma}_{\mathbf{k}\uparrow} &= \sum_{\alpha=a,b,c} (M_{\mathbf{k}})_{\tilde{\gamma}\alpha}\, \alpha_{\mathbf{k}\uparrow}, \quad \tilde{\gamma}^\dagger_{-\mathbf{k}\downarrow} = \sum_{\alpha=a,b,c} (M_{\mathbf{k}})_{\tilde{\gamma}\alpha}\, \alpha^\dagger_{-\mathbf{k}\downarrow} , \qquad (2.41) \\
\Lambda_{\mathbf{k}} &= \mathrm{diag}(\lambda_{\mathbf{k}\tilde{\gamma}}) \ = \ M_{\mathbf{k}} D_{\mathbf{k}} M^\dagger_{\mathbf{k}} . \qquad (2.42)
\end{aligned}
$$

It is now straightforward to diagonalize the Hamiltonian using a 2×2 Bogoliubov's transformation and we obtain the following excitation spectrum:

$$
\epsilon^{(1)}_{\mathbf{k}} = |\mu|, \quad \epsilon^{(2)}_{\mathbf{k}} = \epsilon^{(3)}_{\mathbf{k}} = \sqrt{\mu^2 - \left[3 + \cos(\mathbf{k}\cdot\hat{e}_1) + \cos(\mathbf{k}\cdot\hat{e}_2) + \cos(\mathbf{k}\cdot\hat{e}_3)\right]/2} \, . \qquad (2.43)
$$

The spinon spectrum is gapped for $\mu < -\sqrt{3}$ and the $\mathbf{q} = \mathbf{0}$ ansatz realizes a spin liquid wave function. As $\mu \to -\sqrt{3}$, the energy gap vanishes, causing the spinons to condense and resulting in a magnetically ordered state. By requiring that the expectation of the total boson density at each lattice is equal to $2S$, we obtain

$$
S = \frac{1}{3N} \sum_{\mathbf{k}} \left(-1 + \frac{|\mu|}{\epsilon^{(2)}_{\mathbf{k}}} \right) \leq 0.25 \, . \qquad (2.44)
$$

This suggests that the spin liquid phase may not be accessible to spin-1/2 systems. However, the mean-field level treatment is too crude to predict accurately the critical value of S that separates the magnetically ordered phase for large spins from the spin-disordered phase for small spins. In Chapter 6, we improve upon the mean-field treatment by applying a Gutzwiller projection to enforce the stricter constraint $\sum_\sigma n_\sigma = 2S$ at each site. We study the energetics of the projected Schwinger boson wave functions in the spin-1/2 Heisenberg antiferromagnetic model with first- and second-neighbor couplings.

2.4 Quantum Monte Carlo Techniques

Quantum Monte Carlo (QMC) is a class of algorithms widely used to simulate many-body systems in physics. It allows us to study problems where analytically exact solutions or well-controlled approximations are not available. For unfrustrated strongly correlated models in two dimensions or higher, QMC is often the method of choice for obtaining unbiased information on the ground state or finite temperature properties and is therefore an invaluable tool. The essential ingredient of QMC algorithms is the stochastic approach of sampling important configurations in systems with large number of degrees of freedom.

Different flavors of QMC algorithms exist, for example, variational Monte Carlo (VMC), Diffusion Monte Carlo (DMC), Green's Function Monte Carlo (GFMC), Path Integral Monte Carlo (PIMC), and Stochastic Series Expansion (SSE). In this thesis, we make extensive use of the VMC to investigate the ground state properties of a number of quantum lattice models. In the absence of frustration, where QMC does not suffer from the well-known sign problem, we set up a GFMC simulation which provides exciting evidence that a concrete realization of the exotic Bose Liquid phase may be possible in a hard-core boson model with ring-exchange interaction. In the remainder of this section, we review the VMC and GFMC techniques employed in this thesis.

2.4.1 Variational Monte Carlo

The variational Monte Carlo (VMC) approach relies on the variational principle, which states that the average energy E_T of any trial wave function Ψ_T provides an upper bound to the exact ground state energy E_0 of a system

$$E_0 \leq E_T = \frac{\langle \Psi_T | H | \Psi_T \rangle}{\langle \Psi_T | \Psi_T \rangle}, \tag{2.45}$$

and this forms the basis for the variational approach. By itself, VMC does not provide an exact solution of the problem but it instead allows one to identify a candidate ground state among competing wave functions. This is very useful in many problems where other unbiased QMC techniques fail due to the sign problem. In addition, it is often possible to implement contraints such as hard-core repulsion in wave functions where approximate treatments are rather crude. Thus, the VMC allows us to obtain reliable upper bounds using trial wave functions that lie in the physical Hilbert space.

We apply the VMC technique to study the energetics of a variety of quantum phases ranging from insulator to magnetic orderings, spin liquids, and bose liquids. To assess the accuracy of a trial state, it is often useful to determine where the trial energy lies in relation to the exact diagonalization spectrum:

$$|\Psi_T\rangle = \sum_i a_i|E_i\rangle, \qquad \sum_i |a_i|^2 = 1, \tag{2.46}$$

$$\frac{E_T - E_0}{E_1 - E_0} = \frac{\sum_i |a_i|^2(E_i - E_0)}{E_1 - E_0} \geq \sum_{i>0} |a_i|^2. \tag{2.47}$$

Equation (2.47) shows that it is necessary for the trial energy of a variational wave function to be close to the ground state energy compared to the excitation gap in order to achieve a good overlap with the true ground state. However, it is important to note that the accuracy of other measurements such as correlation functions may not be satisfactory since variational energies are mainly sensitive to the local energetics[58].

The expectation value of an operator $\mathcal{O}$ can be computed stochastically for a given trial state $|\Psi_T\rangle$ as follows:

$$\langle\mathcal{O}\rangle = \frac{\sum_x \langle\Psi_T|\mathcal{O}|x\rangle\langle x|\Psi_T\rangle}{\sum_x \langle\Psi_T|x\rangle\langle x|\Psi_T\rangle} = \sum_x p_x \mathcal{O}_x, \tag{2.48}$$

$$p_x = \frac{\langle\Psi_T|x\rangle\langle x|\Psi_T\rangle}{\sum_{x'}\langle\Psi_T|x'\rangle\langle x'|\Psi_T\rangle}, \quad \mathcal{O}_x = \frac{\langle\Psi_T|\mathcal{O}|x\rangle}{\langle\Psi_T|x\rangle}, \tag{2.49}$$

where $|x\rangle$ is a basis vector in the Hilbert space. The probability distribution $\{p_x\}$ can be statistically sampled by generating a markov chain $\{x_\tau\}$ using the metropolis algorithm, where an arbitrary configuration is selected at a time step τ and accepted with probability $\min(1, \frac{|\langle x_\tau|\Psi_T\rangle|^2}{|\langle x_{\tau-1}|\Psi_T\rangle|^2})$. The expectation value of the operator becomes

$$\langle\mathcal{O}\rangle = \frac{1}{M}\sum_{\tau=1}^{M} \mathcal{O}_{x_\tau}. \tag{2.50}$$

This simple formulation allows us to study a large number of problems in quantum many-body systems.

2.4.2 Green's Function Monte Carlo

The Green's function Monte Carlo (GFMC) is a projector method used for studying the ground state properties of many-body quantum systems. Starting from an initial trial wave function with a sufficiently good overlap with the ground state of a system, a projection operator G is applied repeatedly to the trial wave function to filter out the excited states:

$$|\psi_{\mathrm{g}}\rangle = \lim_{n\to\infty} G^n|\psi_T\rangle. \tag{2.51}$$

This iterative procedure is also known as the power method which singles out the eigenvector of G with the largest eigenvalue as $n \to \infty$. Possible choices of the operator G include $\exp(-H\delta\tau)$ and $1-(H-E_r)\delta\tau$, where E_r and $\delta\tau$ are chosen to ensure that the desired state is projected out. As with other Quantum Monte Carlo techniques, the GFMC can be used only if there is no sign problem, i.e., the matrix elements of G are all positive in a known basis.

We now review Hetherington's GFMC scheme[59] for calculating the expectation of the energy:

$$\begin{aligned}\langle H_n\rangle &= \frac{\langle\Psi_T|HG^n|\phi\rangle}{\langle\Psi_T|G^n|\phi\rangle}, &(2.52)\\ &= \frac{\sum_x E_x\langle\Psi_T|x\rangle\langle x|G^n|\phi\rangle}{\sum_x\langle\Psi_T|x\rangle\langle x|G^n|\phi\rangle}, &(2.53)\end{aligned}$$

where $|\phi\rangle$ is a starting wave function for the projection and E_x is the "local energy" defined in Eq. (2.49). In the limit $n \to \infty$, $\langle H_n\rangle$ converges to the exact ground state energy. Defining

$$G_{xy} = \langle x|G|y\rangle, \quad \phi(x) = \langle x|\phi\rangle, \tag{2.54}$$

and

$$\tilde{G}_{xy} = \langle\Psi_T|x\rangle G_{xy}/\langle\Psi_T|y\rangle, \tag{2.55}$$

the energy becomes

$$\langle H_n\rangle = \frac{\sum_{\{x_i\}} E_{x_n}\tilde{G}_{x_n x_{n-1}}\cdots\tilde{G}_{x_1 x_0}\Psi_T(x_0)\phi(x_0)}{\sum_{\{x_i\}}\tilde{G}_{x_n x_{n-1}}\cdots\tilde{G}_{x_1 x_0}\Psi_T(x_0)\phi(x_0)}. \tag{2.56}$$

To see how Eq. (2.56) can be evaluated stochastically, note that the non-negative matrix $\tilde{G}$ can be decomposed into the product of a diagonal matrix and a stochastic matrix $\tilde{K}_{xy} = \tilde{G}_{xy}/b_y$ with $b_y = \sum_x \tilde{G}_{xy}$. Equation (2.56) now becomes

$$\langle H_n \rangle = \frac{\sum_{\{x_i\}} E_{x_n} \tilde{K}_{x_n x_{n-1}} b_{x_{n-1}} \cdots b_{x_0} P(x_{n-1}, \cdots, x_0)}{\sum_{\{x_i\}} b_{x_{n-1}} \cdots b_{x_0} P(x_{n-1}, \cdots, x_0)}, \tag{2.57}$$

where $P(x_{n-1}, \cdots, x_0) = \tilde{K}_{x_{n-1}x_{n-2}} \cdots \tilde{K}_{x_1 x_0} \Psi_T(x_0)\phi(x_0)$ may be interpreted as the probability distribution for sampling the path $\{x_{n-1}, \cdots, x_0\}$, and $\tilde{K}_{x_n x_{n-1}}$ is the probability for sampling the next configuration, x_n. In a Monte Carlo implementation, the stochastic matrix $\tilde{K}$ is used to generate a markov chain of states starting from an initial configuration state. For example, to evolve from a configuration x to the next time step, we first list all possible configurations $\{y\}$ with $\tilde{K}_{yx} \neq 0$. We then compute the cumulative probabilities $F(y_j) = \sum_{i \leq j} \tilde{K}_{y_i x}$ and select the new configuration based on a uniform random number drawn from the interval $[0, 1]$. Equation (2.55) shows that importance sampling can be achieved by using a $|\Psi_T\rangle$ that has good overlap with the ground state so that configurations with higher weights are sampled more often. The local energy E_x and the weighting factor b_x required for the calculation of the energy are tabulated at each time step during the simulation. The energy is computed using

$$\langle H_n \rangle = \frac{\sum_\tau E_{x_\tau} b_{x_{\tau-1}} \cdots b_{x_{\tau-n+1}}}{\sum_\tau b_{x_{\tau-1}} \cdots b_{x_{\tau-n+1}}}, \tag{2.58}$$

and evaluating it for different n allows us to check for convergence in the simulation.

Next, we consider an ensemble of random walkers propagating simultaneously. To generalize the previous results to the many-walker case[60], we define the following for a single walker

$$P_n(\omega, x) = \sum_{\{x_i\}} \delta(x_n - x)\delta(b_{x_{n-1}} \cdots b_{x_0} - \omega)\tilde{K}_{x_n x_{n-1}} \cdots \tilde{K}_{x_1 x_0} \Psi_T(x_0)\phi(x_0), \tag{2.59}$$

and obtain the following forms for the single-walker case:

$$P_n(\omega, x) = \sum_{x'} \tilde{K}_{x,x'} P_{n-1}(\omega/b_{x'}, x'), \tag{2.60}$$

$$\langle H_n \rangle = \frac{\sum_{\omega,x} E_x \, \omega P_n(\omega, x)}{\sum_{\omega,x} \omega P_n(\omega, x)}. \tag{2.61}$$

Here, ω is the product of the weights b's accumulated by a walker along the path $\{x_0, \cdots, x_{n-1}\}$. The probability distribution $P_n(\omega, x)$ of the walker's configuration (ω, x) evolves according to the stochastic matrix $\tilde{K}$ in Eq. (2.60). For M independent and identically distributed walkers, Eq. (2.61) generalizes to

$$\langle H_n \rangle = \frac{\sum_{j=1}^{M} \langle \omega_j E_{x_j} \rangle}{\sum_{j=1}^{M} \langle \omega_j \rangle}, \tag{2.62}$$

where the averaging is taken with respect to $P_n(\vec{\omega}, \vec{x}) = P_n(\omega_1, x_1) \cdots P_n(\omega_M, x_M)$. The independent-walkers formulation is equivalent to the single-walker case, and thus offers no improvement. By allowing stochastic reconfigurations such that irrelevant (relevant) walkers with small (large) weights are instead eliminated (duplicated) with probabilities depending on their weights, an additional form of importance sampling can be realized.

Hetherington[59] introduced the following reconfiguration for a fixed number of walkers:

$$P_n'(\vec{\omega}', \vec{x}') = \sum_{\vec{\omega}, \vec{x}} P_n(\vec{\omega}, \vec{x}) \prod_{i=1}^{M} \frac{\sum_j \omega_j \delta_{x_j x_i'}}{\sum_j \omega_j} \delta\left(\omega_i' - \frac{\sum_j \omega_j}{M}\right), \tag{2.63}$$

which was shown by Buonaura *et al.*[60] to introduce no bias in simulations, i.e., the energy is still given by Eq. (2.62) after each reconfiguration. Buonaura *et al.* implemented the reconfiguration using the following scheme. For a given set of M walkers and their corresponding weights $\{w_i\}$, generate a random permutation σ and define $p_j = \xi + \sum_{i=1}^{j} \omega_{\sigma(i)} / \sum_{i=1}^{M} \omega_i$ up to modulo one, where ξ is a random number in (0,1). The new set of walkers after reconfiguration is selected by counting the number of points from the set $\{k/M,\ k = 1, \cdots, M\}$ which lie in the intervals (p_{j-1}, p_j). By performing the fixed-population reconfigurations at regular intervals in a simulation, this scheme overcomes the problem of exponential growth or decay in population size which results from the "birth-death" process in an earlier GFMC scheme[61] where each walker is independently allowed to be duplicated or eliminated.

The preceding GFMC formulation can be used to calculate the expectation value of an operator only if the ground state is an eigenstate of the operator. For a generic operator such as an order parameter, a more elaborate technique known as forward walking must be used since "double-projection" is required, i.e., both the bra and ket vectors that sandwich the operator must be the ground state vector. Here, we review Buonaura *et al.*'s forward walking technique with bias-free reconfiguration[60] which we adopted for our work in Chapter 4. For a single walker,

$$\begin{aligned}
\langle \Psi_T | G^n \mathcal{O} | \psi_{\mathrm{g}} \rangle &= \sum_{\{x_i\}} b_{x_{n-1}} \cdots b_{x_0} \mathcal{O}_{x_0} \tilde{K}_{x_n x_{n-1}} \cdots \tilde{K}_{x_1 x_0} \Psi_T(x_0) \psi_{\mathrm{g}}(x_0), && (2.64) \\
&= \sum_{\omega,\gamma,x} \omega \gamma P_n(\omega, \gamma, x), && (2.65) \\
\langle \Psi_T | G^n | \psi_{\mathrm{g}} \rangle &= \sum_{\{x_i\}} b_{x_{n-1}} \cdots b_{x_0} \tilde{K}_{x_n x_{n-1}} \cdots \tilde{K}_{x_1 x_0} \Psi_T(x_0) \psi_{\mathrm{g}}(x_0), && (2.66) \\
&= \sum_{\omega,\gamma,x} \omega P_n(\omega, \gamma, x), && (2.67) \\
\langle \mathcal{O} \rangle &\approx \frac{\langle \Psi_T | G^n \mathcal{O} | \psi_{\mathrm{g}} \rangle}{\langle \Psi_T | G^n | \psi_{\mathrm{g}} \rangle} = \frac{\langle \omega \gamma \rangle}{\langle \omega \rangle}, && (2.68)
\end{aligned}$$

where $P_n(\omega, \gamma, x) = \sum_{\{x_i\}} \delta(b_{x_{n-1}} \cdots b_{x_0} - \omega) \delta(\mathcal{O}_{x_0} - \gamma) \tilde{K}_{x, x_{n-1}} \cdots \tilde{K}_{x_1 x_0} \Psi_T(x_0) \psi_{\mathrm{g}}(x_0)$, $|\psi_{\mathrm{g}}\rangle$ is the ground state of the system, and the averaging in Eq. (2.68) is taken over $P_n(\omega, \gamma, x)$. Equation (2.68) becomes exact in the limit $n \to \infty$. The probability distribution $P_n(\omega, \gamma, x)$ evolves according to

$$P_n(\omega, \gamma, x) = \sum_{x'} \tilde{K}_{x,x'} P_{n-1}(\omega / b_{x'}, \gamma, x'). \tag{2.69}$$

For the case of M random walkers, the forward walking result in Eq. (2.68) generalizes to the following:

$$\langle \mathcal{O} \rangle = \frac{\sum_{j=1}^{M} \langle \omega_j \gamma_j \rangle}{\sum_{j=1}^{M} \langle \omega_j \rangle}, \tag{2.70}$$

where the averaging is taken over the many-walker distribution

$$P_n(\vec{\omega}, \vec{\gamma}, \vec{x}) = P_n(\omega_1, \gamma_1, x_1) \cdots P_n(\omega_M, \gamma_M, x_M). \tag{2.71}$$

Just as reconfiguration is important for reducing the statistical errors in the energy calculation, this is even more so for forward walking since the relative weights of individual walkers diverge rapidly with the number of forward time steps n in Eqs. (2.64) and (2.66). Buonaura *et al.*[60] introduced the following forward walking bias-free reconfiguration for a fixed number of walkers:

$$P_n'(\vec{\omega}', \vec{\gamma}', \vec{x}') = \sum_{\vec{\omega}, \vec{\gamma}, \vec{x}} P_n(\vec{\omega}, \vec{\gamma}, \vec{x}) \prod_{i=1}^{M} \frac{\sum_j \omega_j \delta_{x_i' x_j}}{\sum_j \omega_j} \delta\left(\omega_i' - \frac{\sum_j \omega_j}{M} \right) \delta\left(\frac{\sum_j \omega_j \gamma_j \delta_{x_i' x_j}}{\sum_j \omega_j \delta_{x_i' x_j}} - \gamma_i' \right). \tag{2.72}$$

In a forward walking simulation, the lineage of each walker is recorded and just before a reconfiguration takes place, all but one walker among those having identical present configuration x are discarded, and the remaining walker acquires the total weight of the walkers that had the same configuration. The new set of M walkers is then sampled from the reduced set of walkers analogous to the non-forward-walking case used for calculating the energy.

Note that the ground state $|\psi_{\mathrm{g}}\rangle$ used in Eq. (2.64) requires that the accumulated weight w comprises a product of b's that includes not only the n forward steps but also an appropriate number of backward steps, say m. The expectation of an operator $\mathcal{O}$ therefore has the following form

$$\langle \mathcal{O}_{n,m} \rangle = \frac{\sum_{\tau} \gamma_{x_\tau} b_{x_{\tau-1}} \cdots b_{x_{\tau-n-m+1}}}{\sum_{\tau} b_{x_{\tau-1}} \cdots b_{x_{\tau-n-m+1}}}. \tag{2.73}$$

To minimize statistical errors in a GFMC calculation, it is important to perform a preliminary VMC study to identify a good starting wave function $|\Psi_T\rangle$ that has considerable overlap with the ground state. It is also important to monitor $\langle \mathcal{O}_{n,m} \rangle$ for different number of backward steps m and forward steps n to ensure that convergence has been achieved.

Chapter 3

Heisenberg antiferromagnet on triangular lattice

3.1 Introduction

The spin-1/2 Heisenberg antiferromagnet on a spatially anisotropic 2D triangular lattice is an apparently simple spin system which nevertheless possesses very rich physics. Despite having attracted much attention, a complete understanding of the model has not been achieved. This can be attributed to the enhanced quantum fluctuations arising from a combination of low dimensionality, small spin, geometrical frustration and spatial anisotropy, thus leading to a rich phase diagram. At zero field, studies have suggested that the anisotropic system may possibly remain disordered even at zero temperature[62, 15]. In experimental realizations of the triangular antiferromagnet, a 1/3-magnetization plateau was found for the approximately isotropic material Cs_2CuBr_4 but not for the more anisotropic Cs_2CuCl_4[8, 63, 64, 65, 66, 67]. A recent experimental study of Cs_2CuBr_4 further revealed a cascade of phases in the fields above the 1/3 plateau, which are still not understood[9].

Analytical studies on the model have focused on specific regions of the phase diagram, for instance low anisotropy near the 1/3-magnetization plateau[7, 10], large anisotropy limit[13], and high field limit[11, 12]. Several numerical studies using exact diagonalization[68, 69, 70, 71], series expansion[72, 73], density matrix renormalization group[17, 74], and variational approaches have also been used to analyze the model[14, 16, 62, 15]. Motivated by the experimental and theoretical works, we perform a variational study using simple yet accurate wave functions, attempting to cover a wide region of the phase diagram.

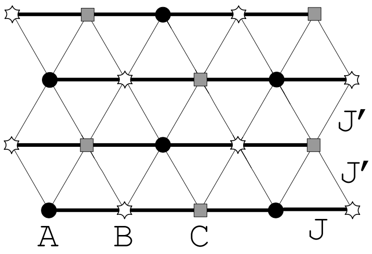

Figure 3.1: Triangular antiferromagnet with coupling constants J and J' between nearest-neighbors along horizontal and oblique directions, respectively. Three sublattices A, B, and C important in the isotropic case are also labelled.

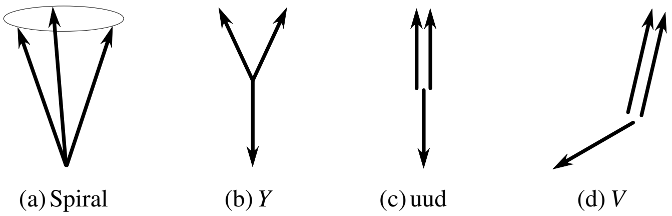
(a) Spiral (b) Y (c) uud (d) V

Figure 3.2: Spin orderings on the isotropic triangular lattice in the field, where three arrows refer to three sublattices indicated in Fig. 3.1: a) spiral (non-coplanar umbrella); b, c, d) coplanar Y, uud, and V.

We consider the Heisenberg model in external magnetic field h,

$$\hat{H} = \sum_{\langle rr' \rangle} J_{rr'} \, \mathbf{S}_r \cdot \mathbf{S}_{r'} - \vec{h} \cdot \sum_r \mathbf{S}^z_r \,, \tag{3.1}$$

where $\mathbf{S}_r$ is the spin operator on site r and $J_{rr'}$ are the nearest-neighbor exchange couplings. Throughout, we extensively use a hard-core boson picture, mapping $S^+_r = b_r$ and $S^z_r = \frac{1}{2} - n_r$:

$$\hat{H} = -\sum_{\langle rr' \rangle} t_{rr'} \left(b^\dagger_r b_{r'} + \text{H.c.} \right) + \sum_{\langle rr' \rangle} J_{rr'} n_r n_{r'} - \mu \sum_r n_r + \text{const} \,, \tag{3.2}$$

$$t_{rr'} = -\frac{1}{2} J_{rr'}, \quad \mu = -h + \frac{1}{2} \sum_{r' \in r} J_{rr'} \,. \tag{3.3}$$

The boson hopping amplitudes are negative and therefore frustrated on the triangular lattice, making this a challenging interacting problem.

Figure 3.2 depicts spin-ordered phases considered in this variational study. While these are simple to draw, realizing them as wave functions is non-trivial. The spiral phase is a boson superfluid containing rotating phase angles (see Fig. 3.3a) and is cap-

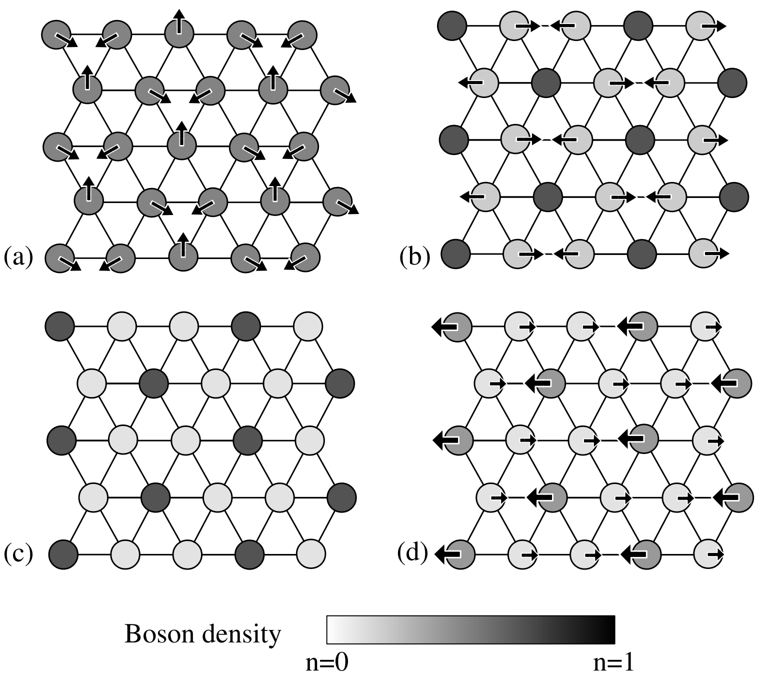

Figure 3.3: Boson interpretation of the spin orderings in Fig. 3.2. Gray scale shows density order $\langle n_r \rangle$, while arrows show superfluid order $\langle b_r^\dagger \rangle$. a) Spiral is a uniform superfluid phase with rotating phase angles; c) *uud* is a Mott insulator with $\sqrt{3} \times \sqrt{3}$ CDW order; b,d) Y and V are supersolid phases which contain both charge density and particular superfluid orderings.

tured by an elegant Huse-Elser generalization of the Bijl-Jastrow wave function[14]. For the other phases, constructing simple and yet accurate wave functions is not straightforward and requires consideration of their physical nature in terms of bosons. Thus, the *uud* is a Mott insulating phase (see Fig. 3.3c) which requires a wave function with strongly localized bosons and rapidly decaying correlations. The Y phase is an interesting supersolid phase (see Fig. 3.3b) with rapidly decaying boson correlations between sites on one of the three sublattices as well as long-range correlation between sites on the other two sublattices. The V phase is a different supersolid (see Fig. 3.3d) with long-range boson correlations between all sites; here we find that two different constructions of the trial wave functions are required to capture the lower and higher density regimes. (Supersolid phases of bosons on the half-filled triangular lattice and in the presence of strong repulsion have been of much recent interest[75, 74, 62].) In Section 3.2, we present simple, few-parameter candidate wave functions used in our isotropic study. Encouraged by the accuracy of these candidates, we generalize the wave functions to incommensurate counterparts for our anisotropic study in Section 3.3. We conclude with a discussion of the results and implications for $\mathrm{Cs_2CuBr_4}$

in Section 3.4.

3.2 Isotropic triangular antiferromagnet: 6×6 Study

In this section, we consider the isotropic triangular Heisenberg antiferromagnet with $J_{rr'} = J$ for all nearest-neighbor links. Beginning at density $n = 1/3$, where we have an excellent wave function for the *uud* Mott insulator phase of Fig. 3.3c, we construct similarly inspired wave functions for nearby supersolid phases of Figs. 3.3b,d. Next, we describe Bijl-Jastrow-type wave functions for the spiral of Fig. 3.3a and V supersolid of Fig. 3.3d, which perform better for n further from 1/3. We also discuss an alternative construction of the *uud* state using a $\det \times \det$ ("2-parton") trial wave function. For the ED calculations, we compute ground state energies for $N_b \leq 12$, while $N_b \geq 13$ data is taken from Bernu *et al.*[68].

We perform all studies at fixed boson number N_b. For each wave function below, we also include a Jastrow factor

$$\text{Jastrow}(\{n_r\}) = e^{-\frac{1}{2}\sum_{r,r'} u_{rr'} n_r n_{r'}} \tag{3.4}$$

with simple choices of pseudopotentials $u_{rr'}$ providing additional variational freedom.

3.2.1 *uud* state at $n = 1/3$

At density $n = 1/3$, the *uud* phase is stabilized by quantum fluctuations. We construct a simple boson wave function by using $N_b = N/3$ orbitals localized around sites A_j, $j = 1 \ldots N/3$, from sublattice A:

$$|\psi_{uud}\rangle = \prod_{j=1}^{N/3} \left(\sum_r \phi_j^{\text{loc}}(r) b_r^\dagger \right) |0\rangle \, , \tag{3.5}$$

$$\phi_j^{\text{loc}}(r) = \begin{cases} 1, & r = A_j \\ -\alpha, & r = \text{neighbor of } A_j \\ 0, & \text{otherwise} \end{cases} \, , \tag{3.6}$$

$$\langle \{r_k\} | \psi_{uud} \rangle = \text{Perm}\left[\phi_j^{\text{loc}}(r_i) \right] \, . \tag{3.7}$$

For $\alpha = 0$ this reduces to the classical CDW state with bosons strictly localized on the A sublattice and minimizing the potential energy. Non-zero α allows bosons to hop to nearest-neighbor sites and gain some kinetic energy; $\alpha > 0$ is appropriate for

Trial state	N^{orb}_{par}	N^{Jas}_{short}	N^{Jas}_{long}	N^{tot}_{par}	E/bond
classical					-0.0833
spiral	0	1	2	4	-0.1265
uud	1	0	0	1	-0.1347
	1	1	0	2	-0.1354
	1	2	0	3	-0.1355
exact					-0.1361

Table 3.1: Comparison of *uud* trial energies for different number of short-range Jastrow parameters for 12 bosons on a 6×6 cluster. Localized orbitals in the permanent extend only to nearest-neighbor sites with amplitude α, which is single variational parameter in the first listed *uud* case. The second *uud* case has one nearest-neighbor (nnb) Jastrow pseudopotential which is taken to be the same between any pair of nnb sites, while the third case has two such parameters, one for $A-B$ and $A-C$ nnb pairs and the other for $B-C$ nnb pairs, as is appropriate given lattice symmetries of the *uud* state. We also show trial energy for the spiral state with 4 variational parameters (same as in table 3.3); this state performs poorly compared to the *uud* state.

boson hopping $t_{rr'} < 0$. In Eq. (3.7), column j of the Permanent matrix is given by the j-th orbital (centered on A_j) evaluated on the occupied sites $\{r_i\}$[76]. One can loosely connect this wave function with a picture starting from the "Ising" limit, $J^z \gg |t|$, and perturbatively building in boson kinetic energy effects[72].

Table 3.1 compares the trial energies for different number of variational parameters. Excluding any Jastrow factor, the single-parameter trial state already captures the important exchange energies; for example, it is closer to the exact ground state in the zero momentum sector than to the first excited state in this sector (not shown)[68]. Adding a short-range Jastrow factor further improves the trial energy, while longer-range Jastrow parameters are unimportant since correlations in the Mott insulator decay rapidly (see Fig. 3.11 in Appendix 3.B). We see that the simplest localized orbitals extending only to nearest-neighbor sites (and with relatively small amplitude $\alpha \sim 0.23$) perform very well, which suggests strong *uud* order in the 1/3-filled system. Indeed, for the optimal wave function, we calculate the boson density to be 0.76 on A sites and 0.12 on BC sites.

3.2.2 Y state at $n \gtrsim 1/3$

Starting from the *uud* wave function where we have good exchange energies between sublattices A and BC, we construct a candidate for the Y supersolid phase by adding

Trial state	$N^{\mathrm{orb}}_{\mathrm{par}}$	$N^{\mathrm{Jas}}_{\mathrm{short}}$	$N^{\mathrm{Jas}}_{\mathrm{long}}$	$N^{\mathrm{tot}}_{\mathrm{par}}$	E/bond
classical					-0.0961
spiral	0	1	2	4	-0.1424
Y	1	0	0	1	-0.1461
	1	1	0	2	-0.1477
	1	2	0	3	-0.1478
exact					-0.1489

Table 3.2: Comparison of Y trial energies for different number of short-range Jastrow parameters for 13 bosons on a 6×6 cluster. The Y state is constructed by adding one boson to the *uud* state as described in the text; we allowed the same variational parameters as in the *uud* case in Table 3.1. We also show trial energy for the spiral state with 4 variational parameters, which has higher energy than the Y state.

bosons to an extended orbital on BC:

$$|\psi_Y\rangle = \left(\sum_r \phi^{\mathrm{ext}}_{BC}(r) b^\dagger_r\right)^{N_b - N/3} |\psi_{uud}\rangle \ , \tag{3.8}$$

$$\phi^{\mathrm{ext}}_{BC}(r) = \begin{cases} +1, & r \in B \\ -1, & r \in C \\ 0, & r \in A \end{cases} \tag{3.9}$$

Just as in the *uud* case, the wave function can be written as an $N_b \times N_b$ permanent. The first $N/3$ columns contain the same ϕ^{loc}_j orbitals as in the *uud* state, while the remaining $N_b - N/3$ columns all contain the extended orbital ϕ^{ext}_{BC} residing on the B and C sublattices. The alternating signs of the extended orbital are appropriate for bosons hopping on the BC honeycomb with $t_{rr'} < 0$. Nearest-neighbor contacts on BC are suppressed by adding a Jastrow factor.

Table 3.2 compares the Y energy against spiral and ED energies for 13 bosons on the 6×6 cluster. Our Y state is close to the ED ground state from Bernu *et al.*[68]; thus, the trial energy is below the first excited state in the same sector (not shown), while the spiral is significantly higher.

We consider such Y states for all boson densities above 1/3 and find them to give lowest trial energies among all our states for $N_b = 13, \ldots, 15$. We discuss properties of the Y states in Appendix 3.B. Here we note an interesting feature that boson correlations are long-ranged for B and C sublattice sites but are short-ranged for A sites. The A sublattice remains "Mott-insulating" despite the superfluid on the BC honeycomb. The absence of the "proximity effect" on the A sublattice is due to can-

Trial state	N^{orb}_{par}	N^{Jas}_{short}	N^{Jas}_{long}	N^{tot}_{par}	E/bond
classical					-0.1250
Y	1	1	2	4	-0.1774
spiral	0	1	0	1	-0.1728
	0	1	0	2	-0.1791
	0	1	2	4	-0.1795
exact					-0.1868

Table 3.3: Comparison of spiral energies for different number of variational parameters for 18 bosons on a 36-site cluster. The extended orbital of the spiral state has amplitudes 1, $e^{i2\pi/3}$, and $e^{i4\pi/3}$ for sites on sublattices A, B, and C respectively. The first spiral case has one nnb Jastrow pseudopotential which is taken to be the same between any pair of nnb sites, while the second spiral case has an additional parameter γ for the Huse-Elser phase factor. The third case has two more parameters w and p for a long-range pseudopotential $\frac{w}{|i-j|^p}$ between any pair of sites i and j. We also show trial energy for the Y state with 4 variational parameters, which has slightly higher energy than the spiral state.

cellations from alternating superfluid order parameter on the B and C sublattices[75]. In particular, just as in the *uud* case, we can not construct Bijl-Jastrow-type wave function for the Y state.

3.2.3 Spiral state at $n \lesssim 1/2$

At half-filling, the 120° magnetically ordered state (spiral) is believed to be the ground state. We use Huse and Elser wave function[14], which generalizes Bijl-Jastrow-type wave function by including complex 3-body terms, to accurately describe the corresponding superfluid state of bosons near half-filling. In this wave function, all the bosons reside on an extended orbital,

$$|\psi_S\rangle = e^{i\sum_{ijk}\gamma_{ijk}\; n_i n_j n_k} \left(\sum_r e^{i\vec{Q}\cdot\vec{r}}\; b^\dagger_r \right)^{N_b} |0\rangle, \tag{3.10}$$

with $\vec{Q} = (4\pi/3, 0)$. Despite frustration, the bosons gain some kinetic energy while hopping along any lattice link. Nearest-neighbor contacts are suppressed by adding a long-range Jastrow factor. The three-body phase factor, which respects the symmetries of the classical state, serves as an additional variational parameter. For details, the reader is referred to the original Ref. [14].

Among our trial states, the Huse-Elser wave function has lower energy than the Y state for $N_b = 16, \ldots, 18$, but only by a very small amount. Table 3.3 shows

Trial state	$N^{\rm orb}_{\rm par}$	$N^{\rm Jas}_{\rm short}$	$N^{\rm Jas}_{\rm long}$	$N^{\rm tot}_{\rm par}$	E/bond
classical					-0.0683
spiral	0	1	2	4	-0.1081
$V_{\rm perm}$	1	0	0	1	-0.1141
	1	1	0	2	-0.1153
	1	2	0	3	-0.1154
exact					-0.1161

Table 3.4: Comparison of $V_{\rm perm}$ energies for different number of variational parameters for 11 bosons on a 36-site cluster. The $V_{\rm perm}$ state is constructed by removing one boson from the *uud* state as described in the text, and the parameters here are of the same type as in the *uud* case in Table I. We also show trial energy for the spiral state with 4 variational parameters, which has higher energy than the $V_{\rm perm}$ state.

that the 18-boson spiral energy is only slightly lower than the Y energy. This is perhaps not surprising since the classical 120° order may be viewed as the spiral or Y-shape order depending on the plane's orientation. A recent variational study using different constructions of the spiral and Y states obtained -0.1827 for their many-parameter spiral state, which is also lower than their Y trial energy by a small amount similar to that in our study[62]. Other recent works[75, 74] observed an abrupt change from the spiral to Y supersolid as the spin anisotropy is varied through the Heisenberg point. In principle, thinking in terms of wave functions, the spiral and Y can be distinct phases with different postulated symmetry breaking also in the SU(2)-invariant model. However, this could also be a plane reorientation transition, and the closeness in energy of the Y trial states reflecting their ability to capture the 120° spiral order.

3.2.4 V state at $n \lesssim 1/3$

Let us now consider densities slightly less than 1/3. We start from the *uud* state and picture it as a filled A sublattice. An appealing scenario is to introduce holes and let them move around on A and condense. We automatically retain charge order selecting the A sublattice vs. B and C. The condensation of holes on the A gives boson superfluid order there and by proximity effect also on the B and C sublattices. Since $t_{AB} = t_{AC} < 0$, we expect the phase angle on the BC to be shifted by π from the A. The resulting supersolid is precisely the V state.

Direct wave function implementation of this scenario is described in Appendix 3.A and leads to a sum of permanents, which becomes prohibitively costly to evaluate for more than a few holes. In the appendix, we also motivate a qualitatively similar wave function with a simpler amplitude given by a single permanent,

$$\langle \{r_k\} | \psi_{V_{\mathrm{perm}}} \rangle = \mathrm{Perm} \begin{pmatrix} \phi_1^{\mathrm{loc}}(r_1) & \dots & \phi_{N/3}^{\mathrm{loc}}(r_1) \\ \vdots & \ddots & \vdots \\ \phi_1^{\mathrm{loc}}(r_{N_b}) & \dots & \phi_{N/3}^{\mathrm{loc}}(r_{N_b}) \\ 1 & \dots & 1 \\ \vdots & \ddots & \vdots \\ 1 & \dots & 1 \end{pmatrix} . \tag{3.11}$$

The first N_b rows contain the localized orbitals of the *uud* construction evaluated at the boson positions, while the remaining $N/3 - N_b$ rows are filled with 1-s corresponding to "zero wavevector" condensate of holes (see Appendix 3.A for details).

Table 3.4 shows the V_{perm} energy for 11 bosons on the 6×6 cluster. Being a descendant of the excellent *uud* state, even with no Jastrow factor the V_{perm} performs very well and lies roughly half-way between the ground state and the first excited state with the same quantum numbers (the latter is not listed in the table). In particular, the V_{perm} clearly wins over the spiral superfluid with uniform density. Just as in the *uud* case, adding simple short-range Jastrow parameters further improves the trial energy of the V_{perm} state. At this stage, we did not include long-range Jastrow pseudopotentials, which would be needed for a correct long-wavelength description[77] of superfluid correlations in the V phase.

The V_{perm} state gives our best variational energies for $N_b = 6, \dots, 11$. In Appendix 3.B, we measure properties of this state and verify the superfluid order with opposite signs on the A and BC sublattices as anticipated above.

3.2.5 V state at $n \ll 1/3$

The above wave function for the V phase is obtained from the strong *uud* state and a priori is not expected to remain good at low density. Here we consider an alternative construction of the V supersolid using Bijl-Jastrow-type wave function, working directly with bosons and condensing them into an appropriate extended

Trial state	$N^{\rm orb}_{\rm par}$	$N^{\rm Jas}_{\rm short}$	$N^{\rm Jas}_{\rm long}$	$N^{\rm tot}_{\rm par}$	E/bond
classical					0.13542
spiral	0	1	2	4	0.12885
$V_{\rm BJ}$	1	0	0	1	0.13216
	1	1	0	2	0.12913
	1	1	2	4	0.12871
exact					0.12845

Table 3.5: Comparison of $V_{\rm Bijl-Jastrow}$ trial energies for different number of variational parameters for 2 bosons on a 36-site cluster. The extended orbital of the $V_{\rm Bijl-Jastrow}$ state has amplitude $e^{\mu/2}$ on sublattice A and -1 on sublattices B and C; μ is the only variational parameter in the first listed $V_{\rm Bijl-Jastrow}$ case. The second $V_{\rm Bijl-Jastrow}$ case has one nnb Jastrow pseudopotential which is taken to be the same between any pair of nnb sites, while the third case has two additional parameters for a long range pseudopotential which is the same as in the spiral case in Table 3.3. We also show trial energy for the spiral state with 4 variational parameters, which has slightly higher energy than the $V_{\rm Bijl-Jastrow}$ state.

orbital,

$$|\psi_{V,\rm Bijl-Jastrow}\rangle = \left(\sum_r \phi_V^{\rm ext}(r)\ b_r^\dagger\right)^{N_b} |0\rangle \tag{3.12}$$

$$\phi_V^{\rm ext}(r) = \begin{cases} e^{\mu/2},\ r \in A \\ -1,\ r \in B, C \end{cases} \tag{3.13}$$

This orbital has opposite signs on the A and BC sublattices as expected from Fig. 3.3d. The "chemical potential" μ on the A sublattice allows us to control the charge order. Similar to other wave functions for states with superfluid order, it is necessary to include a long-range Jastrow factor.

As we argue below, this wave function is a natural candidate at low boson densities. On the 6×6 cluster, it optimizes better than the $V_{\rm perm}$ state for $N_b \leq 6$ and also has better energy than the spiral state, see Fig. 3.4. As an example of variational results, Table 3.5 shows the $V_{\rm Bijl-Jastrow}$ energy for three bosons on the 6×6 cluster. We see that the V state is slightly better than the spiral state. However, both states are quite close in energy and close to the exact ground state. We discuss this more below and see what we can infer about the competition between the coplanar and spiral states from ED spectroscopy.

First, we want to connect the competing $V_{\rm Bijl-Jastrow}$ and spiral states with physics at low boson densities. In the absence of interaction, the kinetic energy minimizes at two distinct points in the Brillouin zone, $\pm\vec{Q} = \pm(4\pi/3,\ 0)$. Boson condensation at one point gives rise to the spiral phase; schematically, the spiral wave function is given by $(b^\dagger_{\vec{Q}})^{N_b}|0\rangle$ [or $(b^\dagger_{-\vec{Q}})^{N_b}|0\rangle$ for the opposite spiral]. A more complex condensation pattern including both points produces a coplanar state, with schematic wave function $(e^{i\alpha}b^\dagger_{\vec{Q}} + \text{H.c.})^{N_b}|0\rangle$. When $\alpha = 0$, this gives boson orbital $\phi(r) = \cos(\vec{Q}\cdot\vec{r})$ taking values $\{+1, -1/2, -1/2\}$ on the three sublattices, which is essentially the ϕ_V^{ext} orbital in Eq. (3.13). On the other hand, $\alpha = \pi/2$ corresponds to a different state with zero boson density on one sublattice and alternating superfluid phases on the remaining two sublattices; in terms of spins, this is a coplanar "Ψ"-type state which has similar symmetry to the Y state in Fig.3.2b, but with the vertical spin flipped up. (For either V or Ψ, there are two more degenerate states given by lattice translations or equivalently by adding $\pm 2\pi/3$ to α.) Reference [11] studies the dilute boson problem analytically for the isotropic lattice and predicts that four-boson interactions select coplanar states. It does not resolve between the V and Ψ states, which would require six-boson terms.

Returning to our example with three bosons, the ED ground state has momentum quantum number $\vec{k} = \vec{Q}$ (there is of course degenerate state with opposite momentum), while even and odd parity states with $\vec{k} = 0$ lie very close. This can be traced to four degenerate eigenstates of the kinetic energy,

$$\left\{(b^\dagger_{\vec{Q}})^3,\quad (b^\dagger_{-\vec{Q}})^3,\quad (b^\dagger_{\vec{Q}})^2 b^\dagger_{-\vec{Q}},\quad b^\dagger_{\vec{Q}}(b^\dagger_{-\vec{Q}})^2\right\}\ . \tag{3.14}$$

Our spiral wave function construction would give essentially the first two states with $\vec{k} = 0$. Our three degenerate V states, upon constructing translationally invariant combinations, would give an even-parity $\vec{k} = 0$ state as well as the last two states with $\vec{k} = \pm\vec{Q}$. Finally, the three degenerate Ψ-type states would give an odd-parity $\vec{k} = 0$ state and the same two $\vec{k} = \pm\vec{Q}$ states. It is clear that these trial states are not independent for this small number of bosons; we cannot resolve the phases, but we can start looking for some tendencies. For example, we can view the fact that the $\vec{k} = \pm\vec{Q}$ are lower in energy than $\vec{k} = 0$ as an indication for the coplanar states being better than the spiral. In principle, we could also try to resolve between the V and Ψ by comparing the even/odd-parity $\vec{k} = 0$ states, but the splitting is too tiny.

We have similarly examined ED spectra with $N_b = 4, \ldots, 9$ bosons, paying attention to near degeneracy of ground states and their quantum numbers. The resolution between the spiral and coplanar states due to interactions becomes clearer with increasing density, and in each instance the ED data is consistent with the coplanar

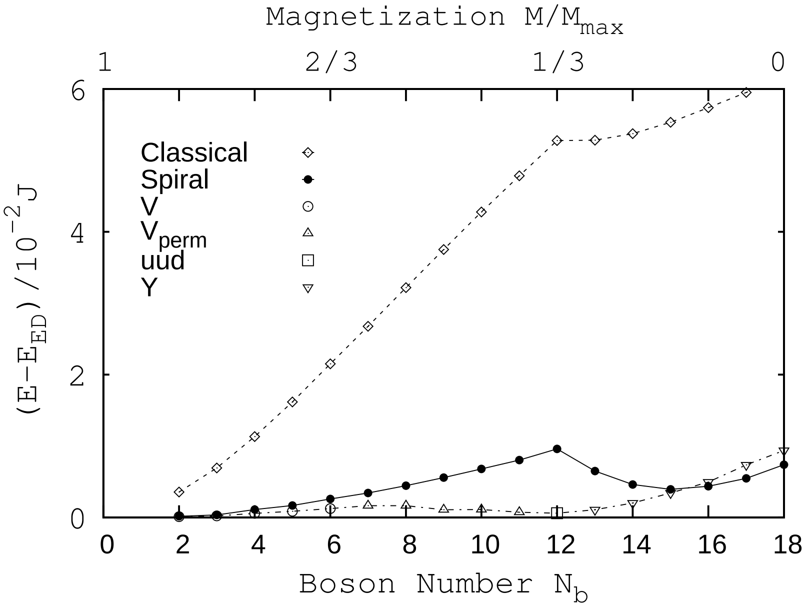

Figure 3.4: Comparison of variational energies (per bond) for the 36-site cluster with isotropic exchanges. The trial energies for the planar states are obtained using Bijl-Jastrow-type wave function for V ($N_b \leq 6$) and permanent-type wave functions for V ($7 \leq N_b \leq 11$), uud ($N_b = 12$), and Y ($N_b \geq 12$). The spiral trial energies are obtained using the Huse-Elser wave function. For clarity, ED ground state energies are subtracted at respective boson numbers. The classical energy curve provides a reference for judging stabilization of specific phases by quantum fluctuations.

states being better. As far as the resolution between the V and Ψ states is concerned, we cannot tell anything with boson number below 6, while for higher boson number we start seeing evidence in favor of the V state. The V state is expected coming from the $n = 1/3$ plateau as we discussed earlier. One possibility is that V occurs for all $n < 1/3$, but we cannot rule out transition to the other coplanar state at low densities. Our VMC study of the spatially anisotropic model on larger clusters in Sec. 3.3.4 also suggests that an incommensurate coplanar phase (in this case, there is no distinction between V and Ψ) wins over the spiral also for a range of anisotropies, strengthening the conclusions here on the coplanar versus spiral energetics.

3.2.6 Summary of trial energies on the isotropic lattice

Fig. 3.4 summarizes the spin energies (per bond) of competing trial states calculated for the 6×6 cluster with periodic boundary conditions for all N_b. For a better comparison of the accuracies of these trial wave functions, we subtract the ED ground state energy at each boson density. The energies of the classical state are included

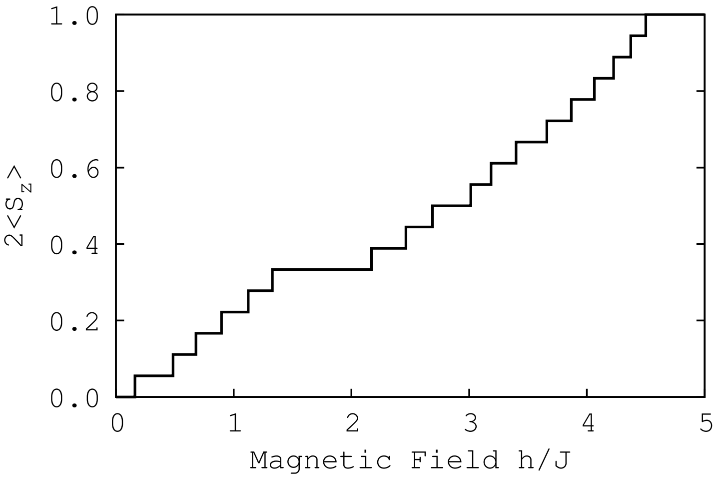

Figure 3.5: Magnetization curve of the 36-site cluster obtained using the variational energies. The pronounced *uud* plateau agrees well with the ED results in Ref. [69]. This shows that the variational tool is able to capture this Mott insulator as well as nearby supersolid phases.

to emphasize the stabilization of specific phases by quantum fluctuations. Our wave functions are particularly accurate in the vicinity of the plateau, and also at low boson densities (higher fields). In the latter regime, the classical energies approach ED values at low densities, indicating vanishing quantum fluctuations[7, 11, 12].

3.2.7 Magnetization process on the isotropic lattice

Using the trial energies from our studies at fixed N_b, we can work out the magnetization curve as a function of field h. Fig. 3.5 shows this for the 36-site cluster. The boundaries of the 1/3-magnetization plateau are determined by the energy gaps to adding or removing one boson to the *uud* state. Since our permanent constructions give very good trial Y and V states in this regime, the estimate of the plateau range is quite accurate. To check finite size effects, we repeated the calculation on a 63-site cluster and obtained critical fields $H_{c1} \approx 1.4J$ and $H_{c2} \approx 2.2J$.

3.2.8 2-parton trial wave functions and alternative construction of *uud* state at $n = 1/3$

The above direct study using spiral, Y, *uud*, and V states is sufficient to describe the phase diagram of the spatially isotropic triangular antiferromagnet in the field. We now consider a versatile set of trial wave functions which we will call "2-parton" states. One motivation is to give a practical realization of the Chern-Simons flux attachment treatment in Ref. [78]. (The relation between the parton and Chern-Simons approaches is discussed in Ref. [79] and citations therein.) Another motivation is to prepare for an anisotropic lattice study in Sec. 3.3. We should say from the outset that while such parton construction is typically used to produce fractionalized (spin liquid) states, it can also be used to give more conventional states such as CDW of bosons with no topological order as discussed below.

We represent the boson operator in terms of two fermions, $b = d^{(1)}d^{(2)}$, subject to constraint $b^\dagger b = d^{(1)\dagger}d^{(1)} = d^{(2)\dagger}d^{(2)}$ on each site. Imagine some "mean-field Hamiltonian" for each parton flavor,

$$\hat{H}_{\rm mf}^{(n)} = -\sum_{\langle rr'\rangle}\left(|t_{rr'}^{(n)}|e^{ia_{rr'}^{(n)}}d_r^{(n)\dagger}d_{r'}^{(n)} + \text{H.c.}\right) - \sum_r \mu_r^{(n)} d_r^{(n)\dagger}d_r^{(n)} \ . \tag{3.15}$$

Here we write the parton hopping amplitudes (which can be complex) as $t_{rr'}^{(n)} = |t_{rr'}^{(n)}|e^{ia_{rr'}^{(n)}}$; we also allow site-dependent chemical potentials $\mu_r^{(n)}$ to test CDW tendencies. The $t_{rr'}^{(n)}$ and $\mu_r^{(n)}$ are variational parameters. We solve $\hat{H}_{\rm mf}^{(n)}$ and fill up the corresponding Fermi seas with $N_{d_1} = N_{d_2} = N_b$ particles. A valid bosonic wave function is obtained by applying a Gutzwiller projection such that every site is either empty ($n_b = n_{d_1} = n_{d_2} = 0$) or contains both d_1 and d_2 partons ($n_b = n_{d_1} = n_{d_2} = 1$):

$$|\psi_{2p}\rangle = \hat{P}_G \prod_{q_n \in FS_n} d_{q_1}^{(1)\dagger} d_{q_2}^{(2)\dagger}|0\rangle. \tag{3.16}$$

For each boson configuration, the amplitude is given by a product of two Slater determinants. One feature of this construction follows from the fermionic statistics which provides an inherent repulsive Jastrow effect for the particles. This effect can be tuned as follows,

$$\langle\{r_k\}\,|\psi_{2p}\rangle = \det{}_1 \cdot \det{}_2 \cdot |\det{}_1|^{p_1 - 1} \cdot |\det{}_2|^{p_2 - 1} \ , \tag{3.17}$$

which preserves the "sign structure" of the wave function while allowing more variational freedom with parameters p_1 and p_2. Numerical calculations can be performed using efficient determinantal Monte Carlo techniques[80].

Besides treating boson repulsion, we want to have good kinetic energy. We can write the frustrated boson hopping amplitudes in Eq. (3.3) as $t_{rr'}^{(b)} = |t_{rr'}^{(b)}|e^{ia_{rr'}^{(b)}}$ and view this as a problem in an external orbital field producing flux π through each triangle[81]. To capture this in the parton treatment, we view $d^{(1)}$ and $d^{(2)}$ as charged particles whose charges add up to that of the boson b; we therefore require

$$e^{ia^{(1)}_{rr'}} e^{ia^{(2)}_{rr'}} = e^{ia^{(b)}_{rr'}}. \tag{3.18}$$

Thus the parton mean-field Hamiltonian should contain fluxes such that for the two flavors they add up to the original flux seen by the bosons. We can still make different choices, say, for the d_1; however, once the $a^{(1)}_{rr'}$ are fixed, then the $a^{(2)}_{rr'}$ are uniquely determined.

We first discuss what we will call "Chern-Simons" states that realize the idea in Ref. [78]. For the d_1 hopping, we take uniform flux of $n\pi$ per triangle, where n is the boson density per site. With this choice, the $\det_1$ Slater determinant fills the "lowest Landau level" band and gives a finite lattice version of the usual Chern-Simons factor $\prod_{i<j}(z_i - z_j)$. We can loosely view the $\det_1$ as performing flux attachment transformation from the bosons to the d_2 fermions[79]. Upon subsequent "flux smearing" mean-field, the d_2 see flux $(1-n)\pi$ per triangle. In the absence of site-dependent chemical potentials and for some rational densities, the $\det_2$ Slater determinant is gapped, and the boson wave function realizes a fractionalized "chiral spin liquid"[78, 81, 82]. We have tried these "topological" states for several densities such as $n = 1/3, 1/4, 1/6$ on the isotropic triangular lattice and found that they are poor compared with the uud and V states described earlier. Thus the interesting proposal of plateaus due to chiral spin liquid states is not realized on this lattice[78].

We now specialize to density $n = 1/3$ and allow a chemical potential on the A sublattice: $\mu_A \neq 0, \mu_B = \mu_C = 0$. We find that optimal $\mu^{(1)}_A, \mu^{(2)}_A$ are large and produce strong CDW order in the mean-field state. When this happens, the trial boson state [Eq. (3.17)] is no longer topological in nature. Indeed, if the parton hopping is set to zero, this construction simply gives the classical $\sqrt{3} \times \sqrt{3}$ CDW state. The particles completely occupy sublattice A, and there is a large gap at the parton Fermi level. Adding small hopping does not close this gap but only builds in some charge fluctuations into the parton mean-field and thus into the boson trial state. Working perturbatively in $t^{(n)}/\mu^{(n)}_A$, the leading modification to the classical boson CDW wave function is to add configurations where one particle moves from a site A_j to a neighbor r. The amplitude for such a configuration is proportional to $t^{(1)}_{A_j,r} t^{(2)}_{A_j,r} / (\mu^{(1)}_A \mu^{(2)}_A) \sim t^{(b)}_{A_j,r}/\mu^{(b)}_A$, where we have kept track of all signs and introduced schematically boson charge gap $\mu^{(b)}_A$. The result is similar to the perturbative picture of the CDW working directly in the boson language that motivated the wave function

Eq. (3.5). Thus at this level the 2-parton states with strong CDW potential are qualitatively the same as the permanent *uud* state in Sec. 3.2.1.

The above leading order structure holds for all 2-parton states satisfying Eq. (3.18). At higher order, the states will differ, and amplitudes can be complex in general: e.g., the Chern-Simons wave function described above is complex-valued. On the other hand, the permanent *uud* wave function is real. The boson Hamiltonian Eq. (3.2) is invariant under complex conjugation in the number basis, and the *uud* state preserves this symmetry. We can construct a real-valued 2-parton state by taking the d_1 fluxes to be 0 or π through up or down triangles; the d_2 partons see correspondingly π and 0 fluxes. We will call this state "$U1B$." It was originally discussed at half-filling in Ref. [83], where (in the absence of chemical potentials) it has Dirac nodes at the Fermi level and realizes so-called Algebraic Spin Liquid state. This particular state has a good trial energy in the Heisenberg model[15, 79, 62], and can be viewed as a more elaborate real-valued version of the Laughlin-Kalmeyer state (see Sec. IIC of Ref. [79] for more discussion). Away from half-filling, the $U1B$ mean-field state has Fermi surfaces of partons and may be unstable to a mechanism described in Ref. [84]. However, this is not a direct concern here since we are gapping out the state by adding large μ_A potential and are connecting to the strong CDW of bosons. The virtue of using the 2-parton framework is that it naturally builds in small charge fluctuations as described above, and determinants are easier to compute as opposed to permanents. Using this construction for the isotropic 6×6 lattice at $n = 1/3$, we obtain a very competitive energy -0.1341 (cf. trial energies in Table 3.1) with $\mu_A \approx 2$ and $p \approx 0.75$. (We also obtain close trial energy using the Chern-Simons state with strong CDW potential, in agreement with the earlier discussion that all 2-parton states can similarly capture leading local charge fluctuations when the charge order is strong). The 2-parton constructions are particularly useful on the anisotropic lattice to be discussed in Sec. 3.3, since they naturally connect to the decoupled chains limit and allow us to detect where the quasi-1D physics sets in and explore CDW instabilities.

3.3 Anisotropic triangular antiferromagnet

Motivated by the unknown phases of Cs_2CuBr_4 in the field[9], we extend our study to the spatially anisotropic lattice. We describe anisotropic extensions of the wave functions introduced in Sec. 3.2 and then present our variational results.

3.3.1 Anisotropic Versions of Wave Functions

Although our study began with a goal of constructing accurate wave functions for identifying the unknown phases of Cs_2CuBr_4, it quickly became clear that this is far from easy. The number of theoretically possible phases is already very rich, with different physics regimes requiring different mindsets. Nevertheless, the variational approach is a useful tool for obtaining quantitative insights into the energetics of various phases, since it applies directly to the spin-1/2 problem at hand and goes beyond approximate treatments like large-S and mean-field. Encouraged by our success for the isotropic problem in the field, we apply this tool to the anisotropic case, while being critical of the limitations of the variational approach.

We consider the anisotropic triangular lattice antiferromagnet with $J'/J \leq 1$, where J and J' are the coupling constants of horizontal and oblique nearest-neighbor links (see Fig. 3.1). The spatially anisotropic wave functions used in this section contain appropriate modifications to the wave functions in Sec. 3.2.

Permanent constructions: For the wave functions from Secs. 3.2.1, 3.2.2, and 3.2.4, the localized orbitals used in the uud, Y, and V_{perm} now include an additional parameter α':

$$\phi_j^{\text{loc}}(r) \quad = \quad \begin{cases} 1, & r = A_j \\ -\alpha, & r = \text{horizontal n.n. of } A_j; \\ -\alpha', & r = \text{oblique n.n. of } A_j; \\ 0, & \text{otherwise.} \end{cases} \tag{3.19}$$

Spiral: Our treatment of the spiral requires separate discussion. The 120° spiral generalizes to an incommensurate spiral with wavevector $\vec{Q}$[12, 10]. However, in a finite sample, periodic boundary conditions would bias against the incommensurate order. We can mitigate this effect by considering appropriate phase twists at the boundaries that accommodate such $\vec{Q}$. For computations, it is convenient to perform a gauge transformation that spreads the twist uniformly across the sample; the resulting Hamiltonian is then translationally invariant:

$$\hat{H}_{\text{twisted}} = -\sum_{\langle rr' \rangle} \left(t_{rr'} e^{i\vec{Q}\cdot\vec{e}_{rr'}} b_r^\dagger b_{r'} + \text{H.c.} \right) + H_{\text{int}} \ , \tag{3.20}$$

where $\vec{e}_{rr'}$ is the displacement vector from r to r'. The twisted Hamiltonian is used only for calculating the incommensurate spiral energies while all other trial energies are evaluated using the original Hamiltonian with no twist.

Jastrow factors: To accommodate spatial anisotropy, we introduce additional parameters into the nearest-neighbor and long-range pseudopotentials as follows:

$$u(r,r') = \begin{cases} w, & \text{if } r \text{ and } r' \text{ are horizontal n.n.} \\ w', & \text{if } r \text{ and } r' \text{ are oblique n.n.} \\ \frac{A}{[\alpha^2(x-x')^2+(y-y')^2]^{p/2}}, & \text{otherwise.} \end{cases} \tag{3.21}$$

2-parton: To obtain spatially anisotropic versions of the 2-parton wave functions from Sec. 3.2.8, we allow the mean-field hopping amplitudes in Eq. (3.15) to be anisotropic:

$$t^{(n)}_{rr'} = \begin{cases} t^{(n)}, & \text{if } r \text{ and } r' \text{ are horizontal n.n.} \\ t'^{(n)}, & \text{if } r \text{ and } r' \text{ are oblique n.n.} \end{cases} \tag{3.22}$$

We consider the same fluxes and possible site-dependent potentials as in Sec. 3.2.8. For example, at density $n = 1/3$ we allow $\sqrt{3} \times \sqrt{3}$ pattern in the chemical potential. At other densities, we can consider other appropriate CDW patterns.

One virtue of the 2-parton states is that they connect naturally to the decoupled chains limit. Indeed, for $t'^{(n)} = 0$, $\text{sign}[t^{(1)}t^{(2)}] = \text{sign}[t^{(b)}] < 0$, the trial wave function Eq. (3.17) on each chain reduces to

$$\Psi_{\text{chain}}(x_1, \ldots, x_M) \quad \sim \quad e^{i\pi(x_1+\cdots+x_M)} \times \left| \prod_{i<j} \sin \frac{\pi(x_i - x_j)}{L} \right|^p \tag{3.23}$$

with $p = p_1 + p_2$. The first factor gives the correct Marshall sign for the 1D boson problem with hopping $t^{(b)} < 0$. (To be more precise, we assume that the chain length L is even and choose periodic or antiperiodic boundary conditions for the partons depending on whether the number of bosons M is odd or even.) This is an accurate trial state in the full range of boson densities: For $n = 1/2$, with $p = 2$ it reduces to the ground state of the Haldane-Shastry chain and is a good approximation to the ground state of the Heisenberg chain; for $n \to 0$, with $p = 1$ it reproduces the nearly free fermion picture of the dilute gas of hard-core bosons; for varying n, by adjusting p this state can capture varying Luttinger liquid exponents. The 2-parton construction can thus provide a starting point for exploring what happens when the chains are coupled together. As discussed in Sec. 3.2.8, the parton hopping between

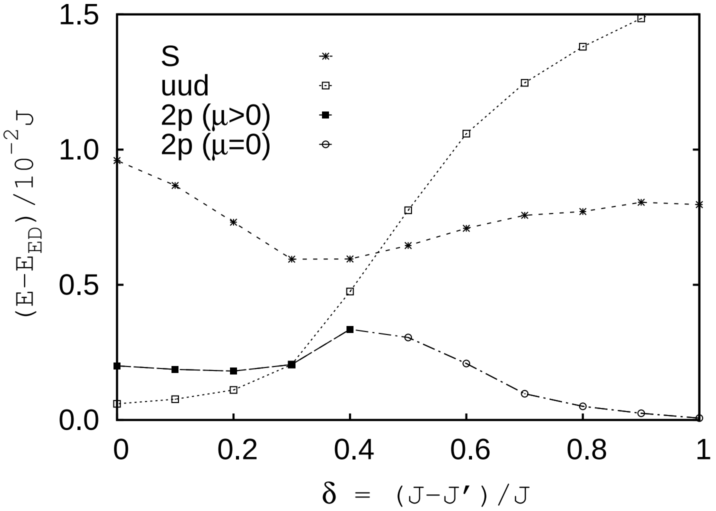

Figure 3.6: Comparison of spiral, permanent-type *uud*, and 2-parton trial energies (per bond) for 12 bosons on the anisotropic 36-site cluster. The wave functions are anisotropic generalizations of those constructed in Sec. 3.2. For $\delta \lesssim 0.4$, the optimal 2-parton wave function has a non-zero chemical potential on sublattice A and provides an alternative realization of the *uud* state. For $\delta > 0.4$, the chemical potential optimizes to zero, probably due to large finite-size gap for such anisotropy. On a larger 24×24 cluster, the chemical potential remains non-zero up to $\delta \approx 0.7$, leading us to conjecture that in the thermodynamic limit the *uud* phase persists all the way to $J'/J \to 0$.

the chains with vector potentials satisfying Eq. (3.18) can roughly capture the interchain boson hopping energy, while site-dependent chemical potentials can produce candidate CDW states. We will present this in some detail for $n = 1/3$ and $n = 1/6$.

ED calculations: To conclude the discussion of our anisotropic setups, we describe the supplementary ED calculations on the 36-site cluster with J and J' couplings. We compute a few lowest eigenvalues in each symmetry sector of the Hamiltonian with no twist and also eigenvalues in the zero momentum sector of the twisted Hamiltonian [Eq. (3.20)] with varying $\vec{Q}$. At a given anisotropy and boson density, the minimum of these ED energies is taken to be the ground state energy. Our ED calculations are restricted to $N_b \leq 12$. The variational calculations are performed for the same 36-site cluster and also for larger systems.

We now turn to the results of our anisotropic study. For illustration, we present two boson densities.

3.3.2 $n = 1/3$

Figure 3.6 shows the trial energies of *uud*, incommensurate spiral, and 2-parton wave functions at density 1/3 on the 36-site cluster. From the isotropic study, it is not surprising that the permanent-type *uud* wave function remains a good candidate at low anisotropy. As mentioned in Sec. 3.2.8, the 2-parton U1B wave function constructed with $0/\pi$ fluxes through triangles and a localizing chemical potential on one sublattice provides an alternative realization of the *uud* state. For $\delta \gtrsim 0.3$, the 2-parton energy becomes lower than the permanent-type wave function but the $\sqrt{3}\times\sqrt{3}$ chemical potential (and therefore the *uud* phase) persists up to $\delta \approx 0.4$. Since our permanent wave function uses localized orbitals that only extend to nearest-neighbor sites, it fails to capture longer-range correlations in the chain direction expected in a more anisotropic system. We would need to use more extended orbitals in the permanent, but we have not pursued this. On the other hand, the 2-parton realization readily accommodates the lattice anisotropy via the parton hoppings, Eq. (3.22), and provides a simple way to continue our study of the *uud* state to larger anisotropy.

In the highly anisotropic region, we obtain good trial energies for the 6×6 system using the 2-parton wave function without the chemical potential. However, if we consider the low energy cutoff due to the finite cluster size, it is clear that the study cannot resolve the true phase in the thermodynamic limit. Specifically, in the decoupled chains limit, we obtain a very accurate wave function for two bosons on a 6-site chain by using antiperiodic boundary conditions for the partons, cf. Eq. (3.23). The corresponding parton spectrum nicely accommodates two particles and has a large finite-size gap to next levels, which persists up to moderate inter-chain couplings. While our 2-parton state by virtue of good fluxes naturally builds in good inter-chain exchange correlations, we cannot resolve the thermodynamic phase (e.g., the development of the $\sqrt{3} \times \sqrt{3}$ CDW) if the relevant energy scale is much lower than the finite-size gap.

To determine how far the *uud* phase might extend into the anisotropic region, we repeat the 2-parton calculation on a large 24×24 cluster and find that the $\sqrt{3} \times \sqrt{3}$ chemical potential surprisingly remains non-zero up to $\delta \approx 0.7$. We also check that the parton spectrum for the optimal parameters is fully gapped and is connected to the strongly gapped CDW limit, so the trial wave function is indeed a valid charge-ordered Mott insulator of bosons as discussed in Sec. 3.2.8. We thus conclude that the *uud* state persists to rather strong anisotropy, albeit the CDW order becomes progressively weaker. Interestingly, Ref. [13] would predict the same $\sqrt{3} \times \sqrt{3}$ CDW

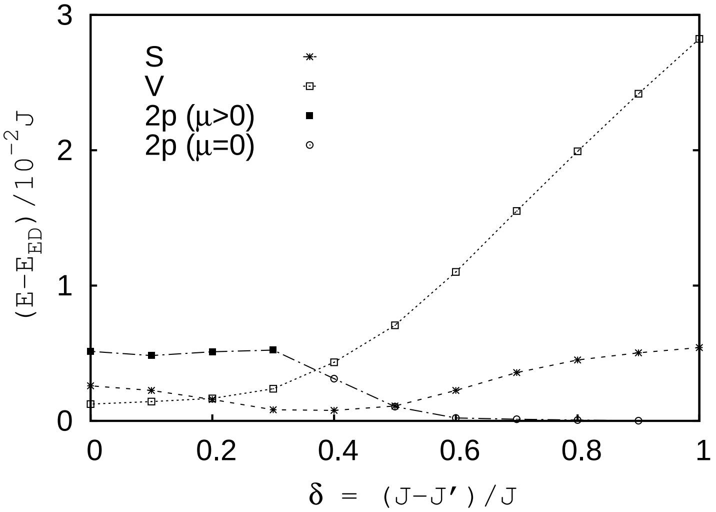

Figure 3.7: Comparison of spiral, commensurate $V_{\mathrm{Bijl-Jastrow}}$, and 2-parton trial energies as a function of anisotropy for 6 bosons on the 6×6 cluster. The E_{2p} values are obtained with higher chemical potential on one sublattice for $\delta \leq 0.3$ (in agreement with this state trying to capture 3-sublattice features near small anisotropy in this small sample). We also performed a much larger study at $n = 1/6$ comparing commensurate and incommensurate V states, incommensurate spiral, and 2-parton states; from this study, the region of commensurate V is actually quite small, while the incommensurate V dominates over the spiral over a range $\delta \leq 0.3$ (see text for more details).

order in the nearly decoupled chains limit at density $n = 1/3$. Combining with our variational work, this suggests that the *uud* phase may in fact extend continuously from $\delta = 0$ up to $\delta = 1$ (See Fig. 3.10). A rigorous confrontation to this conjecture could be provided, for example, by a systematic DMRG study of $3 \times L$ ladders at density $n = 1/3$ varying J'/J from 1 to 0 and monitoring the evolution of the $\sqrt{3} \times \sqrt{3}$ charge order.

While our study agrees with the observed plateau in Cs_2CuBr_4 ($\delta \approx 0.3$), it contradicts the absence of the plateau in Cs_2CuCl_4 ($\delta \approx 0.66$). It is likely that residual interactions (e.g. such as Dzyaloshinskii-Moriya) have to be added to the Heisenberg model in order to describe the latter material[13], and they can change the energetics balance against the (very weak) *uud* state in this highly anisotropic system.

3.3.3 $n = 1/6$

Figure 3.7 shows the trial energies of commensurate $V_{\text{Bijl-Jastrow}}$, incommensurate spiral [treated as described around Eq. (3.20)], and 2-parton wave functions for 6 bosons on the 6×6 cluster. At low anisotropy, the $V_{\text{Bijl-Jastrow}}$ state is a good candidate. For increasing anisotropy, a change to the incommensurate spiral is observed, which eventually loses to the "quasi-1D" phase represented by the 2-parton wave function with zero chemical potential.

In the highly anisotropic region, the figure shows remarkable agreement between the ED and the 2-parton energies, where we impose uniform $\pi/6$ and $5\pi/6$ flux per triangle for the d_1 and d_2 partons, respectively (Chern-Simons state described in Sec. 3.2.8). Despite the excellent agreement, we simply conclude that the highly anisotropic region is strongly dominated by quasi-1D physics and finite size effects. Specifically, in the ED calculation on the 36-site cluster with 6 bosons, we find a non-degenerate ground state and a relatively large excitation energy gap. We interpret this as follows. In the decoupled chains limit, each chain contains one boson; for such a segment of length $L = 6$, one expects a non-degenerate ground state with a large excitation gap due to finite size. This gap persists as the chains are coupled, particularly because of some frustration present in the triangular lattice geometry.

We can similarly rationalize all our ED observations at other densities in the highly anisotropic limit. For example, for 7 bosons on the 36-site cluster, one of the chains now contains two bosons, and the ground state of the decoupled chains Hamiltonian is 6-fold degenerate due to 6 possible ways of choosing this chain. The finite-size gaps "protect" this situation until the inter-chain coupling J' becomes sufficiently large. Such observations on the ED spectra show serious limitations of the small system study in the anisotropic model. Going over all ED data for $N_b \leq 12$, we conclude that $\delta \gtrsim 0.5$ regime can be rationalized as such weakly coupled finite chains, with no clear resolution of the ultimate state. This is labeled as "quasi-1D" region in Fig. 3.9.

One of the goals of the 6×6 study was to have ED reference for our trial states. Having achieved some confidence in the good energetics of these states (despite their limitations), we now want to discuss variational results for larger sizes. Specifically, on the 36-site cluster, we have not considered the possibility of incommensurate V state: While we know how to accommodate the incommensurate spiral state, we do not have similar construction for the incommensurate coplanar state. On the 36-site cluster, we see that incommensuration becomes important for $\delta \geq 0.2$. In fact, as we discuss below, we think that for this density the V state is probably incommensurate already for smaller anisotropy, but also extends to larger anisotropy in the competition against the spiral.

3.3.4 Incommensurate V versus spiral study at low to intermediate boson densities

In this section, we focus on the high field regime where the incommensurate V and spiral are the main competing candidates. First, we briefly describe the relevant physical picture. Beginning with the near-saturation limit, we consider a gas of free bosons hopping on the triangular lattice with the following kinetic energy spectrum:

$$\epsilon_k = J\cos(k_x) + 2J'\cos\left(\frac{k_x}{2}\right)\cos\left(\frac{\sqrt{3}\,k_y}{2}\right). \tag{3.24}$$

The band minima occur at $\vec{Q} = \pm(Q_x, 0)$ with

$$Q_x = 2\ \mathrm{acos}(-J'/2J). \tag{3.25}$$

A condensation of bosons at these points gives rise to a degenerate manifold of states spanned by

$$\{(b^\dagger_{\vec{Q}})^m (b^\dagger_{-\vec{Q}})^{N_b-m}|0\rangle\ ;\ m = 0, 1, \ldots, N_b\}. \tag{3.26}$$

At low densities, the degeneracy is lifted by nearest-neighbor repulsion. To see how this happens, we expand the interaction in terms of the two dominant spectral modes and then replace the operators by c-numbers[11, 12]:

$$\begin{aligned}
b_r &\sim e^{i\vec{Q}\cdot\vec{r}}\ b_{\vec{Q}} + e^{-i\vec{Q}\cdot\vec{r}}\ b_{-\vec{Q}}, & (3.27)\\
\hat{H}_{\mathrm{int}} &= \sum_{\langle rr'\rangle} J_{rr'}\ b^\dagger_r b_r\ b^\dagger_{r'} b_{r'} & (3.28)\\
&\sim (J + 2J')\left(|b_{\vec{Q}}|^2 + |b_{-\vec{Q}}|^2\right)^2 +\ 2\upsilon\ |b_{\vec{Q}}|^2\ |b_{-\vec{Q}}|^2, & (3.29)\\
\upsilon &= J\cos(2Q_x) + 2J'\cos(Q_x). & (3.30)
\end{aligned}$$

The effect of nearest-neighbor repulsion is determined by the sign of υ. For $J'/J < 0.39$, υ is positive and the incommensurate spiral (e.g., $|b_{\vec{Q}}| \neq 0$ and $|b_{-\vec{Q}}| = 0$) wins. For $0.39 < J'/J \leq 1.59$, υ is negative and the incommensurate V ordering ($|b_{\vec{Q}}| = |b_{-\vec{Q}}|$) becomes more stable. The prediction from this approximate treatment

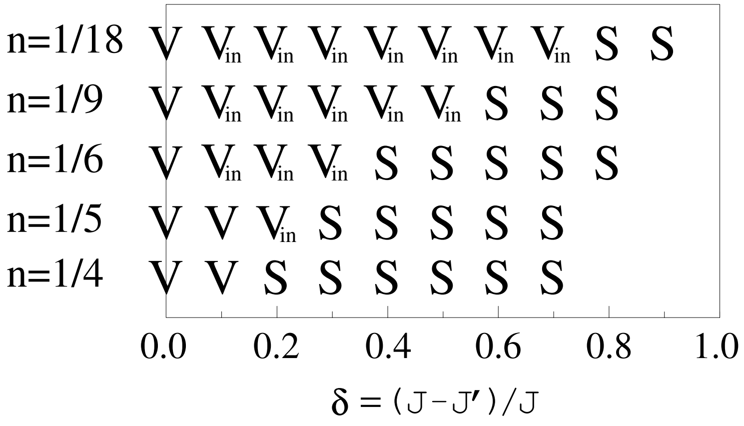

Figure 3.8: Variational phase boundary between V and spiral phases obtained from calculations on cluster sizes 18×18, 51×20, 27×20, 44×20, 47×20, 38×10, 39×10, 53×10, 60×10, and 99×10, where the corresponding anisotropy increases from 0 to 0.9 in equal intervals; the sizes are chosen so as to best accommodate the classical wavevector, Eq. (3.25). The V phase remains commensurate at $\delta = 0.1$ for $n \geq 1/5$. Note that at high anisotropy and particularly with increasing density, we find that the spiral loses to the 2-parton wave function, which we interpret as a quasi-1D dominated regime.

is consistent with the spiral phase found in the nearly decoupled chains limit near saturation and in the highly anisotropic dilute boson study for the Cs_2CuCl_4;[13, 12] this is also consistent with the coplanar phase found in the isotropic dilute boson study[11].

In the above discussion, we have neglected the effect of hard-core interaction. Intuitively, this should be more important at higher density: The role of the hard-core constraint is to prevent two bosons already in nearest-neighbor contact from further occupying the same site, while at low density such contacts are avoided due to nearest-neighbor repulsion. To see whether the hard-core interaction favors the V or spiral phase, we expand the on-site repulsion energy in terms of the two spectral modes:

$$(b_r^\dagger b_r)^2 \sim \left(|b_{\vec{Q}}|^2 + |b_{-\vec{Q}}|^2\right)^2 + \ 2\ |b_{\vec{Q}}|^2\ |b_{-\vec{Q}}|^2. \tag{3.31}$$

From the positive sign in the second term, which dislikes the V, we may expect the boundary between the V and spiral phases to shift in favor of the spiral phase as the density increases.

To address the competition between these two phases quantitatively at finite density, we implement a variational study on $m \times n$ rectangular clusters such that a fitting wavevector $Q_x = 2\pi p/m$ is close to the spiral wavevector at each anisotropy (with appropriate integers p). For the spiral phase, we use the same anisotropic wave function described earlier. A candidate wave function for the incommensurate V phase is constructed as follows:

$$\begin{aligned} |\psi_{V_{\rm in}}\rangle &= \left(e^{i\alpha} b^\dagger_{\vec{Q}} + e^{-i\alpha} b^\dagger_{-\vec{Q}}\right)^{N_b} |0\rangle \\ &= \left(\sum_r \cos(\vec{Q}\cdot\vec{r} + \alpha)\ b^\dagger_r\right)^{N_b} |0\rangle. \end{aligned} \tag{3.32}$$

Note that for incommensurate $\vec{Q}$ the relative phase between $b^\dagger_{\vec{Q}}$ and $b^\dagger_{-\vec{Q}}$ is not fixed, which we indicated with α. This is not important in an infinite system since $\vec{Q}\cdot\vec{r}$ visits all phases. On the other hand, for commensurate $\vec{Q} = (4\pi/3, 0)$, $\alpha = 0$ and $\pi/2$ correspond to distinct V and Ψ-type phases discussed in the isotropic case; both can be viewed as "parent" states for the incommensurate coplanar phase, but we will continue referring to the latter as V-type.

For ease of implementation, we use the same translationally invariant pseudopotentials given in Eq. (3.21). The V state has an incommensurate density wave and in principle allows more complicated pseudopotentials, so this choice probably biases slightly in favor of the spiral which has uniform boson density. In all other respects, the physical setting and the variational freedom are very similar in our realizations of the spiral and V states, and we think this study provides a fair comparison between the two phases even if the Q_x may be slightly off and the Jastrow pseudopotentials are not the most general.

Fig. 3.8 shows the result of our incommensurate V versus spiral variational study. The boundary between the two phases qualitatively agrees with our earlier argument, suggesting that the hard-core repulsion is comparatively less important at low density. We note that the obtained trial energies of the V and spiral states are quite close (particularly at low density), hence the exact location of the phase boundary should not be taken as definitive. Furthermore, the simple pseudopotential is clearly not optimal in the highly anisotropic regime, and eventually our spiral loses to the 2-parton states. A more rigorous V versus spiral variational study can be pursued by introducing more variational parameters into the Jastrow factor and employing systematic wave function optimization methods[15].

From the present results, we make an interesting observation that at the anisotropy relevant for Cs_2CuBr_4, $\delta \approx 0.3$, the transition occurs at density somewhere between

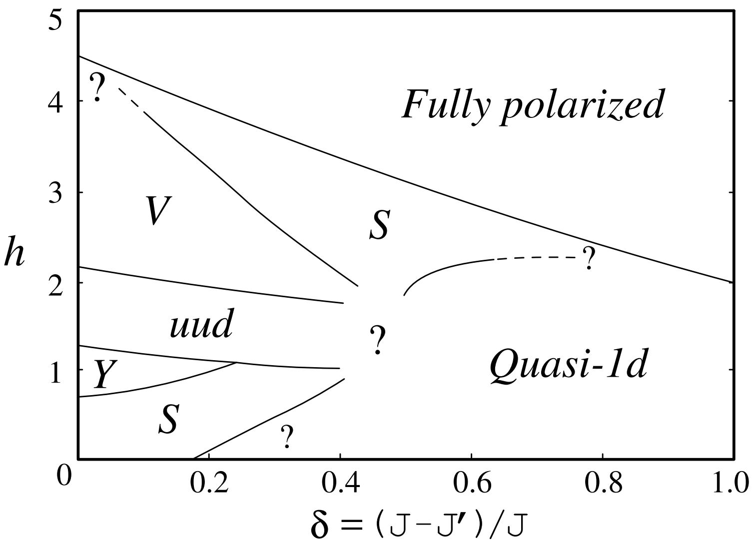

Figure 3.9: Variational phase diagram for the anisotropic 6 × 6 cluster in magnetic field. In this study, we exclude incommensurate versions of V and Y states. Due to finite size limitation, certain regions are marked as unresolved. In addition, the region $\delta > 0.5$ is strongly dominated by quasi-1D physics, particularly for this small cluster study (see discussions in text).

$n = 1/5$ (magnetization 0.6 of saturation) and $n = 1/6$ (magnetization 2/3 of saturation). The V phase occupies the region near saturation, while the spiral occurs at lower magnetizations. Thus, if the Heisenberg model is an adequate description, some of the features in the high field phase diagram of Cs_2CuBr_4 may be due to the competing umbrella-type and coplanar states[9].

3.3.5 Summary of Anisotropic Study

Figure 3.9 summarizes a variational phase diagram obtained for the 36-site cluster considering all boson densities. We label certain parts of the diagram with question marks or broken lines to indicate these regions as unresolved or less reliable. The figure shows the *uud* phase extending relatively far into the anisotropic region. On both sides of the *uud* phase, the commensurate coplanar phases remain stable over the incommensurate spiral for certain ranges of the anisotropy. As the spatial anisotropy biases against the commensurate states, the actual V and Y regions are expected to be wider if the wave functions are generalized to incommensurate versions. However, we exclude such extensions since they could not be accommodated on the 6×6 cluster. For $\delta > 0.5$, our 2-parton trial energies are generally very good. However, we think

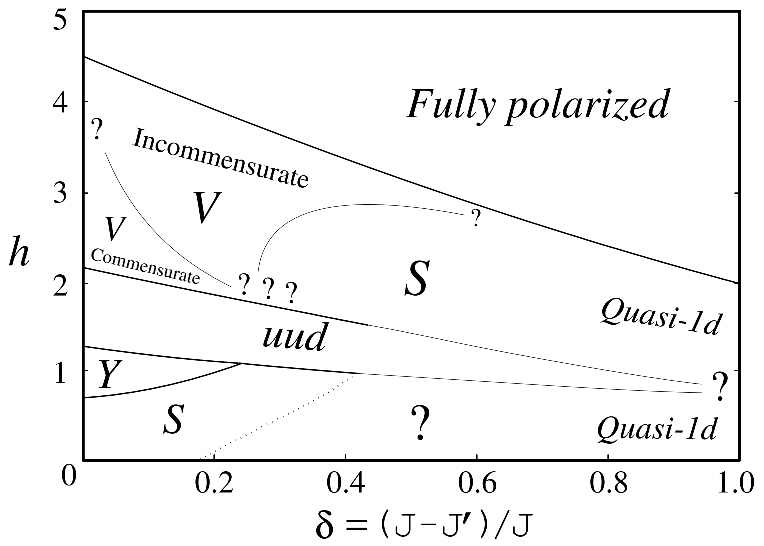

Figure 3.10: Schematic phase diagram for the anisotropic triangular lattice in magnetic field, combining 6 × 6 study as well as larger cluster studies. We suggest the possibility that the *uud* plateau extends across the entire range of anisotropy. The V phase is commensurate (see Fig. 3.2) near the isotropic axis and the plateau but becomes incommensurate at moderate anisotropy and higher fields. The highly anisotropic region is not well resolved in our variational study. The low field regime is particularly challenging and not studied thoroughly in this work.

that this only indicates the onset of quasi-1D physics and strong finite-size effects as discussed earlier for the specific densities.

Figure 3.10 shows a schematic phase diagram based on the 6×6 anisotropic study as well as studies on larger clusters. Here, we address a number of unresolved regions in Fig. 3.9: limits of the *uud* plateau, the boundary between V and spiral, and the boundary between commensurate and incommensurate V. We find that the *uud* phase extends much futher and may be even to all δ. Also, a significant portion of the phase diagram at high fields is occupied by the incommensurate V phase.

We note that our work does not rule out other incommensurate phases found in the recent study by Alicea *et al.*[10]. For example, we were not able to come up with a good implementation of the incommensurate extension of the Y state. On the other hand, we did try Bijl-Jastrow-type wave functions for distorted umbrella states discussed in Ref. [10], which are commensurate supersolids with incommensurate spiral phase angles. On the 36-site cluster, these trial states optimized to the incommensurate spiral with uniform boson density, but we have not explored this thoroughly on larger clusters. Overall, our results are more conclusive at low densities and much less at high densities between 1/3 and 1/2.

3.4 Summary and discussion

We studied the Heisenberg antiferromagnet on the spatially anisotropic triangular lattice in the field from a variational perspective. On the isotropic lattice, we constructed a very simple and physically transparent permanent-type wave function for the *uud* state at density 1/3. This is a Mott insulator of bosons where we accurately included small charge fluctuations by using appropriate localized boson orbitals. The remarkable trial energy suggests that such approach may be useful in other Mott insulator contexts. Next, we obtained natural extensions to nearby V and Y supersolid phases respectively for $n \lesssim 1/3$ and $n \gtrsim 1/3$, where the physics remains strongly influence by the proximity to $n = 1/3$. By connecting to a Bijl-Jastrow-type candidate wave function at low density, the coplanar V phase extends to all $n < 1/3$ (i.e., up to the saturation field in the spin model language). Note, however, that at very low density another coplanar state (Ψ-type) is expected to be very close[11], and we cannot resolve between the two. On the higher density side of the plateau (i.e., at lower fields), the permanent-type Y wave function performs well near the plateau but narrowly loses to the Huse-Elser spiral candidate at densities close to half-filling (zero field). The latter result is consistent with other recent works[75, 74, 62].

The success of our isotropic study encouraged us to extend it to the anisotropic lattice. At density $n = 1/3$, we begin with the permanent-type realization of the *uud* and then connect to a conceptually similar but technically different 2-parton realization at higher anisotropy. Surprisingly, we found that the *uud* phase remains stable over a large range of anisotropy. In conjunction with the same CDW phase found in the decoupled chains limit[13], we suggest that the *uud* phase may in fact extend across the entire range of anisotropy. This conjecture can be tested more rigorously using a DMRG study on finite-width strips.

In the low boson density region (i.e., at high fields), the Bijl-Jastrow-type V commensurate supersolid wave function is smoothly connected to the incommensurate version. This state competes with the incommensurate spiral, and we can accurately compare the two. We found that the incommensurate V state has lower energy in a large region of the phase diagram, extending up to a fairly large value of anisotropy in the very dilute regime (i.e., close to the saturation fields). On the other hand, the V phase remains commensurate near the isotropic axis and the plateau.

In the high density regime (i.e., at low fields), we attempted to construct an incommensurate Y candidate using a Bijl-Jastrow-type wave function but found that this construction performs poorly. This low field region at moderate to high lattice anisotropy calls for more comprehensive investigation.

One of the goals we had was to explore possible new plateaus in the high field regime of $\mathrm{Cs_2CuBr_4}$. We have learned that the phase diagram is already very rich even without considering any additional plateaus. Nevertheless, for several densities such as 1/6, 2/9, and 1/4 we implemented permanent-type wave functions for various proposed CDW from Ref. [9] as well as for some additional stripe-like orderings, and inevitably found that either V or spiral has lower energy. Our earlier *uud* study showed that the 2-parton construction can also be useful for studying CDW phases; however, similar implementations at the above densities again failed to reveal any stable charge ordering. This suggests that any such order, if present at all, is likely to be very weak.

One of the findings from our study is that for the $\mathrm{Cs_2CuBr_4}$ anisotropy, the system is in the coplanar V phase close to the saturation fields, and there may be a transition to the non-coplanar spiral state at lower fields; this could be responsible for one of the features in the $\mathrm{Cs_2CuBr_4}$ experiment. We cannot exclude other more complex cascades of phases. Furthermore, additional residual interactions not treated here may be important for understanding the phases of $\mathrm{Cs_2CuBr_4}$ in the field. This remains a fascinating open problem.

3.A Motivation for $V_{\rm perm}$ wave function for $n \lesssim 1/3$, Eq. (3.11)

We begin with the *uud* state with $N/3$ bosons, Eq. (3.5), and put $N_h = N/3 - N_b$ holes in a "hole orbital" $\phi_h(R)$,

$$|\Psi\rangle \;=\; \left(\sum_R \phi_h(R) b_R\right)^{N_h} |\psi_{uud}\rangle \;. \tag{3.33}$$

For a boson configuration

$$|\eta\rangle \;=\; b^\dagger_{r_1}\dots b^\dagger_{r_{N_b}}|0\rangle \;, \tag{3.34}$$

we obtain an amplitude,

$$\langle\eta|\Psi\rangle = {\sum_{R_1\ldots R_{N_h}}}' \phi_h(R_1)\ldots\phi_h(R_{N_h}) \text{ Perm} \begin{pmatrix} \phi_1^{\mathrm{loc}}(r_1) & \ldots & \phi_{N/3}^{\mathrm{loc}}(r_1) \\ \vdots & \ddots & \vdots \\ \phi_1^{\mathrm{loc}}(r_{N_b}) & \ldots & \phi_{N/3}^{\mathrm{loc}}(r_{N_b}) \\ \phi_1^{\mathrm{loc}}(R_1) & \ldots & \phi_{N/3}^{\mathrm{loc}}(R_1) \\ \vdots & \ddots & \vdots \\ \phi_1^{\mathrm{loc}}(R_{N_h}) & \ldots & \phi_{N/3}^{\mathrm{loc}}(R_{N_h}) \end{pmatrix} \tag{3.35}$$

$$\approx \text{ Perm} \begin{pmatrix} \phi_1^{\mathrm{loc}}(r_1) & \ldots & \phi_{N/3}^{\mathrm{loc}}(r_1) \\ \vdots & \ddots & \vdots \\ \phi_1^{\mathrm{loc}}(r_{N_b}) & \ldots & \phi_{N/3}^{\mathrm{loc}}(r_{N_b}) \\ c_1 & \ldots & c_{N/3} \\ \vdots & \ddots & \vdots \\ c_1 & \ldots & c_{N/3} \end{pmatrix} . \tag{3.36}$$

The primed sum indicates that $R_1, \ldots, R_{N_h}$ need to be different from each other and from all $r_1, \ldots, r_{N_b}$. Close to the 1/3 plateau, the density of holes is small, and we can approximately replace the restricted sum by an unrestricted sum. Performing independent summations over $R_1, \ldots, R_{N_h}$ gives the last expression in the form of a single permanent, where

$$c_j = \sum_R \phi_h(R)\phi_j^{\mathrm{loc}}(R) \tag{3.37}$$

is an “overlap” of the ϕ_h and ϕ_j^{loc} orbitals. On physics grounds, the hole orbital ϕ_h needs to respect the symmetries of the *uud* state ($\phi_h = \text{const}$ over the A sublattice). In this case, c_j is independent of j, and up to a normalization constant we can replace all matrix elements in the last N_h rows by 1. The approximate single permanent form is a valid variational wave function by itself, and this is the state we use in the main text and call V_{perm}.

3.B Correlation Functions of Permanent-type States

We calculate the order parameters and correlation functions in the permanent-type trial states, since we do not have much experience with such wave functions for Mott

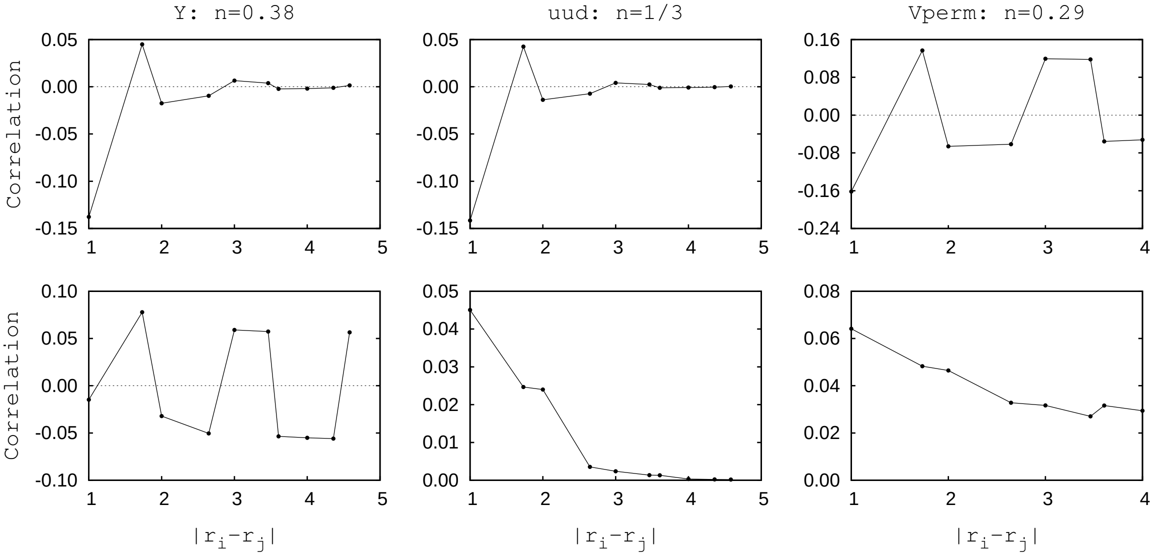

Figure 3.11: Boson correlation $\langle b_r^\dagger b_{r'}\rangle$ as a function of real space distance $|r-r'|$. Top row: r belongs to sublattice A (where $n_A > n_B = n_C$) while r' includes sites on all three sublattices. Bottom row: r belongs to sublattice B while r' includes sites on sublattices B and C. Hexagonal clusters with 84, 144, and 48 sites are respectively used for Y (left column), *uud* (middle), and V_{perm} (right) calculations.

insulators or supersolids. The non-permanent V and spiral trial states are more obvious constructions, and therefore omitted.

For Y, *uud*, and V_{perm} trial states, a 3-sublattice modulation is observed in the CDW order parameter $\langle n_r\rangle$. As expected, the density structure factor $\langle n_{-q}n_q\rangle$ reveals sharp peaks near the reciprocal vectors $\vec{Q} = \pm(\frac{4\pi}{3}, 0)$ for all three trial states.

Figure 3.11 shows the correlation functions $\langle b_r^\dagger b_{r'}\rangle$ between two sites for these trial states. The *uud* state has rapidly decaying correlations between any two sites, which is expected in this Mott insulator state. For the Y supersolid state, the correlations decay rapidly when at least one site lies on the higher density sublattice A (i.e., as if this sublattice is Mott insulating), while they are long-ranged when both sites reside on the BC honeycomb sublattice. The signs of the correlations are positive for all pairs of B-B or C-C sites, and negative for all B-C pairs, which is consistent with the Y spin order shown in Fig. 3.2. Finally, for the V_{perm} trial state, long-ranged correlation exists between any two sites on the lattice. The signs are negative for all pairs of A-B or A-C sites, and positive for all B-C pairs (as well as A-A, B-B, and C-C pairs), which is consistent with the V spin order shown in Fig. 3.2. Thus, we have verified our intuition about the physical properties of these states.

Chapter 4

Realization of Exciton Bose Liquid on a ring-exchange model

4.1 Introduction

The Exciton Bose Liquid (EBL) theory by Paramekanti *et al.* proposed a critical bosonic phase which shows remarkable resemblance to electrons in a metal[18]. For this novel quantum phase, the presence of loci of "Bose surface" in the Brillouin zone closely parallels the Fermi surface for fermions, and allows the Bose system to share many characteristics normally associated with fermions[19]. Paramekanti *et al.* showed that due to the gapless lines of excitations, EBL is a critical (power-law) compressible 2D quantum phase with uncondensed bosons and contains continuously varying exponents. Their striking proposal stimulated a number of works seeking to establish the stability of the EBL phase in bosonic models with ring exchange interactions[20, 21, 22, 23]. However, these studies found that the EBL is not realized in the hard-core boson model on the square lattice with ring exchanges on elementary plaquettes. Instead, such ring interactions favor a (π, π) charge density wave (CDW) in the half-filled case, while away from half-filling they induce strong tendencies to phase separation.

Motivated by the unusual EBL properties, our study focuses on a search for this unconventional quantum phase in simple bosonic models. A candidate model requires additional interactions for suppressing the charge order. One choice that comes to mind might be to introduce second nearest neighbor repulsion. In this work, we instead adopt a different route where we consider additional ring exchanges that frustrate the CDW tendencies of the elementary ring exchanges. We define plaquette

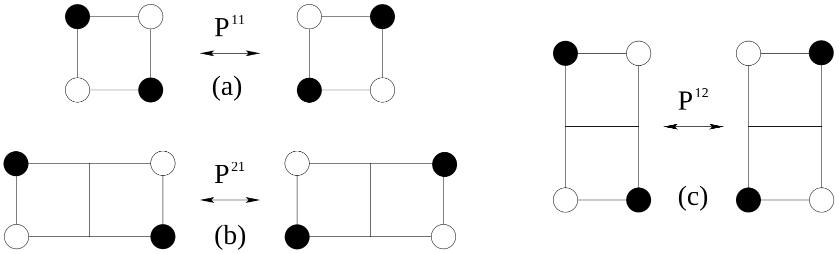

Figure 4.1: The ring exchange interactions for (a) 1×1, (b) 2×1 and (c) 1×2 plaquettes, which hop two bosons on opposite corners of a plaquette onto the two remaining vacant corners.

exchange operators

$$P_{\mathbf{r}}^{mn} = b_{\mathbf{r}}^{\dagger}\, b_{\mathbf{r}+m\hat{\mathbf{x}}}\, b_{\mathbf{r}+m\hat{\mathbf{x}}+n\hat{\mathbf{y}}}^{\dagger}\, b_{\mathbf{r}+n\hat{\mathbf{y}}} + \text{H.c.}\ , \tag{4.1}$$

where $b_{\mathbf{r}}$ annihilates a boson on a site $\mathbf{r}$, and $\hat{\mathbf{x}}, \hat{\mathbf{y}}$ are the unit vectors on the square lattice. The Hamiltonian is

$$\hat{H} = -K_1 \sum_{\mathbf{r}} P_{\mathbf{r}}^{11} - K_2 \sum_{\mathbf{r}} \left(P_{\mathbf{r}}^{12} + P_{\mathbf{r}}^{21} \right)\ . \tag{4.2}$$

Figure 4.1 illustrates the action of these ring exchanges on hoppable plaquettes. The original ring model proposed in Ref. [18] and studied numerically in Refs. [20, 21, 22, 23] corresponds to $K_2 = 0$. To see how the present K_1-K_2 model may stabilize the EBL phase, we first note that the (π,π) CDW in the K_1-only model results from having a large number of basis states connected to the perfect (π,π) CDW configuration. However, the K_2 terms would be completely inoperative in such a CDW. Furthermore, the P^{12} and P^{21} ring exchanges by themselves would favor different charge orderings and not compatible with each other. Thus, the K_2 ring terms compete with the K_1 terms and with each other, making the liquid phase with no charge order more likely.

The present K_1-K_2 model has the same lattice symmetries and boson number conservation on each row and column as the original ring model of Ref. [18]. From the outset, we define our Hilbert space as the sector with equal number of bosons on each row and column. Note that this restriction does not preclude phase separation (PS); in fact, we shall see that PS does occur at low densities within our restricted Hilbert space. For non-negative K_1 and K_2 values, the Hamiltonian does not have a sign problem and allows an unbiased study of the system using Quantum Monte Carlo methods. Although the Stochastic Series Expansion is the method of choice for simulating large lattices, it has not been applied to ring-only hard-core boson models due to implementation issues[20]. We instead use the Green's Function Monte Carlo (GFMC) approach with full bias control as described in Ref. [60], which allows us to obtain exact ground state properties for moderately sized systems up to 12×12 in this work. Without loss of generality, we set $K_1 = 1$ and vary $K_2 \geq 0$ in the study.

Our main results for the phases of the model are summarized in Figs. 4.11 and 4.14. First, at half-filling, our intuition that the K_2 should suppress the charge order is indeed borne out, and the CDW disappears already for moderate K_2. Somewhat surprisingly, this does not stabilize the EBL right away but instead drives the system into a columnar Valence Bond Solid (VBS), while the EBL is tentatively stabilized only for quite large K_2 terms. On the other hand, away from half-filling, moderate K_2 already produce stable EBL phase.

The chapter is organized as follows. In Sec. 4.2, we first construct good trial wave functions for the EBL phase and study their formal properties using Variational Monte Carlo (VMC), followed by an energetics study to determine the variational phase diagram. Using the optimal trial states as starting point for the GFMC projection in Sec. 4.3, we compute density, plaquette, and bond structure factors in the ground states, followed by finite-size scaling to determine the phases. Our phase diagram reveals the (π,π) CDW order at small K_2, VBS order for intermediate K_2, and possibly for large K_2 the novel EBL phase. We perform detailed comparison of the numerical results with the EBL theory. In Sec. 4.4, we extend the search for the EBL to densities less than half at intermediate K_2, and find that the EBL liquid is stable for $1/3 \lesssim \rho < 1/2$ while phase separation occurs at lower densities. In Sec. 4.5, we conclude with a discussion of possible further studies.

4.2 Variational study at $\rho = 1/2$

4.2.1 Formal properties of the EBL wave function

In this section, we study the formal properties of the EBL wave function. To provide motivation for the wave function, we first consider a quantum rotor version of the model with elementary 1×1 ring exchanges,

$$H_{\text{rotor}} = -K \sum_{\mathbf{r}} \cos\left(\phi_{\mathbf{r}} - \phi_{\mathbf{r}+\hat{\mathbf{x}}} + \phi_{\mathbf{r}+\hat{\mathbf{x}}+\hat{\mathbf{y}}} - \phi_{\mathbf{r}+\hat{\mathbf{y}}}\right) + \frac{U}{2} \sum_{\mathbf{r}} \left(n_{\mathbf{r}} - \bar{n}\right)^2, \tag{4.3}$$

where the phase $\phi_{\mathbf{r}}$ and the boson number $n_{\mathbf{r}}$ are canonically conjugate. In the EBL theory, the cosine in the ring term is expanded to quadratic order (this approximation

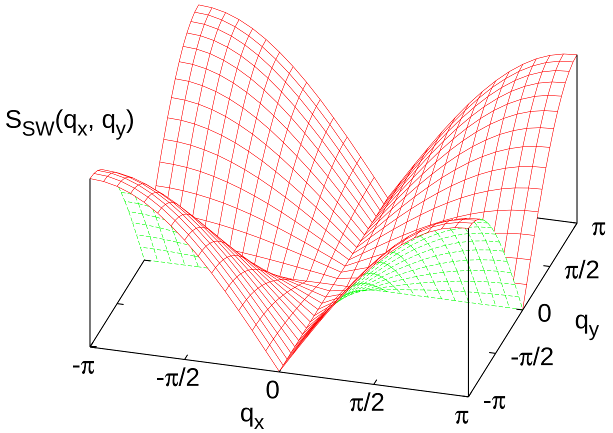

Figure 4.2: Density structure factor $S_{\mathrm{SW}}(q_x, q_y)$, Eq. (4.9), for the ground state of the spin-wave Hamiltonian, Eq. (4.4). The characteristic “cross” formed by the singular lines $q_x = 0$ or $q_y = 0$ is a distinctive feature of the EBL phase.

is valid in the stable “spin-wave phase” with no topological defects). The resulting set of coupled harmonic oscillators can be diagonalized in momentum space, which leads to the following,

$$H_{\mathrm{SW}} = \sum_{\mathbf{q}} \left(\frac{U}{2}\, n_{\mathbf{q}}\, n_{-\mathbf{q}} + \frac{\omega_{\mathbf{q}}^2}{2U}\, \phi_{\mathbf{q}}\, \phi_{-\mathbf{q}} \right), \tag{4.4}$$

$$\omega_{\mathbf{q}} = 4\sqrt{UK} \left| \sin\left(\frac{q_x}{2}\right) \sin\left(\frac{q_y}{2}\right) \right| . \tag{4.5}$$

We will loosely refer to H_{SW} as the “spin-wave” Hamiltonian. Writing its ground state in the n variables and then restricting to $n_{\mathbf{r}} \in \{0, 1\}$, we obtain a valid hard-core boson wave function in the convenient Jastrow-type form that can be implemented easily in VMC,

$$\Psi_{\mathrm{EBL}} \propto \exp\left[-\frac{1}{2} \sum_{\mathbf{r},\mathbf{r}'} u(\mathbf{r}-\mathbf{r}')\, n_{\mathbf{r}} n_{\mathbf{r}'} \right], \tag{4.6}$$

$$u(\mathbf{r}) = \frac{1}{L^2} \sum_{\mathbf{q}} \frac{W\, e^{i\mathbf{q}\cdot\mathbf{r}}}{4\,|\sin(q_x/2)\sin(q_y/2)|}. \tag{4.7}$$

In the spin-wave theory, $W = \sqrt{U/K}$, while here it serves as a variational parameter. For the K_1-K_2 model, W becomes a $\mathbf{q}$-dependent function with two parameters. In this section, we will focus on the single-parameter EBL wave function to illustrate properties of such variational states and what can happen with them.

To characterize the phases realized in the EBL wave function, we measure the density structure factor

$$S(q_x, q_y) = \frac{1}{L^2} \sum_{\mathbf{r},\mathbf{r}'} e^{i\mathbf{q}\cdot(\mathbf{r}-\mathbf{r}')} \langle n_{\mathbf{r}} n_{\mathbf{r}'} - \bar{n}^2 \rangle \ . \tag{4.8}$$

The density structure factor of the ground state for the spin-wave Hamiltonian in Eq. (4.4) is given by

$$S_{\text{SW}}(q_x, q_y) = \frac{2}{W} \left| \sin\left(\frac{q_x}{2}\right) \sin\left(\frac{q_y}{2}\right) \right| . \tag{4.9}$$

At any fixed q_y, $S_{\text{SW}}(q_x, q_y)$ vanishes for small q_x as $C(q_y)|q_x|$, with further $C(q_y) \sim |q_y|$ as $q_y \to 0$. This gives the characteristic "cross" shown in Fig. 4.2 which is a signature of the compressibility of the EBL, and is related to the gaplessness of $\omega_{\mathbf{q}}$ along the loci $q_x = 0$ or $q_y = 0$. The latter is a consequence of the conservation of boson number along each row and each column of the lattice. To identify possible realization of the EBL phase, we monitor the long-wavelength behavior of the density structure factor in addition to the absence of Bragg peaks in all structure factor measurements made in this study.

For sufficiently strong interaction U (in particular, for hard-core model) at half-filling, the spin-wave approximation no longer holds. Proliferation of topological defects results in the (π,π) CDW instability found in earlier Quantum Monte Carlo studies[18, 20, 21, 22, 23]. Remarkably, we find that the single-parameter EBL wave function Eq. (4.6) is able to realize both the EBL and the CDW phase. As we increase W in the half-filled system, the wave function undergoes a phase transition at a critical value $W_c \approx 4.4$ where the (π, π) charge order develops. This is analyzed in the top panel of Fig. 4.3 using finite-size scaling of $S(\pi, \pi)/L^2$, which vanishes as $1/L^2$ in the absence of the order for $W < W_c$ and approaches a finite value in the presence of the order for $W > W_c$. The non-monotonic L dependence of this CDW order parameter for fixed $W > W_c$ is somewhat unusual but appears to be a property of such wave functions, perhaps indicative of some long crossovers in the system.

Next we examine the long-wavelength behavior of the density structure factor near the characteristic "cross." Figure 4.3 also shows the ratio

$$\sigma(q_x, q_y) \equiv \frac{S(q_x, q_y)}{4|\sin(q_x/2)\sin(q_y/2)|} \tag{4.10}$$

evaluated at the smallest $q_x = q_{\text{min}} = 2\pi/L$ as a function of q_y on lattices with length L between 10 and 80. For $W = 4.2$ in the middle panel, the ratio shows

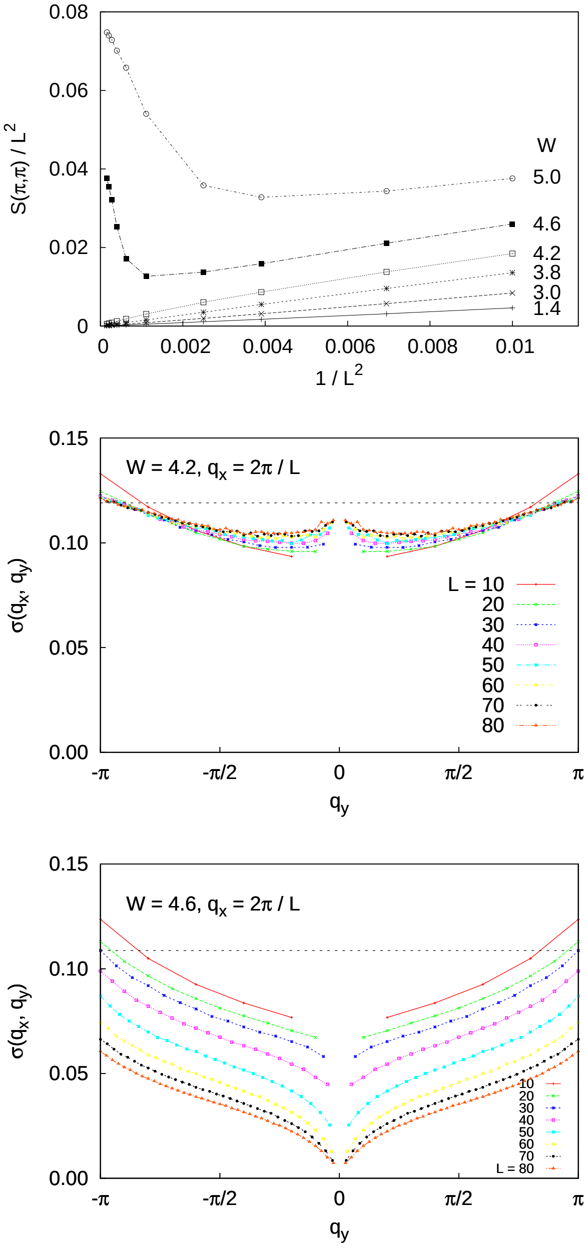

Figure 4.3: VMC study of the EBL wave function in Eq. (4.6) with one parameter W defined by Eq. (4.7). Top: finite-size scaling of the density structure factor $S(\pi, \pi)$. The wave function undergoes a transition at a critical value $W_c \approx 4.4$, which separates the EBL phase at low W from the (π,π) CDW at larger W. Middle and bottom: $\sigma(q_x = 2\pi/L, q_y)$, Eq. (4.10), which gives normalized slopes of the density structure factor near the cross, plotted against q_y for lattice length $L = 10$ to 80. Middle: Results for $W = 4.2$ show long-wavelength EBL characteristics where these normalized slopes approach finite values [apparently close to $\sigma_{\rm SW} = 1/(2W)$ indicated with a dotted line]. Bottom: Results for $W = 4.6$ show a downward renormalization of the slopes, which is similar to a gapped state. The critical values estimated from both the order parameter study and the detailed study of the cross agree, i.e., $W_c \approx 4.4$.

some deviation from $\sigma_{\mathrm{SW}} = 1/(2W)$ but it clearly renormalizes towards finite values as expected in the EBL theory. When plotted in the full Brillouin zone, the VMC density structure factor looks essentially like Fig. 4.2.

On the other hand, for $W = 4.6$ in the bottom panel, a strong downward renormalization of the ratio is observed for all q_y, in particular near $q_y = 0$. Such behavior is similar to a Mott insulator, where the density structure factor is non-singular and hence has cuts $(q_x \to 0, q_y)$ with vanishing slopes. Thus, the contrasting long-wavelength behaviors of $S(q_x, q_y)$ independently confirm a phase transition in the wave function near $W_c \approx 4.4$.

To summarize, the above wave function with one variational parameter can realize either the EBL liquid phase or the (π, π) charge order and thus can alert us about CDW tendencies in the system. A note of caution is appropriate here. Our GFMC study in later Sec. 4.3 shows that the formal wave function study of the present section does not always capture a full physics of the problem. Namely, as we will discuss in Sec. 4.3.4, the wave function itself may be in the liquid phase, while the full EBL theory with the same effective K/U is already unstable. Nevertheless, our formal wave function study clearly has its own merits. For instance, it alerts us to the possibility of complex crossovers with the system size and that the order may be weak and not apparent on short scales, but may still appear on longer scales. It also teaches us to look at the long-wavelength behavior for signs of instabilities.

4.2.2 K_1-K_2 energetics study with one-parameter EBL wave function

Let us turn to the energetics study using the above one-parameter wave function. For each value of K_2 and system size L we find the optimal variational parameter W (later Fig. 4.6 compares the trial energies with the exact diagonalization values on the 6×6 lattice). In Fig. 4.4, finite-size scaling of the corresponding structure factor $S(\pi, \pi)$ shows the presence of the CDW order for small K_2 and the absence for $K_2 \geq 0.3$. Thus, the VMC study suggests that the EBL phase could be stabilized even with quite weak K_2 ring interactions. Allowing an additional variational parameter corresponding to K_2 in the spin-wave Hamiltonian does not modify this conclusion. Figure 4.5 summarizes the VMC results obtained for the K_1-K_2 ring model at half-filling. In the following section, our GFMC simulation reveals another phase in the intermediate K_2 region. We will present a revised phase diagram based on unbiased GFMC results in Sec. 4.3.2, and will discuss the failure of the VMC later in Sec. 4.3.4.

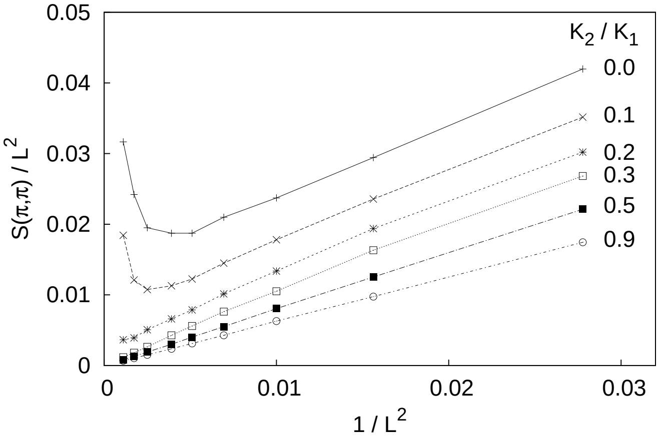

Figure 4.4: finite-size scaling of the VMC density structure factor $S(\pi,\pi)$ obtained in the energetics study using optimized W for each K_2 in the Hamiltonian and each system size L.

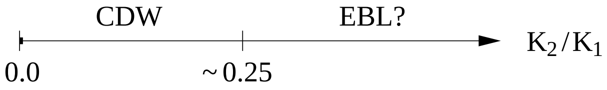

Figure 4.5: Variational phase diagram for the K_1-K_2 model on the half-filled square lattice, based on the single-parameter trial wave function. Refer to Fig. 4.11 for a revised phase diagram based on unbiased GFMC results.

4.3 Unbiased GFMC study at $\rho = 1/2$

In this section, we perform a Green's function Monte Carlo study which, being unbiased, provides an important check on the VMC results. In the GFMC approach, an initial trial wave function is projected onto the ground state via repeated application of a projector which eventually filters out the excited states:

$$|\psi_{n+1}\rangle = [1 - (\hat{H} - E_0)\delta\tau]|\psi_n\rangle. \tag{4.11}$$

Here E_0 is a parameter chosen close to the ground state energy, and $\delta\tau$ is a "time step" chosen to ensure dominance of the ground state and positiveness of the projector, which then allows Monte Carlo calculations without a sign problem. Operator expectation values are evaluated using stochastically sampled ground states which generally requires the so-called GFMC "forward walking" technique, and we implement this using the bias-controlled scheme described in Sec. 2.4.2. We refer the reader to the literature for more details on the GFMC[59, 61, 85, 60].

To identify the nature of the true ground states, we measure the density structure factor $S(q_x, q_y)$ defined in Eq. (4.8) as well as the following plaquette structure factor

$$P(q_x, q_y) = \frac{1}{L^2} \sum_{\mathbf{r},\mathbf{r}'} e^{i\mathbf{q}\cdot(\mathbf{r}-\mathbf{r}')} \langle (P^{11}_{\mathbf{r}})^2 \ (P^{11}_{\mathbf{r}'})^2 \rangle \ , \tag{4.12}$$

where $(P^{11}_{\mathbf{r}})^2$ equals 1 if the 1×1 plaquette is "hoppable" and 0 otherwise. While quantitatively different from the off-diagonal $P^{11}_{\mathbf{r}}$ plaquette structure factor used in Ref. [20], the operator $(P^{11}_{\mathbf{r}})^2$ defined here is easier to implement in the GFMC and it gives qualitatively the same access to bond-solid-type phases. To better discriminate between plaquette and bond orders, we also measure the following bond structure factor:

$$B_\alpha(q_x, q_y) \quad = \quad \frac{1}{L^2} \sum_{\mathbf{r},\mathbf{r}'} e^{i\mathbf{q}\cdot(\mathbf{r}-\mathbf{r}')} \langle (B^{\alpha}_{\mathbf{r}})^2 \ (B^{\alpha}_{\mathbf{r}'})^2 \rangle \ , \tag{4.13}$$

where $B^\alpha_{\mathbf{r}} = b^\dagger_{\mathbf{r}} b_{\mathbf{r}+\hat{\alpha}} + b^\dagger_{\mathbf{r}+\hat{\alpha}} b_{\mathbf{r}}$ and $\alpha \in \{\hat{x}, \hat{y}\}$; thus, $(B^\alpha_{\mathbf{r}})^2$ is 1 if the bond is "hoppable" and 0 otherwise, and is again easy to implement in the GFMC.

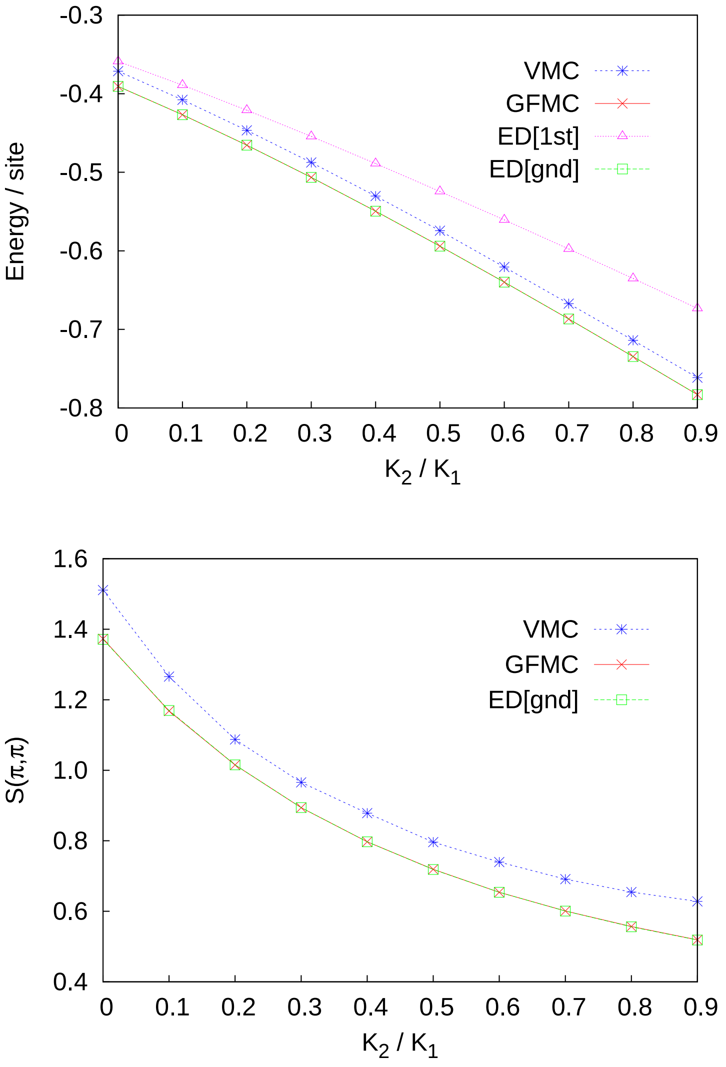

Figure 4.6: Top: Comparison of the 6×6 lattice VMC and GFMC energies per site against the ED ground state and first excited state values for $0 \leq K_2 \leq 0.9$. For $K_2 \geq 0.2$, the VMC energies are already closer to the ground state than to the first excited state; however, despite such a good agreement in the energies, the VMC fails to identify a new phase for $K_2 \geq 0.3$ as described in the text. Bottom: Comparison of the corresponding VMC and GFMC structure factors $S(\pi, \pi)$ against the ED values. The GFMC energies and structure factors show complete agreement with the ED values.

K_2	E_{VMC}	E_{GFMC}	E_{ED}	$S_{\text{VMC}}^{(\pi,\pi)}$	$S_{\text{GFMC}}^{(\pi,\pi)}$	$S_{\text{ED}}^{(\pi,\pi)}$
0.0	-0.3714	-0.39075	-0.39075	1.511	1.368	1.371
0.1	-0.4078	-0.42675	-0.42675	1.266	1.168	1.170
0.2	-0.4467	-0.46552	-0.46552	1.087	1.015	1.015
0.3	-0.4875	-0.50658	-0.50658	0.966	0.894	0.894
0.4	-0.5303	-0.54953	-0.54953	0.878	0.797	0.797
0.5	-0.5744	-0.59406	-0.59406	0.796	0.719	0.719
0.6	-0.6206	-0.63988	-0.63988	0.740	0.654	0.654
0.7	-0.6672	-0.68678	-0.68678	0.691	0.601	0.601
0.8	-0.7139	-0.73455	-0.73456	0.655	0.557	0.556
0.9	-0.7614	-0.78307	-0.78307	0.628	0.519	0.518

Table 4.1: Comparison of the ground state energy and $S(\pi,\pi)$ obtained using the VMC, GFMC, and ED calculations for the 6×6 lattice. The energies are given in units of K_1 per lattice site. The GFMC results are essentially exact, and we treat them as such for larger sizes.

4.3.1 Test of our GFMC setup

In Fig. 4.6, we test our GFMC setup against exact diagonalization (ED) calculations for the 6×6 lattice. All results are in the sector with three bosons in each row and in each column. On both panels, the GFMC and ED results essentially coincide for the entire K_2 range shown. Table 4.1 summarizes the respective data for reference. To check the accuracy of the trial wave functions, the VMC energies are also plotted in the top panel of Fig. 4.6 along with the first excited state ED energies. For $K_2 \geq 0.2$, the VMC energies are already closer to the ground state than to the first excited state. We caution the reader that despite this very good accuracy on the 6×6 system, the VMC fails to identify another order that develops for larger K_2 and is found by the GFMC for larger sizes.

4.3.2 GFMC study of the K_1-K_2 model at half-filling

We now proceed to apply this numerical tool to characterize the ground states of the K_1-K_2 ring model. The top panels in Figs. 4.7 and 4.8 show the density structure factor $S(\pi,\pi)$ and the plaquette structure factor $P(\pi,0)$ plotted against K_2 for lattice sizes ranging from $L = 6$ to 12. Between $K_2 = 0$ and 0.4, $S(\pi,\pi)$ increases strongly with L while the size dependence weakens with K_2. This coincides with a strengthening size dependence of $P(\pi,0)$. Beyond $K_2 = 0.4$, the charge order is absent while the plaquette order now dominates in the range up to $K_2 \approx 4$. For still larger K_2, $P(\pi,0)$

becomes very weakly dependent on lattice size. We do not observe any other strong feature in $S(q_x, q_y)$ and $P(q_x, q_y)$ over the full Brillouin zone. Thus we identify the (π,π) CDW for $0 \leq K_2 < 0.4$, a $(\pi, 0)$ bond-solid-type phase for the intermediate K_2 region, and tentatively an EBL phase for $K_2 > 4$. The middle panels in Figs. 4.7 and 4.8 show finite-size scalings of the respective order parameters which support these conclusions.

The bottom panels in Figs. 4.7 and 4.8 show the corresponding Binder ratios defined as

$$\text{Binder ratio} = \frac{\langle |M|^4 \rangle}{\langle |M|^2 \rangle^2} \tag{4.14}$$

with $M_{\text{CDW}} = \sum_{\mathbf{r}} e^{i(\pi,\pi)\cdot\mathbf{r}} n_{\mathbf{r}}$ or $M_{\text{VBS}} = \sum_{\mathbf{r}} e^{i(\pi,0)\cdot\mathbf{r}} (P_{\mathbf{r}}^{11})^2$ (so $\langle |M|^2 \rangle$ are simply proportional to the already discussed structure factors). The Binder ratios provide additional information about the fluctuations of the order parameters (via the measurement $\langle |M|^4 \rangle$) and are expected to approach 1 in the presence of the order and 3 in the absence of the order. Such change in the behavior is clearly seen when the CDW order disappears and the plaquette order appears near $K_2 \sim 0.3 - 0.4$. Note, however, that the familiar Binder crossing technique apparently does not work for the CDW order parameter for our sizes, even though we are confident that the CDW order disappears (also supported by the values ≈ 3 of the Binder ratio itself). Note also strong and non-systematic size dependence, particularly for the smallest $L = 6$. In the plaquette Binder ratio, we see lack of order for small K_2, appearance of order for intermediate K_2, and apparently "disordered" Binder values for $K_2 \gtrsim 4$ (which is consistent with the absence of the plaquette order), but no clear crossings for this transition. Although the Binder data does not clearly give us the critical value of K_2 for the transition to the disordered phase, its limiting value strongly suggests that there is no $(\pi, 0)$ or $(0, \pi)$ plaquette order at large K_2. An additional lesson from this study is that we should be aware of particular strong finite-size effects in this system.

Our identification of the VBS order for the intermediate K_2 region is further helped by measurement of the bond structure factor $B_x(q_x, q_y)$ defined in Eq. (4.13). For this measurement (not shown), similarly to the plaquette structure factor, we observe $(\pi, 0)$ and $(0, \pi)$ Bragg peaks but no peak at (π, π). This is more consistent with a "columnar" VBS order rather than a plaquette order, and is also similar to the phase found by Sandvik *et al.*[20] in the J-K model for $8 \lesssim K/J \lesssim 14$. Our finding of the same VBS state may in fact be related, since J added to the pure K_1 model may induce effective K_2 ring exchanges frustrating the CDW while still remaining in the Mott insulator.

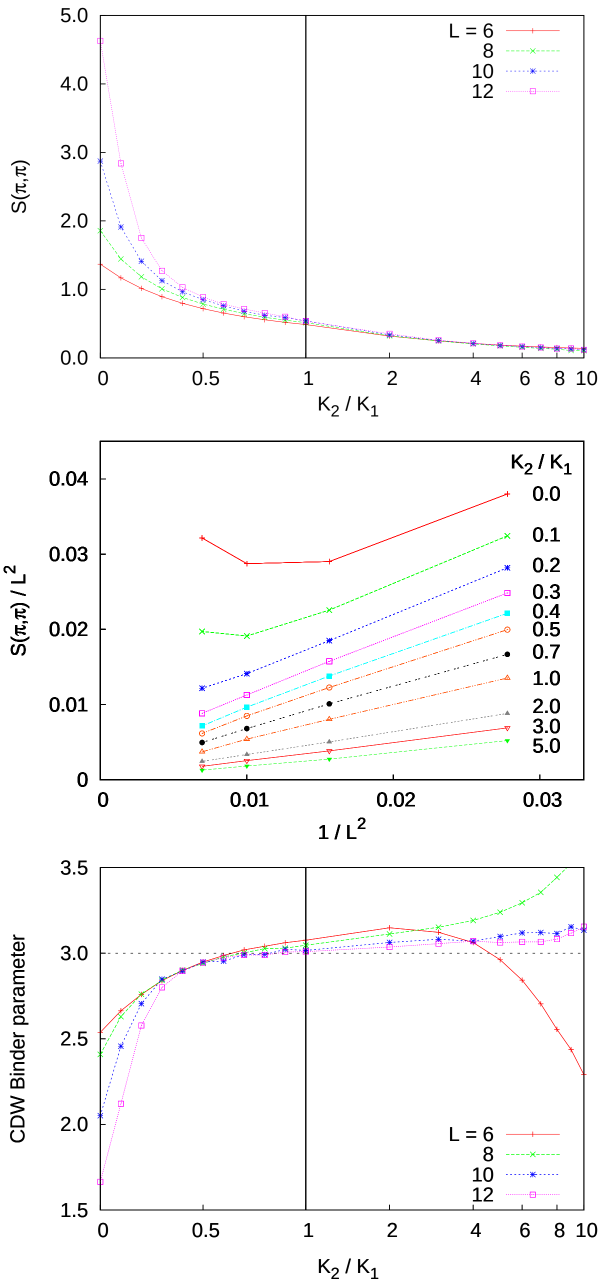

Figure 4.7: Top: GFMC density structure factor $S(\pi, \pi)$ versus K_2 for periodic lattices with length $L = 6, 8, 10$ and 12. Note that to show the data compactly, taken for $K_2 = 0$ to 1 in steps of 0.1 and $K_2 = 1$ to 10 in steps of 1, we used linear scale for the first range but log scale for the second range. Middle: finite-size scaling of $S(\pi, \pi)$. Bottom: Binder ratio, Eq. (4.14), for the CDW order parameter. Note the apparently large finite-size effect in the ratio, particularly for sizes $L = 6$ and 8 at large K_2, and also absence of clear Binder crossings. Nevertheless, the Binder data is generally consistent with a lack of CDW order for $K_2 \gtrsim 0.3$, as can be seen from the ratio approaching the expected "disordered" value 3 (shown with a dotted line).

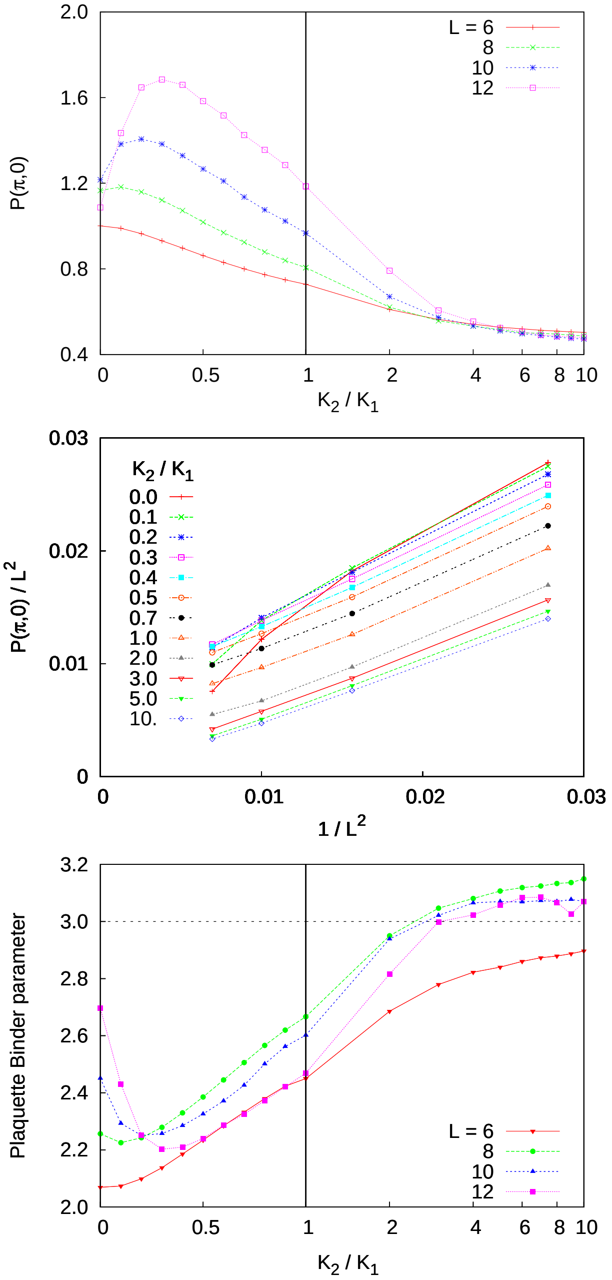

Figure 4.8: Top: GFMC plaquette structure factor $P(\pi, 0)$ versus K_2 for periodic lattices with length $L = 6, 8, 10$ and 12. Linear scale is used for $K_2 = 0$ to 1 in steps of 0.1, and log scale for $K_2 = 1$ to 10 in steps of 1. Middle: finite-size scaling of $P(\pi, 0)$. Bottom: Binder ratio, Eq. (4.14), for the bond-solid order parameter. The Binder data is consistent with no VBS order for small K_2 and VBS order for intermediate K_2. The observation of Binder ratios exceeding the disordered value 3 suggests that there is no order for large K_2, although there is no clear crossing going to the large K_2 phase (note that similar somewhat unusual behavior is also seen in the CDW Binder data when the CDW order disappeared.)

To get a more complete picture, we examine the long-wavelength behavior of the density structure factor using the "cross analysis" of Sec. 4.2.1. Figure 4.9 shows the "normalized slopes" $\sigma(q_x\!=\!2\pi/L, q_y)$, Eq. (4.10), for $L = 6$ to 12. The left panel shows the results for $K_2 = 0$, which we already know is in the CDW phase from the presence of the (π,π) Bragg peak. We clearly observe a Mott-like incompressible behavior where the slopes vanish. This is similar to the earlier formal wave function study with the CDW. The Mott-like dependence of $S(q_x, q_y)$ at long-wavelengths continues to be present after the charge order disappears for $K_2 \gtrsim 0.4$. This is illustrated in the middle panel for $K_2 = 1$, at which the bond-solid ordering is already established in Fig. 4.8. Our "cross analysis" therefore provides an independent detection of the instability to a different solid.

In the right panel of Fig. 4.9 for $K_2 = 7$, our small-lattice data appears to suggest that $S(q_x, q_y)$ does have the V-shaped singularity along the lines $q_x = 0$ or $q_y = 0$. This would mean that the bond-solid ordering exists only at intermediate K_2 and hence, possibly realizing the EBL phase at large K_2. However, this panel also reveals a weak downwards renormalization of the slopes upon increasing L and we therefore do not rule out the possibility of the EBL behavior disappearing at much larger lattice sizes.

A rigorous confrontation of the large K_2 region requires a study on much larger lattices, but this is beyond the capability of our present numerical setup. We instead examine the structure factors $S(q_x, q_y)$ and $P(q_x, q_y)$ over the entire Brillouin zone and look for signatures of the EBL phase as well as potential instabilities. The top panel in Fig. 4.10 shows the density structure factor at $K_2 = 7$ and clear absence of any CDW ordering. Here, we highlight the presence of the long-wavelength EBL signature near the lines $q_x = 0$ and $q_y = 0$ (this characteristic cross has already been analyzed in Fig. 4.9). The middle panel in Fig. 4.10 shows the plaquette structure factor for the same system, which again does not show bond or plaquette ordering. Despite the potential instability hinted by the $P(\pi, 0)$ and $P(0, \pi)$ cusps, the size independence of the plaquette structure factor along the cut $q_x = \pi$ shown in the bottom panel of Fig. 4.10 gives us some confidence that the EBL phase may indeed be realized in the large K_2 regime at half-filling.

Figure 4.11 summarizes the unbiased GFMC phase diagram obtained for the K_1-K_2 model at half-filling.

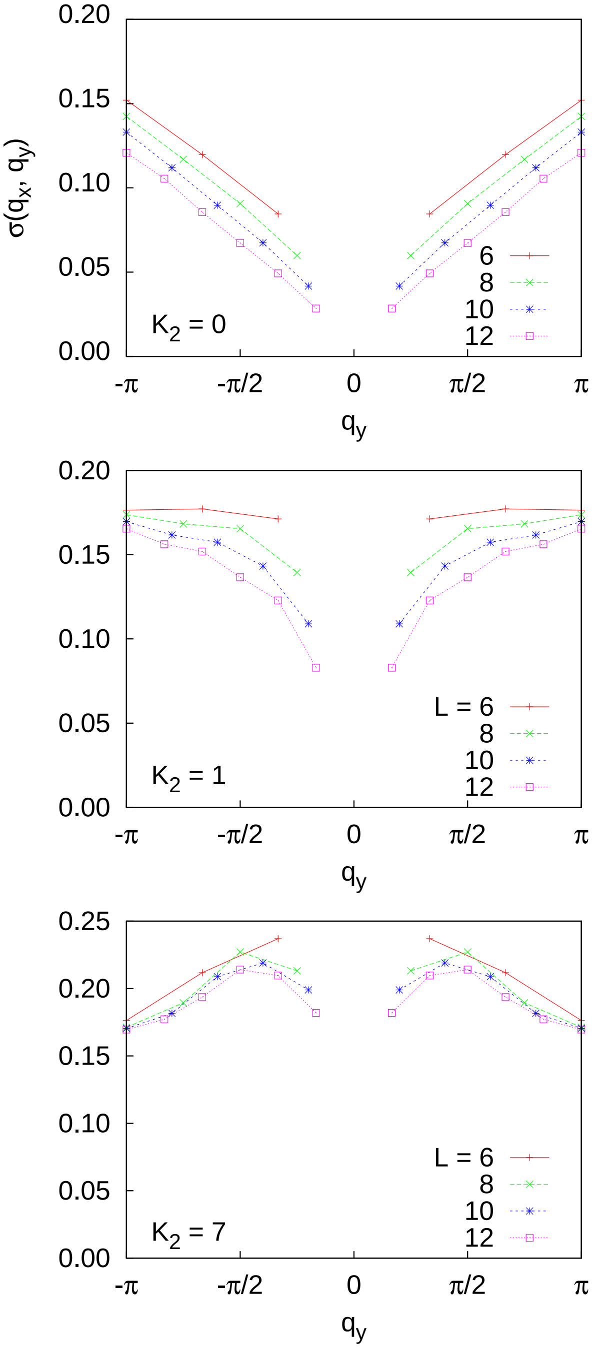

Figure 4.9: "Cross analysis" of the density structure factors, plotting "normalized slopes" $\sigma(q_x = 2\pi/L, q_y)$, Eq. (4.10), versus q_y for $L = 6$ to 12. Left: $K_2 = 0$ in the CDW phase; the vanishing of the slopes is consistent with non-singular behavior expected in an incompressible system. Middle: $K_2 = 1$ in the VBS phase; the vanishing of the slopes continues to be present and can be used as an indication of the EBL instability even if we did not know the resulting order. Right: $K_2 = 7$ (note different vertical scale); the data shows non-zero normalized slopes and only weak renormalizations, therefore suggesting a stable EBL phase.

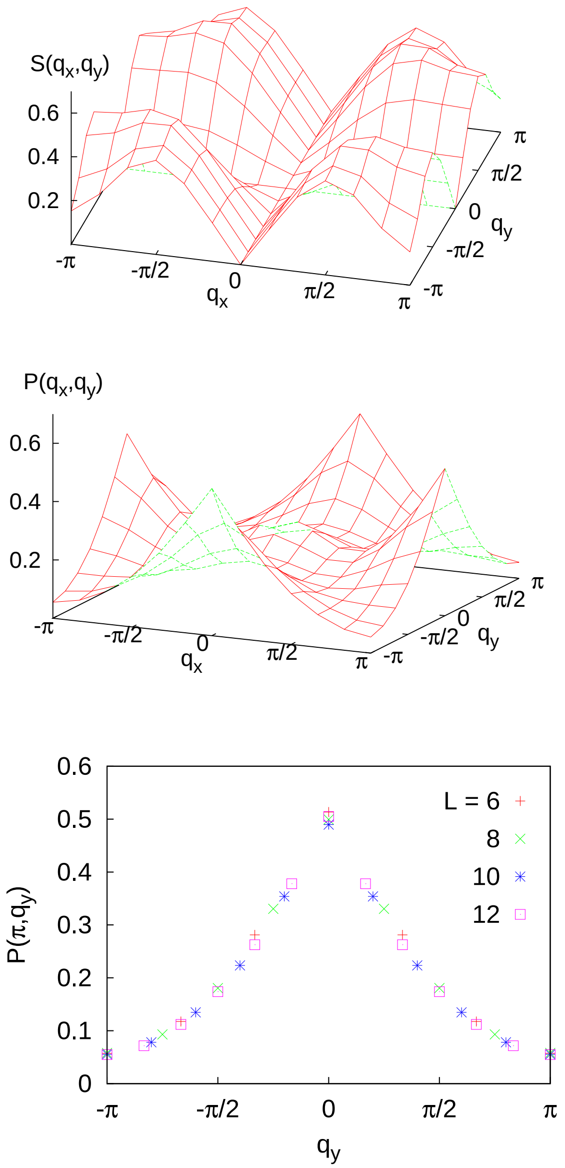

Figure 4.10: Top: GFMC density structure factor $S(q_x, q_y)$ for a 12×12 lattice at $K_2 = 7$. Middle: GFMC plaquette structure factor $P(q_x, q_y)$ for the same system ($\mathbf{q} = \mathbf{0}$ point not calculated). Bottom: Cut of $P(q_x, q_y)$ at $q_x = \pi$ for $L = 6$ to 12.

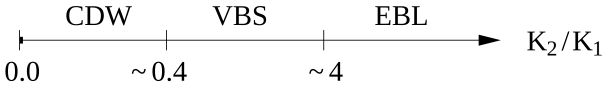

Figure 4.11: GFMC phase diagram for the K_1-K_2 model on the half-filled square lattice. We found the (π, π) CDW for $K_2 \lesssim 0.4$, the $(\pi, 0)$ VBS for intermediate values of K_2, and possibly the EBL phase for $K_2 \gtrsim 4$.

4.3.3 More detailed comparison with the EBL theory and interpretations

We now discuss how the presented results at half-filling may fit into the EBL theory framework. The EBL is characterized by an "EBL phase stiffness." For example, in the spin-wave theory Eq. (4.4), the EBL stiffness is simply K/U, which we will parametrize by $\kappa = \sqrt{K/U}$. More generally, the EBL stiffness is a *function* on the cross lines $q_x = 0$ or $q_y = 0$, with convenient parametrization by $\kappa(q_y) = \sqrt{\mathcal{K}(0, q_y)/\mathcal{U}(0, q_y)}$, which determines exponents in various power-law correlations along lattice directions, which in turn determine stability of the EBL.

We do not have a direct access to the EBL phase stiffness in our setup, but we can crudely monitor its behavior using the characteristic cross in the density structure factor. Specifically, the "normalized slopes" from the EBL theory is given by[3]:

$$\sigma(0, q_y) = \frac{\kappa(q_y)}{2} \times |C_\rho(0, q_y)|^2 \ . \tag{4.15}$$

Here $C_\rho(\mathbf{q})$ is a non-universal function of order 1. In the spin-wave theory, $C_\rho(\mathbf{q}) = 1$. In general, $C_\rho(\mathbf{q} \to \mathbf{0}) = 1$, and we conjecture also that $C_\rho(q_x \to 0, q_y) = 1$ for any q_y, but we do not know for sure. If we can indeed ignore the $|C_\rho(0, q_y)|^2$ factor in Eq. (4.15), we can then view our "cross analysis" presented earlier as a crude measure of the effective EBL stiffness on the corresponding length scales. When the measured $\sigma(q_{\min} = 2\pi/L, q_y)$ renormalizes down to small values upon increasing the system size, the EBL is unstable; when $\sigma(2\pi/L, q_y)$ stays finite, the EBL is stable.

The theoretical stability of the EBL requires the stiffness to be sufficiently large, and the condition is particularly stringent at half-filling because of allowed Umklapp interactions. The corresponding scaling dimensions depends on $\kappa(q_y)$ (see Appendix A of Ref. [3]) and the leading Umklapp has scaling dimension that becomes irrelevant if

$$\kappa > 3/8 \ , \tag{4.16}$$

which we can take as a rough guide at half-filling. Our EBL cross analysis of the density structure factor gives $\sigma \approx \kappa/2$, so to establish stability we would like to see $\sigma \geq 3/16 = 0.1875$. For $K_2 = 7$ this is satisfied on average for sizes $L = 6$ to 12, but the larger sizes come close to the threshold. The state may be somewhat more stable in that the measured $\sigma(q_y)$ is largest near $q_y = \pi/2$ and the particular "average" of $\kappa(q_y)$ that one needs has the main weight in the middle of the region $[0, \pi]$. [We also want to repeat that we are not sure whether we can ignore the factor $|C_\rho|^2$ in

Eq. (4.15) and unambiguously extract κ from σ.] From the absence of any orders, we conjecture that this point is stable; of course, if the instability is very weak, we may be not detecting the order on our length scales.

For $K_2 = 0$ and $K_2 = 1$, the effective EBL stiffness parameters as estimated by the cross analysis in Fig. 4.9 are below critical or border-line critical already for the size $L = 6$ and then quickly renormalize down upon increasing L, consistent with our finding of the instability of the EBL towards boson solid phases.

When the EBL is unstable at half-filling, the natural outcomes are a (π, π) CDW or a plaquette solid with period 2 in both lattice directions. The outcome depends on the sign of some effective couplings. If an effective nearest neighbor repulsion dominates, the solid locks into the CDW, while if the second-neighbor repulsion dominates, the solid locks into the plaquette state. We then propose that, as we increase the K_2, while the EBL remains unstable (e.g., as detected by the cross analysis), at some point the sign of the locking switches from the CDW to the bond-solid. (At present, we do not know how to realize the columnar VBS out of the EBL theory, but usually columnar and plaquette orders are related[86, 87, 88, 89] and perhaps we are missing some physics ingredients in the theory that would enable the columnar VBS.) As we further increase K_2, we conjecture that the Umklapp eventually becomes irrelevant and the stable EBL is realized. In this scenario, we do not anticipate any other instability, so if the presented large K_2 region is eventually unstable, the simplest possibility is that it will have a very small VBS order.

4.3.4 Interpretation of the failure of the VMC at $\rho = 1/2$

In light of the above stability considerations, we now briefly discuss the failure of the formal wave function study in Sec. 4.2 to detect the EBL instability in the intermediate K_2 regime. We presented mainly the one-parameter wave function that can capture only the EBL or CDW. However, we also considered a two-parameter wave function where in the spin-wave theory like Eq. (4.4) we include both K_1 and K_2 ring terms (in fact, this was used throughout to obtain improved initial states for the GFMC projection). We found that such a wave function, depending on the parameters, can realize also the VBS state on the same footing as the CDW[2]. Nevertheless, in the energetics study in the intermediate K_2 regime, the optimized two-parameter wave function produces a liquid.

The one-parameter example from Sec. 4.2 is sufficient for our discussion. The wave function is constructed from the EBL spin-wave theory and it seems reasonable to take the EBL parameter as $\kappa = 1/W$. Consider now $W = 4.2$ shown in the middle panel in Fig. 4.3, where the normalized slopes in the density structure factor approached the expected value $\sigma_{\rm SW} = 1/(2W)$ and where we concluded that the VMC wave function is in the liquid phase. However, such stiffness $\kappa = 0.24$ strongly violates the stability condition Eq. (4.16). Therefore, we appear to have a situation where the formal wave function is a liquid with a stiffness that is too small for the full EBL theory to be stable.

This is reminiscent of what happens when one formally considers a Jastrow-type wave function for 1D hard-core bosons, $\Psi_{1D} = \Pi_{i<j} |\sin[\pi(x_i - x_j)/L]|^{\nu}$. The wave function describes a Luttinger liquid of bosons with the Luttinger parameter $g = 1/\nu$. On a half-filled chain, the Luttinger liquid becomes unstable to a staggered CDW when $g < 1/2$ corresponding to $\nu > 2$. However, as discussed in Ref. [90], the above wave function remains liquid until ν exceeds 4, and only then the CDW order develops. Thus, in this 1D example, the condition for the formal stability of the wave function is different from that in the full theory.

Assuming similar phenomenon for the formal EBL wave function, we can then speculate on what happened in our variational study. The wave function parameter is found by optimizing the energetics and it roughly captures the bare EBL stiffness on the scale of few lattice spacings. For small K_2, this is already in the regime where both the wave function and the full EBL theory are unstable. However, for intermediate K_2 the optimized parameters happen to be in the range where the wave function is stable while the full EBL theory is not, hence the failure of our VMC. Of course, once we suspect boson-solid phases, the use of the few-parameter wave functions motivated from the liquid side becomes inadequate. In the variational approach, more parameters also allowing the Jastrow pseudopotentials to become more long-ranged would be needed[91, 92], while in the present study the correct physics is brought by the GFMC projection.

4.4 Study of the K_1-K_2 model for $\rho < 1/2$

When we step away from half-filling, the Umklapp terms discussed above are no longer allowed. While the EBL may still be unstable due to non-Umklapps, they are typically less relevant. However, here one also competes against phase separation at low densities. Previous studies[21, 22, 23, 79] of boson models with 1×1 ring exchanges found that ring interactions induce strong tendency to phase separation, since they are operative only when bosons are nearby. The more extended K_2 ring interactions can somewhat offset this tendency and produce a stable uniform EBL regime over a wider range of densities below half-filling.

We would like to point out that our restricted Hilbert space with equal boson number in each row and each column does not preclude phase separation. For example, basis states with preferential clumping along a diagonal or in blocks along the diagonal are present in our Hilbert space. In fact, we observe regimes of phase separation in the VMC and GFMC simulations which will be discussed below. We detect the phase separation in the Monte Carlo simulations either by monitoring snapshots of the real-space boson configurations, or by looking at the structure factors in momentum space, where it is revealed by the presence of strong peaks at the smallest wavevectors. To further check the results, we start our simulations from both uniform (random) boson configurations and from half-filled diagonal stripes. We verified that, independent of the initial configurations, our simulations converge to uniform states for densities close to 1/2 but phase-separate for low densities.

It may be true that in our working sector the phase separation is somewhat suppressed in finite samples, since other shapes of clumped regions are not allowed. However, this effect should decrease with increasing system size, and it is likely that our sizes already crudely capture such local energetics tendencies as to whether the system wants to stay uniform or phase-separate.

Below, we present results of a VMC energetics study on a 24×24 lattice and results of a GFMC study on lattices with $L \leq 12$. We find that a stable EBL phase is present in a window $\rho \in (0.4, 0.5)$ for K_2 as small as 0.5.

4.4.1 VMC results for 24×24 lattice

For our VMC energetics study of the uniform liquid phase on the 24×24 lattice, we use the single-parameter EBL wave function from Eq. (4.6). We consider total boson numbers in multiples of 24, as appropriate for the Hilbert space with equal number of bosons in each row and column. Figure 4.12 shows the trial energy per site for the optimized EBL wave function plotted against boson density. Away from half-filling, uniform VMC liquids are obtained for all data points shown in the figure. For $\rho \lesssim 0.13$, we already detect phase separation in the VMC simulations (data points for these cases were excluded from the plot). Among the uniform liquids shown on the plot, not every point produces a stable liquid. We can use Maxwell construction (illustrated for $K_2 = 1.0$) to determine the critical density ρ_c dividing the stable uniform liquid regime ($\rho_c < \rho < 1/2$) and the phase-separated regime ($\rho < \rho_c$), the

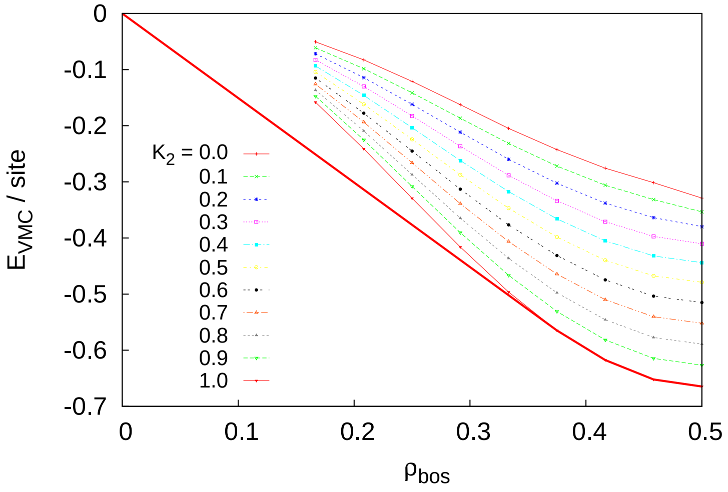

Figure 4.12: Trial energies of the optimized EBL wave function measured on a 24×24 lattice. Using Maxwell construction (illustrated for $K_2 = 1$), the critical density dividing the uniform liquid regime and the phase-separated regime can be determined for each K_2. We found a decrease in the critical density from 0.45 to 0.37 as K_2 increases from 0 to 1.

latter comprising a uniform liquid region and an empty region on the lattice. We found a decrease in the critical density ρ_c from approximately 0.45 to 0.37 as K_2 increases from 0 to 1.0. Thus, the additional K_2 ring terms indeed help to widen the stable regime of the uniform EBL phase in the K_1-K_2 model.

We should of course be cautious taking the VMC results too literally, given the described experience with the failures of the VMC at half-filling. However, we are probably in a better position here in that the "bare EBL stiffnesses" are such that both the wave function and the full theory are stable. Specifically, for $K_2 \geq 0.2$ and all densities $\rho < 1/2$, the optimal W is smaller than 3.5 and is further decreasing with increasing K_2. In the absence of Umklapps, the most important non-Umklapp has scaling dimension $8\sqrt{K/U} = 8/W > 2$ (see Appendix A3 of Ref. [3]); hence, all residual interactions are irrelevant and the full EBL theory is stable. While the VMC results are suggestive, the ultimate determination of the phase diagram requires unbiased approaches.

4.4.2 GFMC results for $L \leq 12$ lattices

Next, we discuss the results of our GFMC study on the 12×12 lattice for two selected points in parameter space, $K_2 = 0.5$ and 1.0. We consider densities varying from two

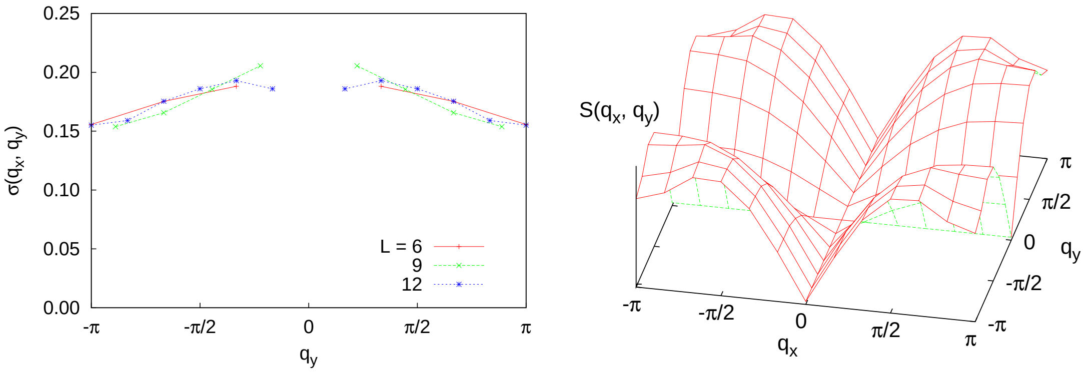

Figure 4.13: The GFMC density structure factor $S(q_x, q_y)$ on the 12×12 lattice at density $\rho = 1/3$ and $K_2 = 1.0$. Top: "Cross analysis" showing normalized slopes $\sigma(q_x = 2\pi/L, q_y)$, Eq. (4.10), versus q_y. Bottom: $S(q_x, q_y)$ in the full Brillouin zone. Besides the "cross" signature, notice also (weak) "$2k_F$ ridges" [here lines $(\pm 2\pi/3, q_y)$ and $(q_x, \pm 2\pi/3)$] which are typically present for all the uniform liquids observed at density less than half.

up to five bosons per row and per column (corresponding to densities $\rho = 1/6$ up to 5/12). For two and three bosons per row at $K_2 = 0.5$ and two bosons per row at $K_2 = 1.0$, we already see signatures of phase separation both in real space and momentum space. For higher boson number per row and per column, we do not see any sign of the phase separation. This allows us to conclude that the 12×12 system is in a stable uniform phase (i.e. without phase separation) for $1/3 \lesssim \rho < 1/2$.

To determine whether the uniform phase realizes the EBL, we examine the GFMC density and plaquette structure factors for any sign of instability to CDW or bond-solid ordering, but we do not observe any strong peak in $S(q_x, q_y)$ or $P(q_x, q_y)$. We apply the "cross analysis" of earlier sections to study the long-wavelength behavior of the density structure factor. The top panel of Fig. 4.13 shows the analysis done for $K_2 = 1.0$ and $\rho = 1/3$, which is carried out on $L \times L$ lattices with $L = 6$, 9 and 12. Note that the crude stability condition at generic densities is $\sigma \approx \kappa/2 = (1/2)\sqrt{K/U} > 1/8$ and is safely satisfied. Note also that the bare EBL stiffness on the scale $L = 6$ is similar here and in the half-filled system with the same K_2 shown in the middle panel in Fig. 4.9; however, unlike the half-filled case, it does not renormalize upon increasing L consistent with the picture where some relevant Umklapp becomes inoperative for $\rho < 1/2$. (One needs to worry about higher-order Umklapps if the density happens to be commensurate, which we do not worry here, having more in mind incommensurate densities in a window $1/3 \lesssim \rho < 1/2$. Density $\rho = 1/3$ may be slightly outside the

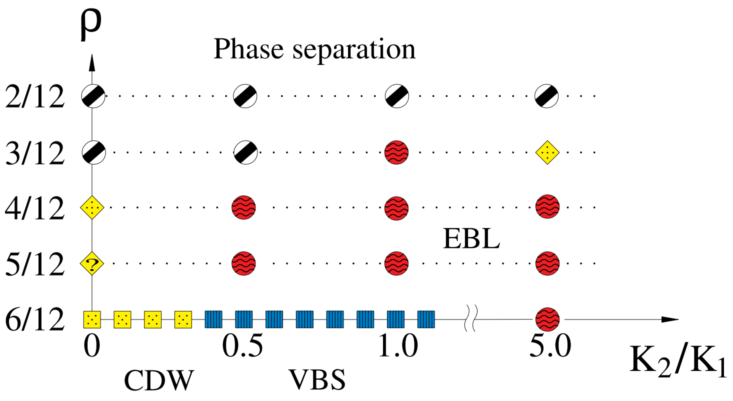

Figure 4.14: GFMC phase diagram for the K_1-K_2 model on the 12×12 lattice with varying boson density from two up to six bosons per row and per column.

stability window if we take the VMC energy per site estimates in Fig. 4.12 seriously and is perhaps stabilized here against phase separation by the finite system size, but is a good example allowing us to see the absence of flow of the EBL stiffness with several our sizes.) Similar result is obtained for $K_2 = 0.5$ (not shown), and both indicate that strong EBL signature is present. In the bottom panel of Fig. 4.13, the sharper "cross" shows that the EBL is more stable for density $\rho < 1/2$ compared to the half-filled system.

We also note the presence of small $2k_F$ ridges (discussed in Appendix A of Ref. [3]) which we typically observe in the GFMC density structure factor of uniform liquid ground states studied at densities away from half. This feature is predicted in the EBL theory and may be taken as additional evidence for identifying the uniform phase with EBL. Thus, our GFMC study for densities close to 1/2 shows that the intermediate K_2 regime is a stable EBL phase. Together with the VMC results, we think the evidences are sufficiently strong to conclude that the EBL phase is already realized in the K_1-K_2 model for densities $1/3 \lesssim \rho < 1/2$ and intermediate K_2 values, while the phase separation dominates at lower density.

Figure 4.14 shows the extended GFMC phase diagram which includes densities below 1/2 that we studied. We have also added points at $K_2 = 0$, where our similar study using the "cross" technique indicates that the EBL is unstable also close to half-filling (but we have not established the resulting phases). Thus, it has been crucial to add moderate K_2 exchanges to realize the EBL away from half-filling.

4.5 Summary and discussion

In summary, we studied the K_1-K_2 hard-core boson model with ring-only exchanges and found a transition at half-filling from a staggered CDW order at small K_2 to a columnar VBS order at intermediate K_2, and tantalizingly realizing the EBL phase at large K_2. For densities away from half-filling (but not too far), the EBL phase is more robust and our evidence strongly suggests that the EBL is already realized in this model for intermediate K_2. (Having some K_2 is helpful, since the pure K_1 model does not appear to have the EBL also away from half-filling.) For still lower densities, instability to phase separation is observed.

Although our sizes are significantly smaller than typically studied for more conventional phases with advanced techniques such as Stochastic Series Expansion, we already reach 12×12 systems which are much larger than sizes used in ED studies. Like the ED, the GFMC method that we use provides exact information about the ground state and allows us to reasonably establish the phase diagram of the proposed model already with our sizes. Our GFMC evidence of the EBL phase is quite suggestive at half filling, although we critically point out possible pitfalls. Specifically, while direct measurements of the charge- or bond-solid order parameters do not reveal any orders, the detailed comparison of the long-wavelength signature in the density structure factor with the available EBL theory suggests that our tentative EBL points at half-filling are very close to being unstable. (It may be helpful to modify the model still a bit like adding 2×2 ring exchanges to more reliably stabilize the EBL in the half-filled system.) On the other hand, similar comparison for the claimed EBL points away from half-filling indicates that they are safely away from instabilities.

We hope that it will be possible to study significantly larger sizes and confront our tentative EBL realizations as well as systematically confront the EBL theory. There are a number of further properties and questions that one would like to explore. Thus, we have measured only density and energy correlations that are diagonal in the number basis as they are simplest to implement in the GFMC. The gaplessness of the EBL and its "Excitonic" character can be probed directly by measuring boson "box" correlations like $G_\phi^{(4)}(x, y) \equiv \langle b^\dagger_{(0,0)} b_{(0,y)} b^\dagger_{(x,y)} b_{(x,0)} \rangle$. At fixed y, this can be viewed as an exciton propagator for excitons of size y, and is predicted to show power-law behavior $\sim |x|^{-\eta(y)}$ with calculable y-dependent exponent[18]. A crucial characterization of the EBL (which, in particular, determines all power law exponents) is the "EBL stiffness" function. While we have had some access to it via the cross analysis of the density structure factor, it would also be interesting to measure the EBL stiffness directly.

More broadly, the EBL is an example of a very gapless quantum liquid, and it can be challenging but fruitful learning grounds for how to handle such phases in Quantum Monte Carlo simulations.

One immediate question for the EBL theory is that in its present form it does not seem to anticipate the columnar VBS phase that we found numerically in the K_1-K_2 model. Another question for both numerical and theoretical studies is to understand phases away from half-filling near $K_2 = 0$, in the regime where we did not find the phase separation but also concluded that the EBL is not stable.

We also note that our present realizations of the EBL are very likely immediately unstable towards a superfluid if we allow unfrustrated boson hopping. This is based on our estimates of the EBL phase stiffnesses and understanding of the EBL stability conditions against boson hopping[18]. Thus, an EBL phase envisioned in Ref. [18] in such a broader sense [with no special conservation laws other than global U(1)] will not be realized with our K_1-K_2 model. However, we hope that our work will stimulate further studies to achieve such a phase.

Our tentative numerical realization of the EBL (even in the restricted sense of ring-only systems) is of broader interest in the search for so-called Bose-metal phases or more generally non-Fermi-liquid metals[93, 79, 94, 95, 96, 97, 98, 99, 100, 101, 102]. Despite many studies (including more recently of holographic metals in the High Energy Theory community[101, 102]), to date there is no example where such phases can be demonstrated controllably. The EBL can be viewed as a special kind of a Bose-metal and its theory is on more firm ground (an interesting perspective on the EBL is that it can be viewed as a solvable example of a parton-gauge theory where partons have flat Fermi surfaces in meanfield, cf. Sec. 2.2). It is hoped that the present work may trigger more refined studies of the EBL and confrontation with the theory, and more efforts to access the challenging but very interesting and topical Bose-metal phases.

Chapter 5

Failure of Gutzwiller wave function to capture gauge fluctuations

5.1 Introduction

Over the past decade, the study of spin liquids and non-Fermi liquids have been an active theme in condensed matter physics[93, 103]. A common approach used in many of these studies involves the notion of fractionalization where the original particles of a microscopic model are substituted with slave-particles coupled to a gauge field[104, 93]. It is often thought that Gutzwiller wave functions, constructed by performing projection into the physical Hilbert space, are able to capture the correct physics. However, it is suspected that such wave functions may be not sufficient to capture the long-wavelength properties in important cases with gapless gauge fields, e.g. for U(1) spin liquids, [93, 105, 106, 107, 108, 109, 110, 96, 111, 100, 112, 113] as the Gutzwiller construction does not include spatial gauge fluctuations[114, 115]. In a recent study of a hard-core boson model with pure ring exchange interactions which we proposed as a candidate model for realizing an Exciton Bose Liquid (EBL) phase[18, 45, 46], we noticed that the EBL can be viewed as a special solvable example of a gapless parton-gauge system[2, 3]. In this work, we shall take up this critical issue that Gutzwiller wave functions might not capture the spatial gauge fluctuations by explicit demonstrations in the EBL context.

To set the stage for our discussion, we begin with a schematic hard-core boson model with ring exchange interactions which serves the dual-purpose of introducing the EBL theory as well as motivating the wave functions used in this work. The

Hamiltonian defined on the square lattice is

$$\begin{aligned} H_{\rm ring} &= -\sum_{\mathbf{r},m,n} [K_{mn} P_{mn}(\mathbf{r}) + \text{H.c.}], && (5.1) \\ P_{mn}(\mathbf{r}) &= b^\dagger_{\mathbf{r}}\, b_{\mathbf{r}+m\hat{x}}\, b^\dagger_{\mathbf{r}+m\hat{x}+n\hat{y}}\, b_{\mathbf{r}+n\hat{y}}, && (5.2) \end{aligned}$$

where $P_{mn}(\mathbf{r})$ are extended ring exchanges on $m \times n$ plackets and K_{mn} are amplitudes for these exchanges. The Hamiltonian conserves boson number on each row and column, and throughout our Hilbert space is the sector with equal number of bosons on each row and column. We will assume $K_{mn} \geq 0$. Our recent study of a model with K_{11} and $K_{12} = K_{21}$ found regimes of the EBL phase[2, 3], while here we are not concerned with a detailed realization but rather qualitative aspects, assuming the model Eq. (5.1) is deep in the EBL phase.

In the following, we consider a slave-particle approach applied to this problem. Writing each boson operator as a product of two parton operators

$$b^\dagger_{\mathbf{r}} = b^\dagger_{\mathbf{r}1}\, b^\dagger_{\mathbf{r}2}, \tag{5.3}$$

we can recover the physical Hilbert space by imposing the constraint $n(\mathbf{r}) = n_1(\mathbf{r}) = n_2(\mathbf{r})$. We then consider states where the b_1 partons hop only in the $\hat{x}$ direction while b_2 partons hop only in the $\hat{y}$ direction[79] (so a single microscopic boson b indeed cannot hop by itself), and further justify this by noting that the mean-field expectation value of each ring term in Eq. (5.1) acquires a large, negative energy:

$$\begin{aligned} \langle -K_{mn} P_{mn}(\mathbf{r}) \rangle_{\rm m.f.} &= -K_{mn}\, |G_1(m\hat{x})|^2\, |G_2(n\hat{y})|^2 , && (5.4) \\ G_\mu(m\hat{\mu}) &\equiv \left\langle b^\dagger_{\mathbf{r}\mu} b_{\mathbf{r}+m\hat{\mu},\mu} \right\rangle_{\rm m.f.} . && (5.5) \end{aligned}$$

Beyond the mean-field slave-particle treatment, we introduce fluctuations into the theory by coupling the two parton species to a gauge field $\boldsymbol{a}$ residing on the links of the lattice, with opposite gauge charges for the respective species. The parton-gauge system is qualitatively captured by the following U(1) lattice gauge theory[79]:

$$\begin{aligned} H_{\rm U(1)} &= -t \sum_{\mathbf{r},\mu} \left[e^{i q_\mu a_{\mathbf{r}\mu}} b^\dagger_{\mathbf{r}\mu} b_{\mathbf{r}+\hat{\mu},\mu} + \text{H.c.} \right] && (5.6) \\ &+ h \sum_{\mathbf{r},\mu} e^2_{\mathbf{r}\mu} - K \sum_{\mathbf{r}} \cos(\nabla \times \boldsymbol{a})_{\mathbf{r}}, && (5.7) \\ (\nabla \cdot \mathbf{e})_{\mathbf{r}} &= \sum_{\mu} q_\mu b^\dagger_{\mathbf{r}\mu} b_{\mathbf{r}\mu} , && (5.8) \end{aligned}$$

where $q_\mu = \pm 1$ ($\mu = 1, 2$ or x, y) are the gauge charges for the partons moving respectively along $\hat{x}$ and $\hat{y}$ directions. Equations (5.6) and (5.7) are the respective Hamiltonians for the partons and the gauge fields, while Gauss' law in Eq. (5.8) imposes a constraint on the physical states. The lattice curl and divergence used in Eqs. (5.7) and (5.8) are defined by

$$\begin{aligned} (\nabla \times \boldsymbol{a})_{\mathbf{r}} &= a_{\mathbf{r}+\hat{x},y} - a_{\mathbf{r}y} - a_{\mathbf{r}+\hat{y},x} + a_{\mathbf{r}x} \ , \qquad (5.9) \\ (\nabla \cdot \mathbf{e})_{\mathbf{r}} &= e_{\mathbf{r}x} + e_{\mathbf{r}y} - e_{\mathbf{r}-\hat{x},x} - e_{\mathbf{r}-\hat{y},y} \ . \qquad (5.10) \end{aligned}$$

In the above U(1) gauge theory, the integer-valued "electric" field $e_{\mathbf{r}\mu}$ is canonically conjugate to the compact gauge field $a_{\mathbf{r}\mu}$ on the same lattice link. Dynamical fluctuation of these fields arises from the competing terms in the gauge field Hamiltonian. In the limit $h \gg K, t$, the electric field vanishes and the Gauss' law reduces to $n_1(\mathbf{r}) = n_2(\mathbf{r})$, which projects back into the physical boson Hilbert space. In this limit, it is possible to eliminate the gauge field perturbatively and obtain a Hamiltonian for hard-core bosons on the square lattice with ring exchange terms of the type in Eq (5.1), thus establishing formal connection between H_{ring} and $H_{\text{U(1)}}$[79].

As we will argue below, the EBL phase in H_{ring} corresponds to a "deconfined" phase of $H_{\text{U(1)}}$, where we can ignore the compactness of the gauge field, and treat the spatial gauge fluctuations fully. This is possible in the present case due to the powerful bosonization technique made applicable by the one-dimensional character of the partons and some "dimensional reduction" occuring in the system[18, 45, 46, 47, 48, 49]. On the other hand, a different route beyond mean-field often used in the literature is to apply Gutzwiller projection, mostly popular because of its numerical tractability[80, 116] (while gauge theories are often intractable). As one can anticipate, this state does not know about the spatial gauge field fluctuations and fails to reproduce the long-distance properties of the EBL phase.

The paper is organized as follows. In Sec. 5.2, we start from a Lagrangian formulation and show how the gauge theory leads to the EBL field theory, while neglecting the spatial gauge field fluctuations leads to a decidedly different low energy effective theory. In Sec. 5.3, we construct the wave functions used in this paper, and derive results for density structure factor and box correlator in the harmonic approximation for the wave functions. In Sec. 5.4, we present our accurate Variational Monte Carlo (VMC) calculations for hard-core bosons and show that the Gutzwiller wave function indeed realizes a quantum state that is distinct from the EBL. In the conclusion, we discuss our study more broadly.

5.2 Effective actions for the EBL and Gutzwiller theories

For the remainder of the paper, we assume a stable "deconfined" phase of $H_{\mathrm{U}(1)}$ where we can ignore compactness of the parton phase variables and compactness of the gauge field (stability is discussed in Appendices A,B of Ref. [79], borrowing from stability analyses of the EBL in Refs. [18, 45, 46]). To study the qualitative effects of spatial gauge fluctuations, we consider the following parton-gauge Lagrangian which provides a transparent starting point for our analysis:

$$\begin{aligned}\mathcal{L} &= \frac{v}{2\pi}\left[g^{-1}(\partial_x\theta_1)^2 + g(\partial_x\phi_1 - a_x)^2\right] + \frac{v}{2\pi}\left[g^{-1}(\partial_y\theta_2)^2 + g(\partial_y\phi_2 + a_y)^2\right] \\ &+ \frac{i}{\pi}(\partial_x\theta_1)(\partial_\tau\phi_1) + \frac{i}{\pi}(\partial_y\theta_2)(\partial_\tau\phi_2) + \frac{\kappa}{2}(\partial_x a_y - \partial_y a_x)^2, \end{aligned} \tag{5.11}$$

where the coarse-grained fields ϕ_μ and θ_μ provide a hydrodynamic fluid description of partons moving in the respective direction $\hat{\mu}$, and minimally coupled to the gauge field $\boldsymbol{a}$. The velocity v and dimensionless parameter g are convenient parametrization from the bosonization literature[50, 51, 117, 118]. In this formulation, ϕ_μ gives the phase of a parton while the dual variable θ_μ is related to the parton density fluctuation through $\delta n_\mu = \pi^{-1}\partial_\mu\theta_\mu$. We also assume a sizable "stiffness" κ for the gauge field (e.g., set by the energetics of the boson ring exchanges). Instead of introducing the temporal gauge field, we impose the following constraint at each lattice site:

$$\partial_x\theta_1 = \partial_y\theta_2, \tag{5.12}$$

which allows to recover the physical Hilbert space by binding two partons to give the original boson. The constraint is then solved by introducing a field ϑ satisfying

$$\theta_1 = \partial_y\vartheta, \quad \theta_2 = \partial_x\vartheta, \tag{5.13}$$

where, as the analysis below shows, ϑ can be identified as the coarse-grained field dual to the boson phase ϕ in the "bosonization" of the two-dimensional ring exchange model in Ref. [18].

We first integrate out the fields ϕ_μ and obtain

$$\begin{aligned}\mathcal{L}_{\text{eff}} &= \frac{v}{\pi g}(\partial_x\partial_y\vartheta)^2 + \frac{1}{2\pi v g}[(\partial_\tau\partial_x\vartheta)^2 + (\partial_\tau\partial_y\vartheta)^2] \\ &+ \frac{i}{\pi}(\partial_\tau\vartheta)(\partial_x a_y - \partial_y a_x) + \frac{\kappa}{2}(\partial_x a_y - \partial_y a_x)^2. \end{aligned} \tag{5.14}$$

After further integrating out the gauge field $\boldsymbol{a}$ and then dropping a less relevant term $(\partial_\tau \boldsymbol{\nabla}\vartheta)^2$, we arrive at the following realization of the EBL theory:

$$\mathcal{L}_{\mathrm{EBL}} = \frac{1}{2\pi^2\kappa}(\partial_\tau\vartheta)^2 + \frac{v}{\pi g}(\partial_x\partial_y\vartheta)^2, \tag{5.15}$$

where the more general EBL theory is defined by the action[18]

$$\mathcal{S}_{\mathrm{EBL}}[\vartheta] = \frac{1}{2}\sum_{\mathbf{k},\omega}\mathcal{M}_{\mathrm{EBL}}(\mathbf{k},\omega)\ |\vartheta(\mathbf{k},\omega)|^2, \tag{5.16}$$

$$\mathcal{M}_{\mathrm{EBL}}(\mathbf{0},\omega) \sim \omega^2, \quad \mathcal{M}_{\mathrm{EBL}}(\mathbf{k},0) \sim |k_x k_y|^2, \tag{5.17}$$

for small k_x, k_y. [Strictly speaking, going from Eq. (5.14) to Eq. (5.15), we need to keep $\mathcal{M}_{\mathrm{EBL}}(\mathbf{k},\omega)$ accurately on the full lines $\mathbf{k} = (0, k_y)$ and $(k_x, 0)$, i.e., we should not drop the naively less relevant term $(\partial_\tau \boldsymbol{\nabla}\vartheta)^2$. However, here we focus on long-wavelength effects originating near $\mathbf{k} = (0, 0)$ and work in a schematic continuum notation, while an accurate lattice variant can be found in Appendix B of Ref. [3]]. The energy dispersion can be obtained from Eq. (5.17) and has the form $E_{\mathbf{k}} \sim |k_x k_y|$. This is responsible for interesting properties of the EBL phase[18] such as specific heat $C \sim T\log(1/T)$, which makes it qualitatively different from sliding or cross-sliding Luttinger liquid phases[52, 53, 55]. [Generally, the vanishing of $E_{\mathbf{k}}$ along the lines $(0, k_y)$ and $(k_x, 0)$ can be shown to be a consequence of the conservation of boson number in each row and column of the lattice ring model, and is satisfied in this parton-gauge approach by construction.]

Let us now see what happens if we do not have dynamical gauge fields. To obtain the resulting Lagrangian, we drop the gauge field from Eq. (5.14):

$$\mathcal{L}_{\mathrm{Gutzw}} = \frac{v}{\pi g}(\partial_x\partial_y\vartheta)^2 + \frac{1}{2\pi v g}[(\partial_\tau\partial_x\vartheta)^2 + (\partial_\tau\partial_y\vartheta)^2]. \tag{5.18}$$

We will view this as a schematic model of what happens under Gutzwiller projection, hence the label "Gutzw." The corresponding action is

$$\begin{aligned} \mathcal{S}_{\mathrm{Gutzw}}[\vartheta] &= \frac{1}{2}\sum_{\mathbf{k},\omega}\mathcal{M}_{\mathrm{Gutzw}}(\mathbf{k},\omega)\ |\vartheta(\mathbf{k},\omega)|^2, && (5.19)\\ \mathcal{M}_{\mathrm{Gutzw}}(\mathbf{k},\omega) &= \frac{2v}{\pi g}|k_x k_y|^2 + \frac{1}{\pi v g}\omega^2\mathbf{k}^2. && (5.20) \end{aligned}$$

Here, the energy dispersion is $E_{\mathbf{k}} \sim |k_x k_y|/|\mathbf{k}|$ and the distinct behavior in the vicinity of $\mathbf{k} = 0$ leads to low energy properties different from the corresponding EBL properties. For example, the specific heat vanishes linearly with temperature for the Gutzwiller action, i.e., does not have the logarithmic factor $\log(1/T)$ found for the EBL case.

The long-wavelength properties of the EBL and Gutzwiller actions are also different. To give examples of other observable consequences, we calculate the density structure factor $D(\mathbf{k})$ and box correlator $\mathcal{B}(x,y)$ defined below:

$$\begin{aligned} D(\mathbf{k}) &\equiv \left\langle |n_{\mathbf{k}}|^2 \right\rangle, & (5.21)\\ \mathcal{B}(x,y) &\equiv \left\langle e^{i[\phi(0,0)-\phi(x,0)+\phi(x,y)-\phi(0,y)]} \right\rangle, & (5.22)\\ &= e^{-\frac{1}{2}\int \frac{d^2\mathbf{k}}{(2\pi)^2}|1-e^{ik_x x}|^2|1-e^{ik_y y}|^2 \langle|\phi_{\mathbf{k}}|^2\rangle}, & (5.23)\end{aligned}$$

with $\phi_{\mathbf{r}}$ denoting the boson phase variable, $b^\dagger_{\mathbf{r}} \sim e^{i\phi_{\mathbf{r}}}$. Here, $\langle|n_{\mathbf{k}}|^2\rangle$ can be evaluated for the Gaussian action using $\delta n_{\mathbf{r}} = \pi^{-1}\partial_x\partial_y\vartheta_{\mathbf{r}}$, and we obtain

$$\begin{aligned} D_{\rm EBL}(\mathbf{k}) &= \frac{1}{2}\sqrt{\frac{g\kappa}{2\pi\upsilon}}\,|k_x k_y|, & (5.24)\\ D_{\rm Gutzw}(\mathbf{k}) &= \frac{g}{2\sqrt{2}\pi}\,|k_x k_y|/|\mathbf{k}|, & (5.25)\end{aligned}$$

for small k_x, k_y. The singularity in the structure factor is distinct at $\mathbf{k} = \mathbf{0}$ for the two actions. Specifically, at fixed k_y, $D(k_x \to 0, k_y) = C(k_y)|k_x|$, with $C_{\rm EBL}(k_y) \sim |k_y|$ for small k_y, but $C_{\rm Gutzw}(k_y) \sim \text{const}$ for small k_y.

Since $n_{\mathbf{r}}$ and $\phi_{\mathbf{r}}$ are canonically conjugate to each other, they satisfy the following ground state minimum uncertainty relation

$$\sqrt{\langle|n_{\mathbf{k}}|^2\rangle}\sqrt{\langle|\phi_{\mathbf{k}}|^2\rangle} = 1/2, \tag{5.26}$$

which allows to obtain the box correlator Eq. (5.22). We will focus on the regime $|x| \gg |y|$, where we find power-law decay $\sim |x|^{-\eta(y)}$ with y-dependent exponents. To determine the exponents for all y, we in fact need to have details on the $(0, k_y)$ line all the way up to the Brillouin zone boundary [only the large y limit is determined by focusing on the vicinity of $\mathbf{k} = (0,0)$]. For illustrations below, we simply take model $D_{\rm EBL}(\mathbf{k})$ and $D_{\rm Gutzw}(\mathbf{k})$ by replacing $|k_y| \to 2|\sin(k_y/2)|$ in Eqs. (5.24) and (5.25).

For the EBL case we find[18]

$$\begin{aligned}
\mathcal{B}_{\mathrm{EBL}}(x,y) &\sim |x|^{-\eta_{\mathrm{EBL}}(y)}, && (5.27)\\
\eta_{\mathrm{EBL}}(y) &= \frac{1}{\pi^2}\sqrt{\frac{2\pi v}{g\kappa}}\int_0^{\pi}\frac{\sin^2(k_y y/2)}{\sin(k_y/2)}\,dk_y && (5.28)\\
&\approx \frac{1}{\pi^2}\sqrt{\frac{2\pi v}{g\kappa}}\log(y), && (5.29)
\end{aligned}$$

where the last line gives growth behavior for $|y| \gg 1$. For the Gutzwiller box correlator we find

$$\begin{aligned}
\mathcal{B}_{\mathrm{Gutzw}}(x,y) &\sim A(y)\ |x|^{-\eta_{\mathrm{Gutzw}}}, && (5.30)\\
\eta_{\mathrm{Gutzw}} &= \sqrt{2}/g\ , && (5.31)
\end{aligned}$$

which is independent of y in the present Gutzwiller model and generally remains finite for any y.

For finite y and large x, $\mathcal{B}(x,y)$ can be viewed as the propagator for an exciton of transverse size y. The qualitative difference in the box correlator for large transverse size shows that the two actions indeed lead to different long-wavelength properties. Thus, whether or not one allows gauge fluctuation does lead to effective low energy theories with distinct ground state properties.

We emphasize here that the stability of the EBL phase in the ring model given in Eq. (5.1) is not the focus of this study. Instead, we take the parton-gauge action in Eq. (5.11) as our starting point and address the question of whether excluding gauge fluctuation may lead to a qualitative difference. Note that the Gutzwiller action is only a caricature of what happens under the Gutzwiller projection and one should use some effective parameter g_{eff} rather than bare g. In the next section, we will give a more accurate treatment by explicitly constructing a Gutzwiller wave function and comparing its properties with those of a model EBL wave function.

5.3 Trial wave functions

In this section, we examine the formal properties of the Gutzwiller and EBL wave functions and highlight qualitative differences between them.

5.3.1 General Jastrow wave function and harmonic approximation

We first derive expressions for the density structure factor and box correlator for a general Jastrow-type wave function with a two-body pseudo-potential[119, 120]

$$\Psi\left(\{\mathbf{r}_i\}\right) \propto \exp\left[-\frac{1}{2}\sum_{i,j} u(\mathbf{r}_i - \mathbf{r}_j)\right], \tag{5.32}$$

where the indices i, j run over the bosons. In the second-quantized notation on the lattice, the wave function can be equivalently expressed as

$$|\Psi\rangle \propto \sum_{\{n_{\mathbf{r}}\}} \exp\left[-\frac{1}{2}\sum_{\mathbf{r}',\mathbf{r}''} u(\mathbf{r}' - \mathbf{r}'') n_{\mathbf{r}'} n_{\mathbf{r}''}\right] |\{n_{\mathbf{r}}\}\rangle\,. \tag{5.33}$$

We will shortly see that both the EBL and Gutzwiller wave functions have such forms, and their pseudo-potentials $u(\mathbf{r})$ will be given later. If we disregard the discreteness of the boson number here, we obtain the following approximate density structure factor[77] for an arbitrary Gaussian wave function (viewed in $n_{\mathbf{r}}$ variable)

$$\left\langle |n_{\mathbf{k}}|^2 \right\rangle = \frac{1}{2u_{\mathbf{k}}}, \tag{5.34}$$

$$u_{\mathbf{k}} = \sum_{\mathbf{r}} u(\mathbf{r}) e^{-i\mathbf{k}\cdot\mathbf{r}}. \tag{5.35}$$

The box correlator defined in Eq. (5.22) can be calculated using

$$\left\langle |\phi_{\mathbf{k}}|^2 \right\rangle = \frac{1}{2} u_{\mathbf{k}}, \tag{5.36}$$

which follows from the boson phase operator $\phi_{\mathbf{r}}$ being canonically conjugate to the boson number operator $n_{\mathbf{r}}$. Again, we have made use of the harmonic approximation, that is, we neglect the discreteness of $n_{\mathbf{r}}$, or equivalently the compactness of $\phi_{\mathbf{r}}$.

5.3.2 EBL wave function

For a model EBL wave function, we use the pseudo-potential from Refs. [79, 3], which can be motivated by a direct “spin-wave” treatment of the ring Hamiltonian in Eq. (5.1),

$$u_{\mathrm{EBL}}(\mathbf{r}) = \frac{1}{L^2}\sum_{\mathbf{k}} \frac{W_{\mathrm{EBL}}\; e^{i\mathbf{k}\cdot\mathbf{r}}}{4|\sin(k_x/2)\sin(k_y/2)|}. \tag{5.37}$$

Note that we exclude lines $(k_x, 0)$ and $(0, k_y)$ from the sum. One can also turn this into a convergent integral by replacing $e^{ik_x x}$ by $e^{ik_x x} - 1$ and $e^{ik_y y}$ by $e^{ik_y y} - 1$; this does not change Ψ_{EBL} because of fixed particle number in each row and column (in our working Hilbert space appropriate for the ring models). In principle, W_{EBL} can be a smooth function of $\mathbf{k}$ but for simplicity here, we take it to be a constant. We now use harmonic approximation and obtain the following density structure factor and box correlator

$$
\begin{aligned}
D_{\mathrm{EBL}}(\mathbf{k}) &= \frac{2}{W_{\mathrm{EBL}}} \left| \sin\left(\frac{k_x}{2}\right) \sin\left(\frac{k_y}{2}\right) \right|, && (5.38) \\
\mathcal{B}_{\mathrm{EBL}}(x, y) &\sim |x|^{-\eta_{\mathrm{EBL}}(y)}, && (5.39)
\end{aligned}
$$

where Eq. (5.39) holds for large x and fixed y and $\eta_{\mathrm{EBL}}(y)$ is given by

$$
\begin{aligned}
\eta_{\mathrm{EBL}}(y) &= \frac{W_{\mathrm{EBL}}}{\pi^2} \int_0^{\pi} \frac{\sin^2(k_y y/2)}{\sin(k_y/2)}\, dk_y && (5.40) \\
&= \frac{2W_{\mathrm{EBL}}}{\pi^2} \left[1 + \frac{1}{3} + \frac{1}{5} + \cdots + \frac{1}{2y-1} \right] && (5.41) \\
&\approx \frac{W_{\mathrm{EBL}}}{\pi^2} \log(y), \quad y \gg 1. && (5.42)
\end{aligned}
$$

Properties Eq. (5.38) with $D_{\mathrm{EBL}}(\mathbf{k}) \sim |k_x k_y|$ and Eq. (5.39) with $\eta_{\mathrm{EBL}}(y)$ growing logarithmically with y are long-wavelength properties of the EBL[18].

5.3.3 Gutzwiller wave function

To obtain the Gutzwiller wave function, we use the following wave function for partons confined within a chain

$$
\begin{aligned}
\Psi_{\mathrm{chain}}\left(\{x_i\}\right) &\propto \exp\left[-\frac{1}{2} \sum_{i,j} u_{1\mathrm{d}}(x_i - x_j) \right], && (5.43) \\
u_{1\mathrm{d}}(x) &= \frac{1}{L} \sum_{k_x} \frac{W_{1\mathrm{d}}\, e^{ik_x x}}{2|\sin(k_x/2)|}. && (5.44)
\end{aligned}
$$

(We can again regularize the sum by replacing $e^{ik_x x}$ by $e^{ik_x x} - 1$ since adding a constant to the pseudo-potential does not change the wave function for fixed particle number in the chain.) This trial wave function has been known to capture the energetics as well as Luttinger liquid exponents of one-dimensional systems[121, 122]. We construct the

Gutzwiller wave function as

$$\Psi_{\text{Gutzw}}(\{\mathbf{r}_i\}) = \Psi_1(\{\mathbf{r}_i\})\ \Psi_2(\{\mathbf{r}_i\})\ , \tag{5.45}$$

where Ψ_μ is the wave function for the b_μ partons confined to move within chains oriented in the $\hat{\mu}$ direction. Note that Gutzwiller projection has been explicitly imposed in Eq. (5.45) where both parton species are present at each boson location for any given set of $\{\mathbf{r}_i\}$. The Gutzwiller wave function indeed has a Jastrow form with the following pseudo-potential:

$$u_{\text{Gutzw}}(\mathbf{r}-\mathbf{r}') = \delta_{y,y'}\ u_{\text{1d}}(x-x') + \delta_{x,x'}\ u_{\text{1d}}(y-y'). \tag{5.46}$$

Again disregarding the discreteness of the boson numbers, we obtain the following density structure factor:

$$D_{\text{Gutzw}}(\mathbf{k}) = \frac{1}{W_{\text{1d}}} \frac{|\sin(k_x/2)\sin(k_y/2)|}{|\sin(k_x/2)| + |\sin(k_y/2)|}\ . \tag{5.47}$$

This has a different singularity at $\mathbf{k} = \mathbf{0}$ compared to the density structure factor for the EBL wave function in Eq. (5.38)[123].

The difference in the structure factors near $\mathbf{k} = \mathbf{0}$ manifests itself in the fluctuation properties. For a rectangular region $[0, x) \times [0, y)$, we define the following number fluctuation for the total number of bosons in the region

$$\delta N(x,y) = \sum_{x'=0}^{x-1}\sum_{y'=0}^{y-1} \delta n(x', y')\ . \tag{5.48}$$

The variance of the number fluctuation is readily calculated

$$\langle \delta N(x,y)^2 \rangle = \frac{1}{L^2}\sum_{\mathbf{k}} \left[\frac{\sin(k_x x/2)\sin(k_y y/2)}{\sin(k_x/2)\sin(k_y/2)}\right]^2 \langle |n_{\mathbf{k}}|^2 \rangle\ .$$

In the limit $x \gg y \gg 1$, this has different asymptotic forms for the EBL and the Gutzwiller wave functions:

$$\left\langle \delta N_{\text{EBL}}(x,y)^2 \right\rangle \approx \frac{2}{\pi^2 W_{\text{EBL}}} \log(x)\ \log(y), \tag{5.49}$$

$$\left\langle \delta N_{\text{Gutzw}}(x,y)^2 \right\rangle \approx \frac{1}{\pi W_{1d}}\, y\ \log(x). \tag{5.50}$$

Equation (5.49) shows that such number fluctuation in the EBL wave function is strongly suppressed. On the other hand, it scales linearly in the region width y for the Gutzwiller case while increasing logarithmically with x. This reminds us of the additivity of variances of statistically independent random variables, and the Gutzwiller result appears to suggest that, in the absence of gauge fluctuations, the bosons in adjacent chains are weakly coupled compared to those in the EBL phase.

We now turn to the box correlator and obtain

$$\mathcal{B}_{\rm Gutzw}(x,y) \sim |x|^{-W_{\rm 1d}/\pi}, \tag{5.51}$$

for large x and finite y, which is again qualitatively different from the EBL box correlator in that the exponent here does not grow with y. Notice that the Gutzwiller result has in fact identical power-law to the mean-field box correlator [see Eq. (5.5)]

$$\begin{aligned} \mathcal{B}_{\rm m.f.}(x,y) &= |G_1(x\hat{x})|^2\ |G_2(y\hat{y})|^2, & (5.52)\\ &\sim |x|^{-W_{\rm 1d}/\pi}\ |y|^{-W_{\rm 1d}/\pi}. & (5.53)\end{aligned}$$

This therefore suggests that the Gutzwiller projection has not provided any improvement over the mean-field slave-particle treatment as far as long-distance properties are concerned. [Note that the schematic treatment in Sec. 5.2 leading to results Eqs. (5.25) and (5.31) might suggest otherwise if we naively use $g = g_{\rm m.f.} = \pi/W_{1d}$ there; however, such treatment appears to over emphasize the role of the constraint on the long-distance properties of the wave functions and we should allow some effective $g_{\rm eff}$ instead. We believe the direct approach to the wave functions as in this section is more accurate and shows that there is no change in the power-laws compared to the mean-field.]

To conclude our harmonic approximation study of the EBL and the Gutzwiller wave functions in this section, we have shown that despite the ability of the Gutzwiller wave function to realize a quantum liquid, it does not give a fully qualitatively accurate representation of the EBL phase as defined by Eqs. (5.16) and (5.17). In the next section, we enforce hard-core boson condition at each lattice site in Variational Monte Carlo calculations and obtain numerically exact information for the corresponding wave functions, defined in sectors with fixed boson number in each row and column.

5.4 Exact VMC results

In this section, we perform exact calculations for the hard-core bosons using the wave functions from Sec. 5.3. We set up Variational Monte Carlo simulations which allow hard-core boson constraint to be imposed exactly. We also require fixed boson number in each row and column. Since we are only interested in wave functions which realize liquid phases, it is important to ensure that the variational parameter chosen for each trial wave function does not lead to an ordered phase. For concreteness, we choose density with $\rho = 1/2$ (i.e., $L/2$ bosons in each row and each column of $L \times L$ lattices), and select $W_{\rm EBL} = 1.5$ for the EBL wave function and $W_{\rm 1d} = 1.5$ for the Gutzwiller wave function so that both wave functions are deep inside the liquid regimes[124]. For the Monte Carlo random walks, we allow all possible $m \times n$ ring moves where bosons hop from occupied sites at $\mathbf{r}$ and $\mathbf{r} + m\hat{\mathbf{x}} + n\hat{\mathbf{y}}$ onto vacant sites at $\mathbf{r} + m\hat{\mathbf{x}}$ and $\mathbf{r} + n\hat{\mathbf{y}}$. These are the simplest moves that preserve the boson number in each row and column and also guarantee ergodicity in the Hilbert space of the problem.

We now present the results of our numerical study. In Fig. 5.1, we analyze the density structure factor for each of the two wave functions by plotting

$$C(k_y) = \left. \frac{D(k_x, k_y)}{\sin(k_x/2)} \right|_{k_x = 2\pi/L}, \qquad (5.54)$$

taken at the smallest $k_x = 2\pi/L$. This gives a finite-size measure of the slope of the density structure factor characterizing the V-shaped singularity in the small k_x limit at fixed k_y, and we are further interested in the behavior of $C(k_y)$ for small k_y. In the top panel, we obtain the limiting behavior for the EBL wave function $C_{\rm EBL}(k_y \to 0) \approx |k_y|/W_{\rm EBL}$, which agrees very well with the results derived using the harmonic approximation in Eq. (5.38) (illustrated as a broken line in the figure).

The bottom panel of Fig. 5.1 shows the corresponding analysis of the density structure factor for the Gutzwiller wave function. Here, $C_{\rm Gutzw}(k_y)$ approaches constant $1/W_{\rm Gutzw}$ (horizontal broken line) for any finite k_y when lattice size $L \to \infty$, which again is in line with the result in the harmonic approximation in Eq. (5.47). We also examine the ratio of the VMC Gutzwiller density structure factor to that in the harmonic approximation (not shown), and verify that the VMC data indeed converges toward the analytical trend in Eq. (5.47) with increasing L. Thus, the density structure factor at long wavelengths clearly has a qualitatively different behavior for the EBL and Gutzwiller hard-core boson wave functions.

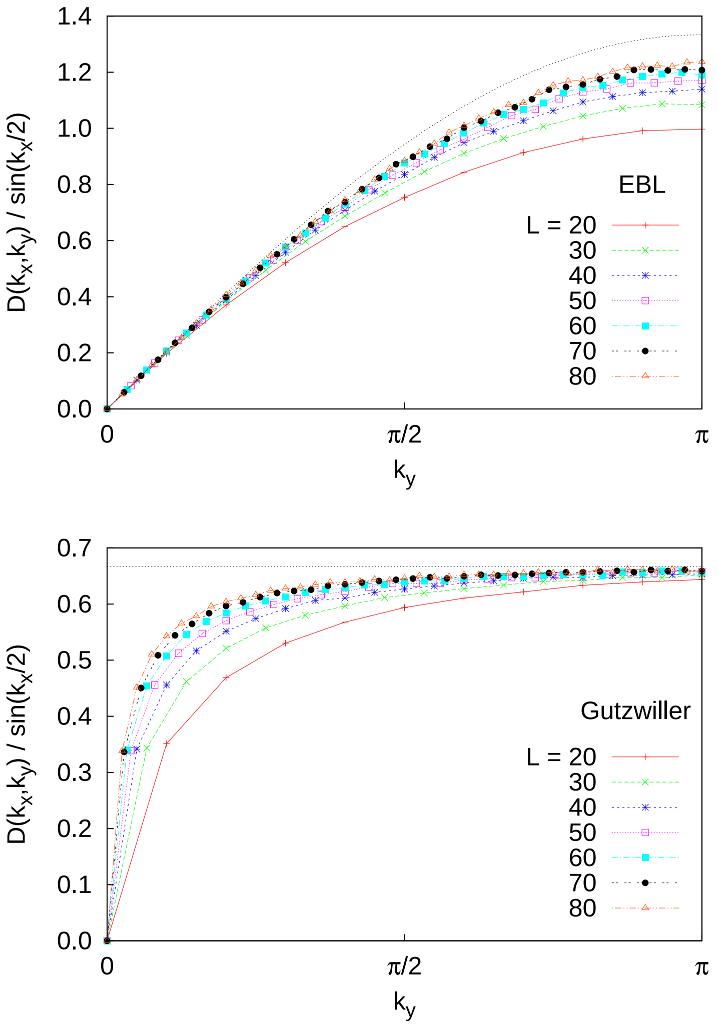

Figure 5.1: Analysis of the VMC density structure factors at long wavelengths for the hard-core boson wave functions. We plot $C(k_y) = D(k_x, k_y)/|\sin(k_x/2)|$ evaluated at the smallest $k_x = 2\pi/L$ versus k_y for system sizes from $L = 20$ to 80. Top: The EBL result shows $C(k_y)$ approaching $|k_y|/W_{\rm EBL}$ for small k_y. Bottom: The Gutzwiller result shows $C(k_y)$ approaching the constant $1/W_{\rm Gutzw}$ for any fixed $k_y \neq 0$ upon increasing L. The broken lines show the results obtained using harmonic approximations in the $L \to \infty$ limit.

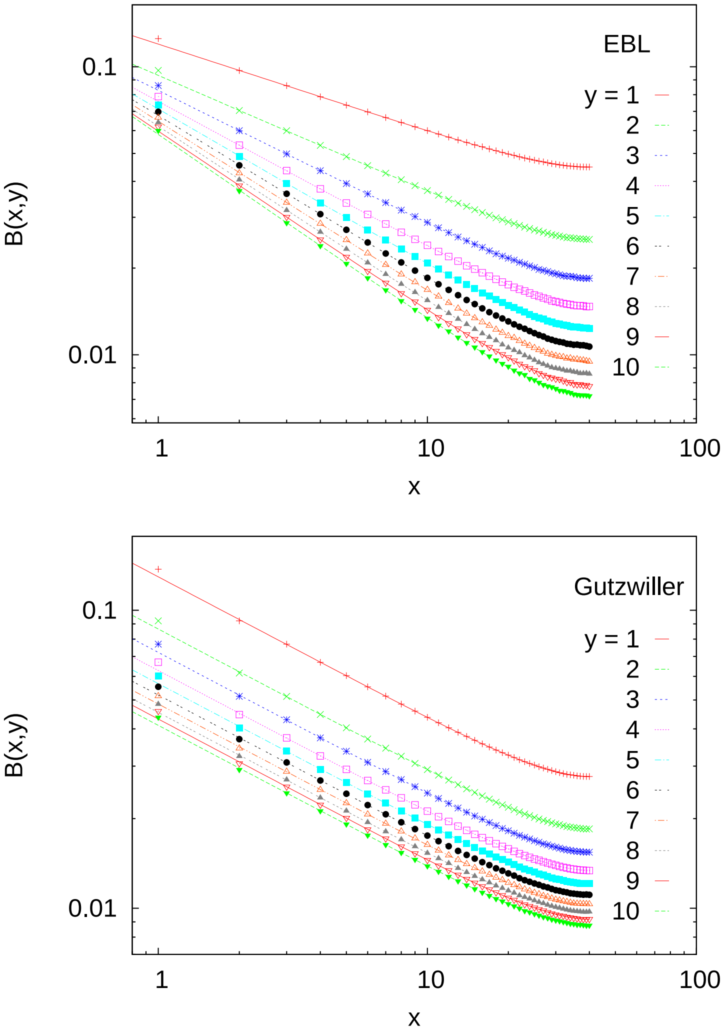

Figure 5.2: Box correlator $\mathcal{B}(x, y)$ versus x for $y = 1$ to 10, measured on a 80×80 lattice. The data is fitted to the ansatz in Eq. (5.55), and the results show that the power-law exponent $\eta(y)$ increases logarithmically with y for the EBL wave function (top), while the exponent is essentially independent of y for the Gutzwiller wave function (bottom).

Figure 5.2 shows the box correlator $\mathcal{B}(x, y)$ versus x for $y = 1$ to 10, measured on a 80×80 lattice. The results for the EBL and Gutzwiller wave functions are given in the top and bottom panels, respectively. The data points are plotted together with the best-fit curves using the following ansatz:

$$\begin{aligned} \mathcal{B}(x, y) &= A_y \left| \frac{L}{\pi} \sin\left(\frac{\pi x}{L}\right) \right|^{-\eta(y)}, \qquad (5.55) \\ &\approx A_y |x|^{-\eta(y)}, \quad x \ll L. \qquad (5.56) \end{aligned}$$

From the two plots shown in Fig. 5.2, it is clear that Eq. (5.55) provides very good fits for the data. For fixed y, the parameter $\eta(y)$ determines the exponent in the power-law relation $\mathcal{B}(x, y) \sim |x|^{-\eta(y)}$.

For the EBL wave function, the lines fanning out in the top panel show that the fitting parameter $\eta(y)$ increases with y. Anticipating a logarithmic relation from Eq. (5.42), we perform an additional data fit to the following:

$$\eta(y) = \gamma \log(y), \qquad (5.57)$$

and obtain $\gamma = 0.148$. This value is very close to W_{EBL}/π^2 from the harmonic approximation, and therefore suggests that the discreteness of the boson number and the hard-core repulsion in the wave function do not significantly alter the long-wavelength properties of the resulting quantum state when the wave function is well inside the liquid regime.

For the Gutzwiller wave function, the lines running parallel to one another in the bottom panel in Fig. 5.2 show that the exponent of the box correlator is essentially independent of y. We obtain very good fits using $\eta(y) = 0.477$, which is again very close to the corresponding Gaussian value $W_{1\mathrm{d}}/\pi$. As before, the discreteness of the boson number and the hard-core repulsion do not modify the long-wavelength results of the harmonic approximation.

We have thus shown that the EBL and Gutzwiller results obtained using the harmonic approximations in Sec. 5.3 remain valid for hard-core bosons here when the wave functions are well inside the liquid regimes. But more importantly, the exact VMC density structure factor and box correlator show that the Gutzwiller projection leads to a quantum state that is qualitatively different from that of the EBL wave function. We discuss further implications of this finding in the conclusion.

5.5 Summary and discussion

In this work, we compared a Gutzwiller wave function with an EBL wave function, both motivated from the same parton-gauge action, and found that they realize quantum liquids with qualitatively different long-wavelength properties. This shows that the Gutzwiller wave function, which does not include fluctuations of the spatial gauge field, has failed to capture the long-wavelength physics. Similar approaches have often been used in the studies of quantum spin liquids and other strongly correlated systems, and in some cases, Gutzwiller wave functions with gapless partons possess competitive ground state energies[114, 15, 115, 16, 125, 79, 97, 126, 127, 128]. We note that the gauge fluctuations in our case are more damped compared to the cases with generic parton Fermi surfaces[93, 105, 106, 107, 108, 109, 110, 96, 111, 100] or Fermi points[93, 112, 113], and hence are expected to be less important than in those cases, but still lead to qualitative effects as we have seen. This therefore raises the possibility that Gutzwiller projection may generally fail to capture the correct ground state physics.

Let us also mention some extensions. An interesting question in the same setting is to compare entanglement in the Gutzwiller and EBL wave functions[129, 130], and examine the effect of including spatial gauge fluctuations as modeled by the latter. A direct study both in the EBL field theory and in the hard-core boson model realizations[2, 3] would be useful.

In this paper, we used bosonic partons, which we argued to be appropriate for the ring models with $K_{mn} > 0$; in this case the ground state wave function is positive and there is no sign problem. On the other hand, for models with $K_{mn} < 0$, where in general there is a sign problem and the ground state wave function has non-trivial signs, it appears to be more appropriate to use fermionic partons, $b^\dagger_{\mathbf{r}} = d^\dagger_{\mathbf{r}1} d^\dagger_{\mathbf{r}2}$[79]. We can argue for this either from mean-field energetics like in Eq. (5.4), or from the connection between the corresponding H_{ring} and $H_{\text{U(1)}}$[79]. This construction gives a so-called extremal DLBL state from Ref. [79] where fermionic partons form flat Fermi surfaces in the mean-field. A naive bosonization treatment of the corresponding parton-gauge system leads to theory similar to our Eq. (5.11), and hence to an EBL-like long-wavelength description. The Gutzwiller wave function $\Psi_b = \Psi_{d_1} \Psi_{d_2}$ is also similar to the one in the present study, but with specific sign structure from the product of the parton Slater determinants. Inspired by the present work, we can attempt to crudely account for the gauge fluctuations by replacing the absolute value $|\Psi_{d_1} \Psi_{d_2}|$ by the Jastrow-EBL form while keeping the sign structure. Interestingly, while the density correlations are not sensitive to the sign structure, the boson ring correlations are, and in the frustrated case they have faster power-law decay (for the same density correlations), as can be seen already on the mean-field level.

It would be interesting to examine other contexts with gapless parton-gauge systems where Gutzwiller-type wave functions have been used, such as gapless spin liquids[93, 114, 115, 16, 126, 128, 125] and more general Bose-metals[79, 97, 127], and see if we can learn how to include gauge fluctuations in these cases, even if only on some crude level.

Chapter 6

Schwinger boson spin liquids on Kagome lattice

6.1 Introduction

The Heisenberg antiferromagnet on the kagome lattice has long been anticipated to realize a spin liquid. Recently, Herbertsmithite $ZnCu_3(OH)_6Cl_2$[30], which contains kagome layers of spin-1/2 moments, has emerged as an experimental candidate with no sign of any ordering down to 50 mK. However, analysis of this material is complicated by the presence of impurities and residual interactions such as Dzyaloshinski-Moriya interaction and spin anisotropy[131]. Interest in spin liquids on the kagome lattice has been re-ignited by recent numerics[24, 25, 29, 132], where Density Matrix Renormalization Group (DMRG) studies find a spin-disordered ground state with a small gap for the nearest-neighbor antiferromagnet[29]. Preliminary DMRG data suggests that the gap increases in the presence of second-neighbor J_2 coupling[133], corroborating an earlier Exact Diagonalization (ED) study[25]. A vast review of earlier literature is revisited in Ref. [29].

In an early study of the nearest-neighbor Heisenberg model using large-N treatment of Schwinger boson slave particles[40], Sachdev found that condensation of spinons gives rise to magnetically ordered ground states for spin $S > 0.26$. A subsequent variational study by Sindzingre *et al.* using Resonating Valence Bond (RVB) wave functions interpolating between spin liquids and magnetically ordered states instead found that the former have lower energies[134]. However, the spin correlations beyond first neighbors do not agree well with ED results[134, 27]. More recently, the trial energy of the projected Dirac spin liquid constructed using fermionic slave particle approach was found to lie very close to the ED ground state energy in the nearest-neighbor Heisenberg model[41, 42], and a recent study extended this to the

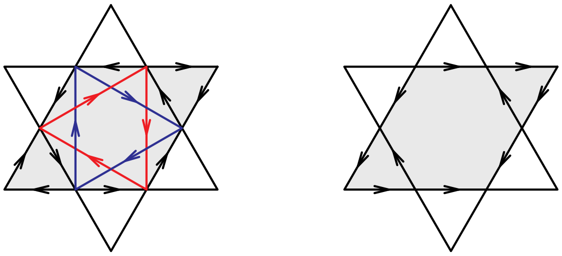

(a) $q = 0$ SL (b) $\sqrt{3} \times \sqrt{3}$ SL

Figure 6.1: The SB ansatze $\{A_{ij}\}$ from Ref. [40]. The unit cell is shaded for each ansatz. All equidistant A_{ij} have identical magnitudes, and A_{ij} is positive if an arrow points from site i to j. For the $\mathbf{q} = \mathbf{0}$ ansatz, we extend A_{ij} to include second-neighbor pairing. The $\sqrt{3} \times \sqrt{3}$ ansatz has poorer energy for $J_2 > 0$.

presence of second-neighbor coupling J_2[44]. However, the observation of an energy gap in the DMRG and ED studies suggests that the gapless Dirac spin liquid may lose some ground in the presence of second-neighbor coupling[25, 133].

6.2 Schwinger-boson mean field ansatze

To investigate the performance of Schwinger-boson wave functions in the presence of second-neighbor coupling, we study the energetics of a class of projected Schwinger boson wave functions in the J_1–J_2 Heisenberg model given by following Hamiltonian:

$$H = J_1 \sum_{\langle i,j \rangle} \mathbf{S}_i \cdot \mathbf{S}_j + J_2 \sum_{\langle\langle i,j \rangle\rangle} \mathbf{S}_i \cdot \mathbf{S}_j, \tag{6.1}$$

where $\langle i, j \rangle$ and $\langle\langle i, j \rangle\rangle$ denotes first- and second-neighbor pairs (separated by distances 1 and $\sqrt{3}$), respectively. We set $J_1 = 1$ as the unit for energy and consider only antiferromagnetic second-neighbor coupling with $J_2 \geq 0$. The Schwinger-boson representation of a spin $\mathbf{S}$ is given by

$$\mathbf{S} = \frac{1}{2} \sum_{\alpha,\beta} b^\dagger_\alpha \boldsymbol{\sigma}_{\alpha\beta} b_\beta, \quad \kappa = \sum_\alpha b^\dagger_\alpha b_\alpha = 2S, \tag{6.2}$$

where b_α is a bosonic operator, $\boldsymbol{\sigma}$ are Pauli matrices, and κ is the number of bosons per site. The Hamiltonian becomes quartic in the bosonic operators, and upon mean-field decoupling (cf. Sec. 2.3), we obtain the following:

$$\begin{aligned}\hat{H}_{\text{m.f.}} &= \frac{1}{2}\sum_{i,j}\left(A_{ij}b^{\dagger}_{i\downarrow}b^{\dagger}_{j\uparrow}+\text{H.c.}\right)+\sum_{i,j}\frac{|A_{ij}|^2}{2J_{ij}} \\ &- \mu\sum_{i}\left(\sum_{\sigma}b^{\dagger}_{i\sigma}b_{i\sigma}-\kappa\right), \qquad (6.3)\\ A_{ij} &= \frac{1}{2}J_{ij}\sum_{\sigma,\sigma'}\epsilon_{\sigma\sigma'}\langle b_{i\sigma}b_{j\sigma'}\rangle, \quad \kappa=\sum_{\sigma}\langle b^{\dagger}_{i\sigma}b_{i\sigma}\rangle. \qquad (6.4)\end{aligned}$$

We treat the "pairing amplitudes" A_{ij} and "chemical potential" μ as variational parameters. Equations (6.4) are self-consistency relations in the mean-field. Figure 6.1 shows Sachdev's ansatze for A_{ij} which have good mean-field energies in the $J_2 = 0$ model[40]. The nearest-neighbor A_{ij} are real, and their signs are positive if an arrow points from site i to j. Following Sindzingre *et al.*[134], we label these ansatze as $q = 0$ and $\sqrt{3}\times\sqrt{3}$, which correspond to Sachdev's $Q_1 = \pm Q_2$, respectively[40]. For the $q = 0$ ansatz shown in Fig. 6.1(a), we introduce an additional real parameter for the second-neighbor pairing, with the pattern of arrows going clockwise in triangular loops for both first and second neighbors. Similar second-neighbor A_{ij} for the $\sqrt{3}\times\sqrt{3}$ ansatz are forbidden by its projective symmetry group (PSG). In Ref. [57], Wang *et al.* found two more distinct ansatze for symmetric spin liquids, but they argued that the Heisenberg model energies of those spin liquids are expected to be considerably poorer. Our variational calculations confirm that this is indeed true.

6.3 Accessibility of Schwinger-boson spin liquid

We first present the results of a crude study on the accessibility of Schwinger boson spin liquids at the mean-field level, by computing the critical boson density

$$\kappa_c = -1 + \lim_{\mu\to\mu_{\max}}\frac{1}{N}\sum_{\alpha=1}^{N}\frac{|\mu|}{\sqrt{\mu^2-\lambda_\alpha^2}}, \qquad (6.5)$$

where $\{\lambda_\alpha\}$ are eigenvalues of the matrix $-iA$ (cf. Eq. 6.6 below), $\mu_{\max} = -\max\{|\lambda_\alpha|\}$, and N is the number of sites on the lattice. Below κ_c, the mean-field excitation spectrum is gapped and gives rise to a stable spin liquid. For $\kappa \geq \kappa_c$, the gap closes and magnetic ordering results from spinon condensation. With only nearest-neighbor A_{ij}, $\kappa_c \approx 0.5$ and 0.54 for the $q = 0$ and $\sqrt{3}\times\sqrt{3}$ ansatze, respectively[57]. In analogy to Wang's analysis for the honeycomb lattice[136], we plot the critical boson density κ_c

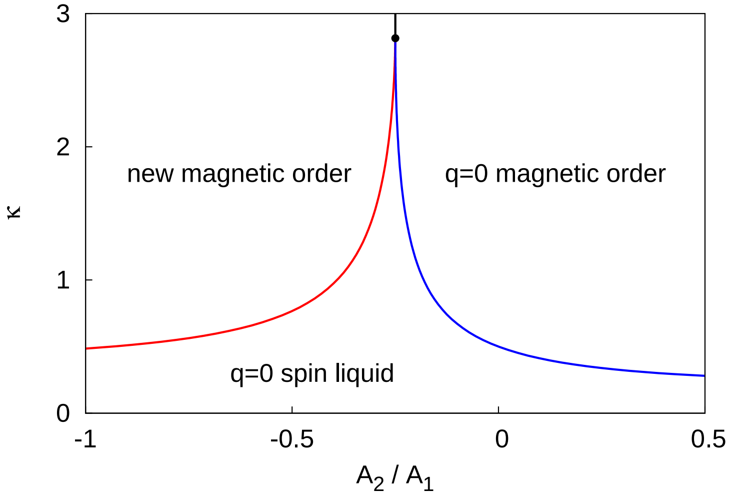

Figure 6.2: mean-field “phase diagram” for the $\mathbf{q} = \mathbf{0}$ SB ansatz[135]. The phase boundary separates spin liquid from the magnetically ordered phases. A spin liquid regime is present for physical spin-1/2 systems with κ=1. The new magnetic order is complex and is not relevant for this paper.

versus A_2/A_1 for the $q = 0$ ansatz, where A_1 and A_2 are the amplitudes of first- and second-neighbor A_{ij}, in Fig. 6.2. We note that the second-neighbor A_{ij} has opened up a disordered regime in the parameter range $-0.4 < A_2/A_1 < -0.18$ relevant for $S = 1/2$.

6.4 Variational Monte Carlo study

We now turn to a variational Monte Carlo study of the J_1–J_2 model on the symmetric 36-site cluster used in previous numerical studies[27, 134], which allows a direct comparison with ED energies as well as the energies of the Dirac spin liquid and magnetically ordered states. We construct projected wave functions for the Schwinger boson spin liquids as follows. Writing the anti-symmetric matrix A (see Eq. 6.4) as

$$A = iM\Lambda M^{\dagger}, \tag{6.6}$$

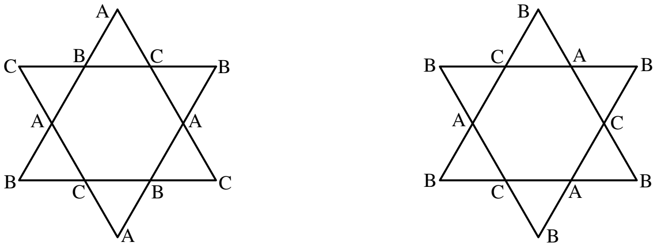

(a) $q = 0$ MO (b) $\sqrt{3} \times \sqrt{3}$ MO

Figure 6.3: Magnetic orderings (MO) which arise from spinon condensation in $\mathbf{q} = \mathbf{0}$ and $\sqrt{3}\times\sqrt{3}$ SB ansatze. A, B, and C are the 120° antiferromagnetic spin orientations. For $J_2 > 0$, the $\sqrt{3} \times \sqrt{3}$ MO has poorer energy than the $\mathbf{q} = \mathbf{0}$ MO.

where Λ is diagonal and M is unitary, we solve the mean-field Hamiltonian using Bogoliubov's transformation and obtain the following trial wave function

$$|\Psi_{\mathrm{SB}}\rangle = \hat{\mathcal{P}}_G \ \exp\left\{\sum_{j,k} u_{jk} \ \hat{b}^\dagger_{j\uparrow}\hat{b}^\dagger_{k\downarrow}\right\}|0\rangle, \tag{6.7}$$

$$u_{jk} = i\sum_{\alpha}\frac{M_{j\alpha}\lambda_\alpha(M^\dagger)_{\alpha k}}{-\mu+\sqrt{\mu^2-\lambda_\alpha^2}}. \tag{6.8}$$

The Gutzwiller operator $\hat{\mathcal{P}}_G$ enforces the constraint $\kappa = 1$ at every site. Although the latter boson density may not be accessible to a given ansatz and μ at the mean-field level (see Fig. 6.2), the projected wave function is nevertheless physically valid. However, it should be noted that extrapolating a wave function beyond the regime of applicability of its original motivation may instead realize a different quantum state.

In our variational Monte Carlo simulation, the amplitude of each sampled spin configuration is given by the permanent of the $N/2 \times N/2$ matrix $\{u_{jk}\}$, where j and k run over the spin-up and spin-down sites, respectively. We make use of Ryser-Nijenhuis-Wilf dense permanent algorithm to calculate the permanent[137]; in this way, the procedure does not have the sign problem encountered in the valence bond basis[134]. Despite a poor scaling $\sim 2^{N/2}$ with system size, it is manageable for sizes that are already interesting. For each ansatz, u_{jk} is exponentially decaying for $\mu < \mu_{\max}$, while decaying in a power-law $u_{jk} \sim |r_j - r_k|^{-p}$ at $\mu = \mu_{\max}$. The latter occurs when the mean-field excitation gap just closes and yields a critical state. When written in the valence bond basis, the projected wave function constructed from Schwinger boson slave particles realizes an RVB state.

We also consider magnetically ordered states shown in Fig. 6.3 which arise from

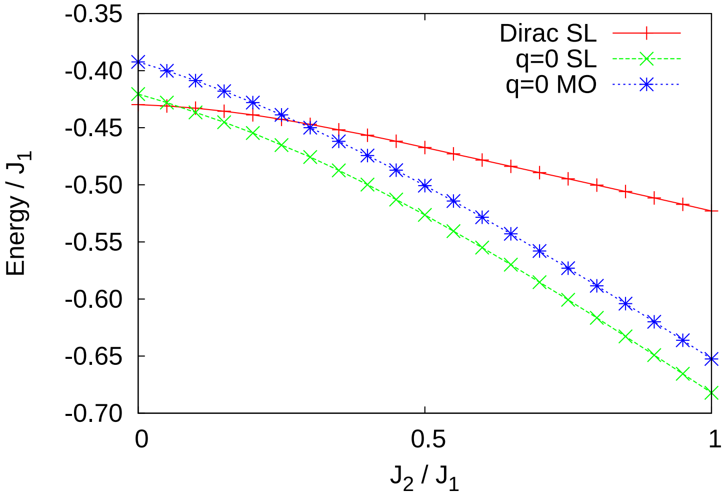

Figure 6.4: Comparison of trial energies per site for Dirac SL, $\mathbf{q}=\mathbf{0}$ SB wave function, and $\mathbf{q}=\mathbf{0}$ Jastrow-type magnetically ordered (MO) state. The SB state has poorer energy than Dirac SL for $J_2/J_1 \lesssim 0.08$, but performs better for larger J_2 and better than the Jastrow-type MO for all J_2.

the condensation of spinons in the respective ansatz[57]. For both orderings, their classical nearest-neighbor energies are identical, but the second-neighbor energy is clearly lower for the $q=0$ ordered state since it has antiferromagetic second-neighbor correlations while the $\sqrt{3}\times\sqrt{3}$ state has ferromagnetic correlations. It is therefore sufficient to consider only the $q=0$ ordering. For this state, we construct the following trial wave function:

$$\langle\{S_j^z\}|\Psi_{q=0}\rangle = \exp\left\{ i\sum_j \phi_j S_j^z - \sum_{ij} K_{ij} S_i^z S_j^z \right\}, \tag{6.9}$$

where $\phi_j = \{0, \pm 2\pi/3\}$ are the phase angles on the three sublattices, and K_{ij} are two-body pseudo-potentials for the Jastrow factor. We allow two variational parameters for the first- and second-neighbor pseudo-potentials, and two more for a power-law decay between further neighbors. We also consider a Huse-Elser type of three-site phase factor allowed by the symmetry of the classical wave function (see Ref. [14]), but this variational degree of freedom apparently does not improve the trial energy.

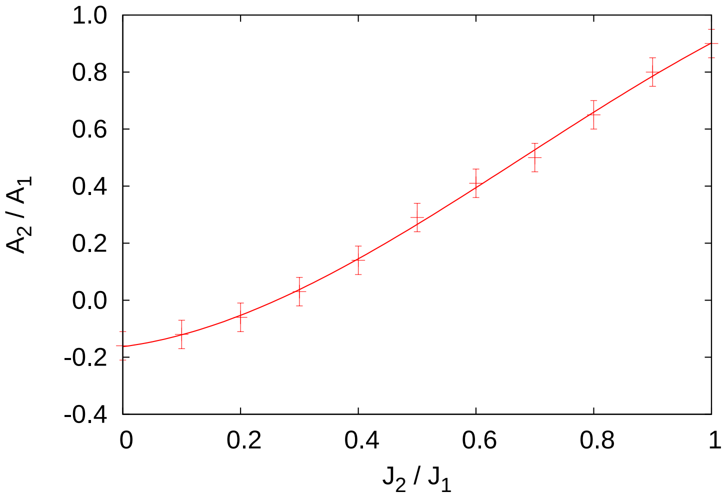

Figure 6.5: Optimal A_2/A_1 versus J_2/J_1 for the $\mathbf{q} = \mathbf{0}$ projected SB wave function, also optimized over μ for each J_2.

6.5 Results

Figure 6.4 shows the variational energies of the Dirac spin liquid, the $q = 0$ Schwinger boson spin liquid, and the $q = 0$ magnetically ordered state. For the Heisenberg model with nearest-neighbor coupling only ($J_2 = 0$), the Dirac spin liquid has significantly better energy than the Schwinger boson spin liquid. But for $J_2 > 0$, the $q = 0$ spin liquid trial energy improves quickly with J_2, and becomes the variational ground state for $J_2 > 0.08$ among the wave functions considered in this study. The $q = 0$ magnetically ordered state has higher energy for all J_2 values shown in the figure.

Figure 6.5 shows the optimal variational parameter A_2 against J_2 for the $q = 0$ Schwinger boson spin liquid. The results in the figure are also optimized over μ. For $J_2 = 0$, the second-neighbor A_{ij} lowers the energy significantly from -0.414 (for $A_2 = 0$) to $-0.420\ J_1$ per site. We obtain antiferromagnetic correlations between the second-neighbor sites. These results are very close to that obtained by Sindzingre *et al.* in a variational study of the J_1-only model[134], wherein they considered RVB ansatze with a few variational parameters for nearby-neighbors u_{jk} [Eq. 6.8] and a power-law decay $\sim |r_i - r_j|^{-p}$ with $p = 5$ for further neighbors. For our projected state, μ optimizes at $\mu_{\max}$ and leads to a critical state with power-law correlations with $p = 3$. Despite the difference in the exponents, both states are apparently trying to capture the critical correlations in the Dirac spin liquid at $J_2 = 0$. In the presence of second-neighbor J_2 coupling, A_2 increases with J_2 as shown in Fig. 6.5 and is important for improving the trial energy of the spin liquid. Beyond $J_2 \sim 0.1$, μ starts to decrease away from $\mu_{\max}$ and we obtain a power-law decay in u_{ij}.

Here, we discuss our own calculation of the Dirac spin liquid (SL) energy constructed from fermionic spinons hopping with flux π through hexagons and flux 0 through elementary triangles[41], which has good nearest-neighbor Heisenberg trial energy[42]. This state was extended in Ref. [44] to include second-neighbor hopping such that triangles formed by two nearest-neighbor bonds and one second-neighbor bond have flux π. (The second-neighbor bonds form three kagome networks and the above ansatz also has flux π through hexagons of these new networks.) The amplitude of the second-neighbor hopping provides a single variational parameter. For large sizes, we reproduced results in Ref. [44] for antiferromagnetic J_2. For the present $N = 36$ site cluster, the state that we used breaks lattice point group symmetries. (More precisely, gauge-invariant specification of the state also contains fluxes through loops that wind around the sample, and the state we used has such fluxes equal to 0 for two Kagome lattice directions and π for the remaining direction.) Comparing several larger systems[44], we find that the size dependence is negligible on the scale in Fig. 6.4. The Dirac SL does not have good second-neighbor spin correlations desired by the antiferromagnetic J_2, but we have not explored adding spinon pairing[44].

6.6 Summary and discussion

Our energetics study reveals the $q = 0$ spin liquid as a strong candidate for the J_1–J_2 Heisenberg model. This is perhaps not surprisingly since this state is already quite competitive in the J_1-only model (even if losing somewhat to other states) and has antiferromagnetic second-neighbor correlations which are favorable when $J_2 > 0$ is added[134]. The $q = 0$ state can furthermore accommodate the J_2 coupling by varying A_2, which was important in the energetics study (see Fig. 6.5). In the large-J_2 limit, the system breaks into three independent Kagome networks, each as difficult as the original nearest-neighbor Kagome problem. The large-A_2 spin liquid in the large-J_2 limit is just like A_1-only state on the original J_1-only model, so while not the best, is again reasonably good in energy. Thus, the A_1-A_2 ansatz provides a nice way to interpolate between the small-J_2 and large-J_2 regimes and is an appealing candidate from this point of view. It clearly wins against the Dirac spin liquid and also wins against the best attempt to construct q=0 magnetically ordered state, which is the most natural competing state here. It would be very interesting and useful to check our results against ED calculations in the J_1-J_2 model on the 36-site cluster to determine the accuracy of the $q = 0$ projected Schwinger boson spin liquid state.

In our study of projected Schwinger boson spin liquids, we made use of a straightforward dense permanent routine whose computational cost scales as $2^{N/2}$ (see Ref. [137]), where N is the number of sites. With reasonably more resources, one can push further to $N = 48$ and, if we also restrict u_{jk} to a few lattice spacings, it can also be scaled further due to sparseness of the matrix. Simulations in the valence bond basis may perhaps reach larger sizes[134]; attention to the sign problem is needed there although it is less severe than the sign problems in QMC. An important news from our work is that the Schwinger boson spin liquids can now be tested on the same footing as the slave fermion spin liquids, albeit for smaller but still reasonable cluster sizes, and can be added to the VMC toolbox of researchers. Here we highlight our use of the permanent construction in a variational study of Heisenberg model on the triangular lattice in magnetic field[1], where we obtained excellent wave functions for Mott insulators and supersolids of bosons with frustrated hopping. We suggest here the honeycomb spin liquid and Fa Wang's proposal as one context for applying the projected Schwinger boson spin liquid[138, 136], as well as other model proposals in Fa Wang's earlier paper on the triangular and kagome lattices for realizing new spin liquids[57].

Bibliography

[1] T. Tay and O. I. Motrunich, Phys. Rev. B **81**, 165116 (2010).

[2] T. Tay and O. I. Motrunich, Phys. Rev. Lett. **105**, 187202 (2010).

[3] T. Tay and O. I. Motrunich, Phys. Rev. B **83**, 205107 (2011).

[4] T. Tay and O. I. Motrunich, arXiv:1012.3783 (to appear in Phys. Rev. **B**).

[5] T. Tay and O. I. Motrunich, arXiv:1103.4429.

[6] H. Kawamura and S. Miyashita, J. Phys. Soc. Jpn **54**, 4530 (1985).

[7] A. V. Chubukov and D. I. Golosov, J. Phys. Condens. Matter **3**, 69 (1991).

[8] T. Ono et al., Phys. Rev. B **67**, 104431 (2003).

[9] N. A. Fortune et al., Phys. Rev. Lett. **102**, 257201 (2009).

[10] J. Alicea, A. V. Chubukov, and O. A. Starykh, Phys. Rev. Lett. **102**, 137201 (2009).

[11] T. Nikuni and H. Shiba, J. Phys. Soc. Jpn **64**, 3471 (1995).

[12] M. Y. Veillette and J. T. Chalker, Phys. Rev. B **74**, 052402 (2006).

[13] O. A. Starykh and L. Balents, Phys. Rev. Lett **98**, 077205 (2007).

[14] D. A. Huse and V. Elser, Phys. Rev. Lett. **60**, 2531 (1988).

[15] S. Yunoki and S. Sorella, Phys. Rev. B **74**, 014408 (2006).

[16] D. Heidarian, S. Sorella, and F. Becca, Phys. Rev. B **80**, 012404 (2009).

[17] M. Q. Weng, D. N. Sheng, Z. Y. Weng, and R. J. Bursill, Phys. Rev. B **74**, 012407 (2006).

[18] A. Paramekanti, L. Balents, and M. P. A. Fisher, Phys. Rev. B **66**, 054526 (2002).

[19] S. Sachdev, Nature **418**, 739 (2002).

[20] A. W. Sandvik, S. Daul, R. R. P. Singh, and D. J. Scalapino, Phys. Rev. Lett. **89**, 247201 (2002).

[21] R. G. Melko, A. W. Sandvik, and D. J. Scalapino, Phys. Rev. B **69**, 100408 (2004).

[22] V. Rousseau, G. G. Batrouni, and R. T. Scalettar, Phys. Rev. Lett. **93**, 110404 (2004).

[23] V. G. Rousseau, R. T. Scalettar, and G. G. Batrouni, Phys. Rev. B **72**, 054524 (2005).

[24] H. C. Jiang, Z. Y. Weng, and D. N. Sheng, Phys. Rev. Lett. **101**, 117203 (2008).

[25] P. Sindzingre and C. Lhuillier, EPL (Europhysics Letters) **88**, 27009 (2009).

[26] A. M. Lauchli, J. Sudan, and E. S. Srensen, arXiv:1103.1159 (2011).

[27] P. W. Leung and V. Elser, Phys. Rev. B **47**, 5459 (1993).

[28] C. Waldtmann et al., Eur. Phys. Journ. B - Condensed Matter and Complex Systems **2**, 501 (1998).

[29] Y. Simeng, D. A. Huse, and S. R. White, Science Express (2011).

[30] J. S. Helton et al., Phys. Rev. Lett. **98**, 107204 (2007).

[31] O. Ofer et al., cond-mat/0610540 (2006).

[32] P. Mendels et al., Phys. Rev. Lett. **98**, 077204 (2007).

[33] A. Olariu et al., Phys. Rev. Lett. **100**, 087202 (2008).

[34] R. R. P. Singh and D. A. Huse, Phys. Rev. Lett. **68**, 1766 (1992).

[35] R. R. P. Singh and D. A. Huse, Phys. Rev. B **76**, 180407 (2007).

[36] R. R. P. Singh and D. A. Huse, Phys. Rev. B **77**, 144415 (2008).

[37] R. Budnik and A. Auerbach, Phys. Rev. Lett. **93**, 187205 (2004).

[38] S. Capponi, A. Läuchli, and M. Mambrini, Phys. Rev. B **70**, 104424 (2004).

[39] G. Evenbly and G. Vidal, Phys. Rev. Lett. **104**, 187203 (2010).

[40] S. Sachdev, Phys. Rev. B **45**, 12377 (1992).

[41] M. B. Hastings, Phys. Rev. B **63**, 014413 (2000).

[42] Y. Ran, M. Hermele, P. A. Lee, and X.-G. Wen, Phys. Rev. Lett. **98**, 117205 (2007).

[43] Y.-C. Chen, Mod. Phys. Lett. B **8**, 1253 (1994).

[44] Y. Iqbal, F. Becca, and D. Poilblanc, arXiv:1011.3954v1 (2010).

[45] C. Xu and J. Moore, Nuclear Physics B **716**, 487 (2005).

[46] C. Xu and M. P. A. Fisher, Phys. Rev. B **75**, 104428 (2007).

[47] Z. Nussinov and E. Fradkin, Phys. Rev. B **71**, 195120 (2005).

[48] C. D. Batista and Z. Nussinov, Phys. Rev. B **72**, 045137 (2005).

[49] Z. Nussinov, C. D. Batista, and E. Fradkin, Int. Journ. Mod. Phys. B **20**, 5239 (2006).

[50] F. D. M. Haldane, Phys. Rev. Lett. **47**, 1840 (1981).

[51] M. P. A. Fisher and D. H. Lee, Phys. Rev. B **39**, 2756 (1989).

[52] V. J. Emery, E. Fradkin, S. A. Kivelson, and T. C. Lubensky, Phys. Rev. Lett. **85**, 2160 (2000).

[53] A. Vishwanath and D. Carpentier, Phys. Rev. Lett. **86**, 676 (2001).

[54] R. Mukhopadhyay, C. L. Kane, and T. C. Lubensky, Phys. Rev. B **63**, 081103 (2001).

[55] R. Mukhopadhyay, C. L. Kane, and T. C. Lubensky, Phys. Rev. B **64**, 045120 (2001).

[56] A. Auerbach, *Interacting Electrons and Quantum Magnetism*, Springer-Verlag, Berlin (1994).

[57] F. Wang and A. Vishwanath, Phys. Rev. B **74**, 174423 (2006).

[58] Sandro Sorella SISSA lecture notes, Numerical Methods for Strongly Correlated Electrons.

[59] J. H. Hetherington, Phys. Rev. A **30**, 2713 (1984).

[60] M. Calandra Buonaura and S. Sorella, Phys. Rev. B **57**, 11446 (1998).

[61] N. Trivedi and D. M. Ceperley, Phys. Rev. B **41**, 4552 (1990).

[62] D. Heidarian and A. Paramekanti, Phys. Rev. Lett. **104**, 015301 (2010).

[63] T. Ono et al., J. Phys. Condens. Matter **16**, S773 (2004).

[64] T. Ono et al., Prog. Theor. Phys. Supp **159**, 217 (2005).

[65] Y. Fujii et al., Physica B **346-347**, 45 (2004).

[66] Y. Fujii et al., J. Phys. Condens. Matter **19**, 145237 (2007).

[67] H. Tsujii et al., Phys. Rev. B **76**, 060406 (2007).

[68] B. Bernu, P. Lecheminant, C. Lhuillier, and L. Pierre, Phys. Rev. B **50**, 10048 (1994).

[69] A. Honecker, J. Schulenburg, and J. Richter, J. Phys. Condens. Matter **16**, S749 (2004).

[70] S. Yoshikawa, K. Okunishi, M. Senda, and S. Miyahara, J. Phys. Soc. Jpn **73**, 1798 (2004).

[71] S. Miyahara, K. Ogino, and N. Furukawa, Physica. B **378**, 587 (2006).

[72] A. Honecker, J. Phys. Condens. Matter **11**, 4697 (1999).

[73] T. Pardini and R. R. P. Singh, Phys. Rev. B **77**, 214433 (2008).

[74] H. C. Jiang, M. Q. Weng, Z. Y. Weng, D. N. Sheng, and L. Balents, Phys. Rev. B **79**, 020409 (2009).

[75] F. Wang, F. Pollmann, and A. Vishwanath, Phys. Rev. Lett. **102**, 017203 (2009).

[76] D. Ceperley and G. V. Chester, Phys. Rev. B **17**, 1070 (1978).

[77] L. Reatto and G. V. Chester, Phys. Rev. **155**, 88 (1967).

[78] G. Misguich, T. Jolicoeur, and S. M. Girvin, Phys. Rev. Lett. **87**, 097203 (2001).

[79] O. I. Motrunich and M. P. A. Fisher, Phys. Rev. B **75**, 235116 (2007).

[80] D. M. Ceperley, G. V. Chester, and M. H. Kalos, Phys. Rev. B **16**, 3081 (1977).

[81] V. Kalmeyer and R. B. Laughlin, Phys. Rev. B **39**, 11879 (1989).

[82] X. G. Wen, F. Wilczek, and A. Zee, Phys. Rev. B **39**, 11413 (1989).

[83] Y. Zhou and X.-G. Wen, (2002).

[84] Y. Ran, W.-H. Ko, P. A. Lee, and X.-G. Wen, Phys. Rev. Lett. **102**, 047205 (2009).

[85] K. J. Runge, Phys. Rev. B **45**, 7229 (1992).

[86] N. Read and S. Sachdev, Phys. Rev. Lett. **62**, 1694 (1989).

[87] C. Lannert, M. P. A. Fisher, and T. Senthil, Phys. Rev. B **63**, 134510 (2001).

[88] T. Senthil, A. Vishwanath, L. Balents, S. Sachdev, and M. P. A. Fisher, Science **303**, 1490 (2004).

[89] T. Senthil, L. Balents, S. Sachdev, A. Vishwanath, and M. P. A. Fisher, Phys. Rev. B **70**, 144407 (2004).

[90] O. Narayan and B. S. Shastry, J. Phys. A: Math. Gen. **32**, 1131 (1999).

[91] M. Capello, F. Becca, M. Fabrizio, and S. Sorella, Phys. Rev. Lett. **99**, 056402 (2007).

[92] M. Capello, F. Becca, M. Fabrizio, and S. Sorella, Phys. Rev. B **77**, 144517 (2008).

[93] P. A. Lee, N. Nagaosa, and X.-G. Wen, Rev. Mod. Phys. **78**, 17 (2006).

[94] R. K. Kaul, Y. B. Kim, S. Sachdev, and T. Senthil, Nature Physics **4**, 28 (2008).

[95] T. Senthil, Phys. Rev. B **78**, 035103 (2008).

[96] S.-S. Lee, Phys. Rev. B **80**, 165102 (2009).

[97] D. N. Sheng, O. I. Motrunich, S. Trebst, E. Gull, and M. P. A. Fisher, Phys. Rev. B **78**, 054520 (2008).

[98] M. P. A. Fisher, O. I. Motrunich, and D. N. Sheng, arXiv:0812.2955 (2008).

[99] A. E. Feiguin and M. P. A. Fisher, arXiv:1007.5251 (2010).

[100] D. F. Mross, J. McGreevy, H. Liu, and T. Senthil, Phys. Rev. B **82**, 045121 (2010).

[101] T. Faulkner, N. Iqbal, H. Liu, J. McGreevy, and D. Vegh, Science **329**, 1043 (2010).

[102] S. Sachdev, (arXiv:1006.3794).

[103] L. Balents, Nature **464**, 199 (2010).

[104] X.-G. Wen, Phys. Rev. B **65**, 165113 (2002).

[105] T. Holstein, R. E. Norton, and P. Pincus, Phys. Rev. B **8**, 2649 (1973).

[106] M. Reizer, Phys. Rev. B **40**, 11571 (1989).

[107] P. A. Lee and N. Nagaosa, Phys. Rev. B **46**, 5621 (1992).

[108] J. Polchinski, Nucl. Phys. B **422**, 617 (1994).

[109] B. L. Altshuler, L. B. Ioffe, and A. J. Millis, Phys. Rev. B **50**, 14048 (1994).

[110] Y. B. Kim, A. Furusaki, X. G. Wen, and P. A. Lee, Phys. Rev. B **50**, 17917 (1994).

[111] M. A. Metlitski and S. Sachdev, Phys. Rev. B **82**, 075127 (2010).

[112] W. Rantner and X.-G. Wen, Phys. Rev. B **66**, 144501 (2002).

[113] M. Hermele et al., Phys. Rev. B **70**, 214437 (2004).

[114] O. I. Motrunich, Phys. Rev. B **72**, 045105 (2005).

[115] M. Hermele, Y. Ran, P. A. Lee, and X.-G. Wen, Phys. Rev. B **77**, 224413 (2008).

[116] C. Gros, Annals of Physics **189**, 53 (1989).

[117] M. P. A. Fisher, (arXiv:Cond-mat/9806164v2).

[118] T. Giamarchi, Quantum Physics in One Dimension, Clarendon Press, Oxford, 2004.

[119] A. Bijl, Physica **7**, 869 (1940).

[120] R. Jastrow, Phys. Rev. **98**, 1479 (1955).

[121] C. S. Hellberg and E. J. Mele, Phys. Rev. Lett. **67**, 2080 (1991).

[122] M. Capello, F. Becca, S. Yunoki, M. Fabrizio, and S. Sorella, Phys. Rev. B **72**, 085121 (2005).

[123] Although the row and column boson numbers are not strictly enforced in the harmonic approximations for both wave functions, the presence of similar "cross" feature in the density structure factors in Eqs. (5.38) and (5.47) suggests that this still holds approximately. To show this more explicitly, we calculate the single boson propagator for both wave functions and obtain the form $\langle b_{\mathbf{0}}^{\dagger} b_{\mathbf{r}} \rangle \sim \delta_{\mathbf{r},\mathbf{0}}$. Interestingly, this shows that single boson hopping is suppressed even in the harmonic approximations.

[124] Our estimates are $W_{\text{EBL}}^{\text{crit}} \approx 4.4$ and $W_{\text{1d}}^{\text{crit}} \approx 3.4$ for developing (π, π) CDW order at half-filling in the EBL and Gutzwiller wave functions respectively.

[125] B. K. Clark, D. A. Abanin, and S. L. Sondhi, (arXiv:1010.3011).

[126] D. N. Sheng, O. I. Motrunich, and M. P. A. Fisher, Phys. Rev. B **79**, 205112 (2009).

[127] M. S. Block et al., (arXiv:1008.4105).

[128] M. S. Block, D. N. Sheng, O. I. Motrunich, and M. P. A. Fisher, (arXiv:1009.1179).

[129] P. Calabrese, J. Cardy, and B. Doyon, Journal of Physics A: Mathematical and Theoretical **42**, 500301 (2009).

[130] M. B. Hastings, I. González, A. B. Kallin, and R. G. Melko, Phys. Rev. Lett. **104**, 157201 (2010).

[131] L. Messio, O. Cépas, and C. Lhuillier, Phys. Rev. B **81**, 064428 (2010).

[132] Discussion from KITP program, Disentangling Quantum Many-body Systems: Computational and Conceptual Approaches.

[133] S. R. White [private communication].

[134] P. Sindzingre, P. Lecheminant, and C. Lhuillier, Phys. Rev. B **50**, 3108 (1994).

[135] The minimum of the spinon dispersion is at $\mathbf{k} = \mathbf{0}$ for $A_2/A_1 > -0.25$ and jumps to new locations for $A_2/A_1 < -0.25$. The relevant spinon bands happen to be very narrow near the transition and this results in large κ_c.

[136] F. Wang, Phys. Rev. B **82**, 024419 (2010).

[137] I. M. Wanless, *Permanents*, Chapter 31 in *Handbook of Linear Algebra* (ed. L. Hogben), Chapman & Hall/CRC (2007).

[138] Z. Y. Meng, T. C. Lang, S. Wessel, F. F. Assaad, and A. Muramatsu, Nature **464**, 847 (2010).